Master Thesis

Design of Sandwich Structures with Grid-Scored Core for Wind Turbine Blades

M. Milis

Delft University of Technology

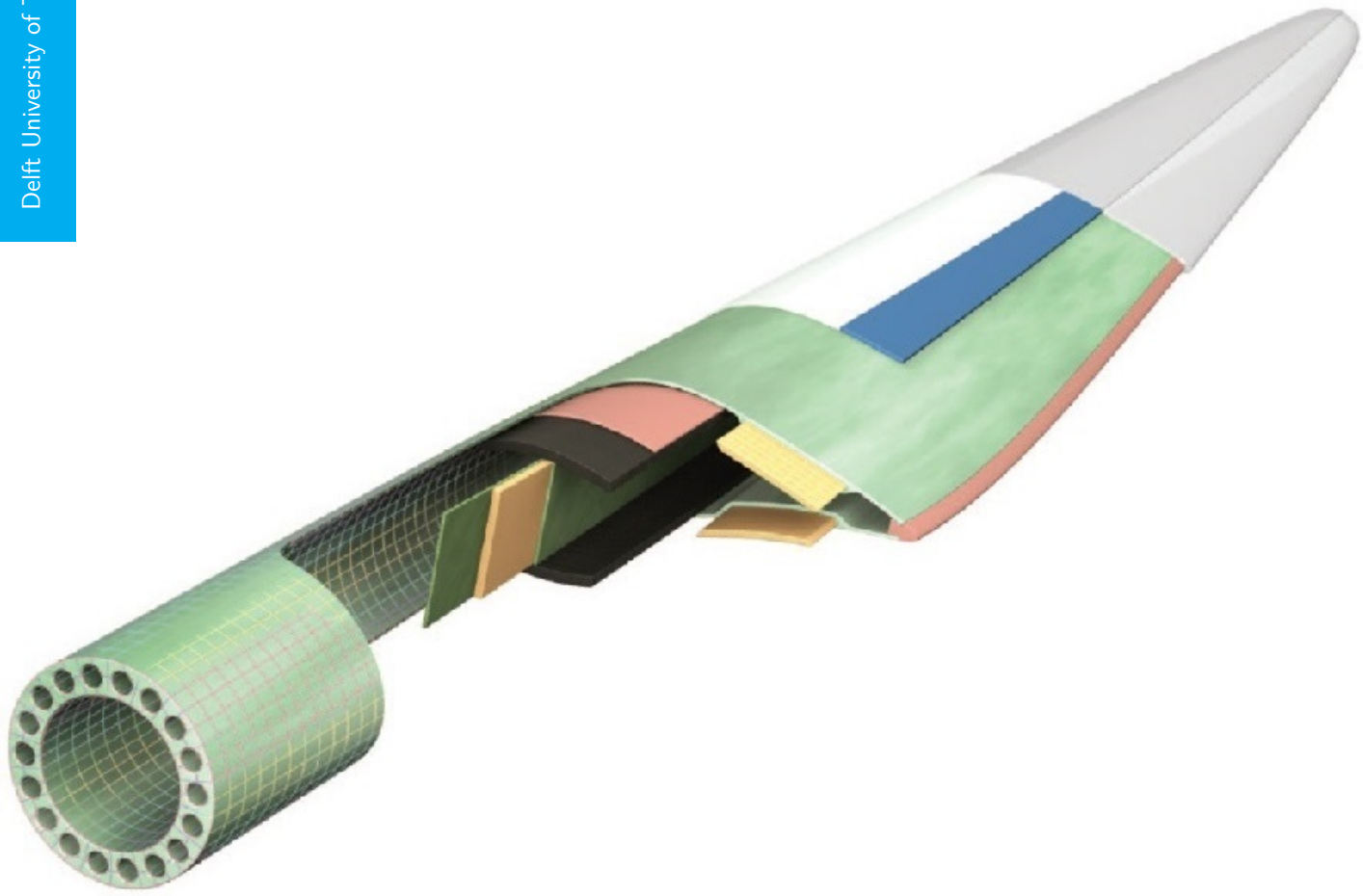

TU Delft Delft University of Technology

Challenge the future

Master Thesis

Design of Sandwich Structures with Grid-Scored Core for Wind Turbine Blades

by

M. Milis

in partial fulfillment of the requirements for the degree of

Master of Science
in Aerospace Engineering

at the Delft University of Technology,
to be defended publicly on Monday December 4, 2017 at 14:00.

Student number TUDelft:	1530747
Student number DTU:	s122640
Supervisors:	Dr. Ir. D. Zarouchas
	Ir. K. Branner
	Ir. J.A. Bhangale
Thesis committee:	Dr. Ir. C.J. Ferreira
	Dr. Ir. D. Zarouchas
	Ir. K. Branner
	Ir. J.A. Bhangale

The cover page image is taken from Gurit [1]

An electronic version of this thesis is available at http://repository.tudelft.nl/.

TU Delft Delft University of Technology

ABSTRACT

A wind turbine blade experiences a spectrum of different loads during its operational lifetime. Most modern wind turbine design layouts consist of a spar, shear webs and a stiffened skin. This latter component is generally composed of a composite sandwich structure. Sandwich structures are implemented because of their high stiffness and strength to mass ratio, and high capability of handling shear loads. Sandwich structures are of interest for this study.

In wind turbine blade skins, grid-scored core materials are used because of the large curvatures in the blade. Inducing this grid to the core material affects the failure behaviour of the sandwich structure. Since sandwich structures are composed of different components (constituents), they can display a number of different failure behaviours depending on the size and the type of loading. This project focuses on shear loading and its failure behaviour. Increased insight into this failure behaviour can not only improve the performance of the wind turbine blade, but also lead to significant savings in weight, cost and performance of the overall wind turbine. A new design concept is proposed by Suzlon Blades Technology, Hengelo, the Netherlands, that will alter the core material of the standard sandwich structure. This adaptation to the standard grid-scored core is further called "resin links" and aims to improve the strength and failure behaviour of the standard grid-scored sandwich structure.Therefore, the aim of this project is to assess whether the implementation of resin links can improve the performance and failure resistance of grid-scored sandwich structures in wind turbine applications.

Test data[1] for flatwise tensile and three point bending tests are available for the standard grid-scored core sandwich structures. New tests on sandwich structures with incorporated resin links were performed during this research in two different resin link sizings. Flatwise tensile and three/four point bending tests were performed and compared to the benchmark tests. A stereoscopic digital image correlation system was used to analyse the strain fields of the tested specimens and gain a better insight in the failure behaviour of the proposed design concept.

When comparing the benchmark with the resin link three point bending tests a significant observation is made with respect to the direction of loading. For the benchmark tests, the sandwich structure exhibits a very different behaviour depending on whether the structure is loaded scrim side up or down. On the other hand, for the resin link test case, no visible difference in performance between scrim up or down loading can be found, meaning that this structure performs more consistently.
For the performed flatwise tensile, three and four point bending tests, in general, the effect of the proposed resin links design change is small, and no significant trends can be observed when comparing benchmark to resin link specimens. When only considering the resin link tests, it can be concluded from all tests that the more resin is added, thus the larger the resin links are, the more the maximum strain increases, while the maximum stress and stiffness decrease.

[1] Tests performed by Suzlon Blades Technology (SBT).

ACKNOWLEDGEMENTS

This thesis is the conclusion of my time as a student at the Faculty of Aerospace Engineering. It would not have been possible without the involvement of a great number of people.

First of all I would like to offer my special thanks to my supervisors Dr. Ir. Dimitrios Zarouchas, Ir. Jaykarna Ashok Bhangale, and Ir. Kim Branner for guiding me throughout my research and providing me with insightful feedback, but most importantly for their persistent support and care when I needed it the most. Thank you all for investing your time, energy and problem-solving experience.

Thank you Dr. Ir. C.J. Ferreira for reading and judging my thesis and being chairman on my graduation committee.

Thanks also to Dr. Ing. Harald Bersee, Ir. Jaykarna Ashok Bhangale and Suzlon Blades Technology for offering me a graduation topic, expert help and facilities to start and complete my thesis work.

To Linda Gaffel and Dr. Ir. Gerard van Bussel, thank you for your genuine concern for students. Your conversations always left me with a positively motivated and inspired feeling.

Gratitude to the many people I can proudly call my friends, for believing in me, for the motivational talks, for all the laughs, for the advice, for having beers with me and for not making (too much) fun of me for being the last of my MSc graduation cohort to graduate. This list of friends I want to thank in particular in relation to my thesis work consists of amongst others; Ashim, Bas, Bram, Brecht, Clara, Daniel, Dieter, Fie, Florian, Lukas, Marcos, Michiel, Michiel, Pranav, Ruben and Tom.

Fellow students, current and former residents of graduation room 6.08, thank you for the daily support, for the coffee breaks, lunch games, lunch discussions, and all kinds of international food and treats.

I want to thank my parents for their unwavering faith in me and their help in all manner of things. Our relationship has changed since I'm not living at home anymore, however it has grown all the more.

Last but not least, Kathleen, you are truly an amazing person. Thank you for your love and support. I am pretty sure I could not have managed to finish this project without you. You mean the world to me.

To all people in this list and those that I forgot to add in this list; Thank you all for enriching my life on a professional and personal level.

M. Milis
Delft, November 2017

CONTENTS

Abstract iii

Acknowledgements v

List of Figures ix

List of Tables xiii

Nomenclature xvii

List of Abbreviations xix

1 Introduction 1
- 1.1 Problem Statement . . . 1
- 1.2 Research Outline . . . 1
- 1.3 Hypothesis . . . 2
- 1.4 Report Outline . . . 2

2 Resin Links 3
- 2.1 The Concept . . . 3
- 2.2 Concept Trade-Off and Design . . . 6
- 2.3 Testing of the Resin Link Coupons . . . 8
  - 2.3.1 Digital Image Correlation (DIC) . . . 9
  - 2.3.2 Flatwise Tensile Test . . . 9
  - 2.3.3 Three and Four Point Bending Test . . . 10
- 2.4 Production of the Resin Link Sandwich Plate and Coupons . . . 10

3 Literature Study 19
- 3.1 Wind Turbine Blade Design . . . 19
  - 3.1.1 Blade Layout . . . 19
  - 3.1.2 Materials . . . 21
  - 3.1.3 Contour Finishing Options . . . 24
- 3.2 Structural Failure of Composite Sandwich Structures in Wind Turbine Applications . . . 26
  - 3.2.1 Failure Criteria . . . 26
  - 3.2.2 Failure of Composite Laminates . . . 28
  - 3.2.3 Failure of Composite Sandwich Structures . . . 28
  - 3.2.4 Failure of Contour Cut Sandwich Structures . . . 35
  - 3.2.5 Improving Failure Capacity Of Composite Sandwich Structures . . . 36

4 Material Characterisation 39
- 4.1 PVC Core Characterisation . . . 39
- 4.2 Resin Characterisation . . . 42
- 4.3 Grid-Scored Sandwich Structures - Characterisation . . . 42
  - 4.3.1 Flatwise Tension . . . 43
  - 4.3.2 Three Point Bending . . . 44

5 Experimental Results 49
- 5.1 Flatwise Tension Results . . . 49
- 5.2 Three Point Bending Results . . . 55
- 5.3 Four Point Bending Results . . . 62

6 Conclusions & Recommendations 67
- 6.1 Conclusions . . . 67
- 6.2 Recommendations . . . 68

Bibliography **71**

A Characterisation Appendix **75**
A.1 Facings Characterisation . . . 75
A.1.1 Edgewise Tensile (ET) Characterisation . . . 75
A.1.2 Edgewise Compression (EC) Characterisation . . . 78
A.1.3 Flatwise Compression Characterisation . . . 80
A.2 Airex C70.55 PVC Core Characterisation . . . 82
A.2.1 Compressive Characterisation . . . 83
A.2.2 Tensile Characterisation . . . 85
A.3 Sandwich Characterisation . . . 86
A.3.1 Edgewise Compression . . . 86
A.3.2 Edgewise Tensile . . . 90
A.3.3 Flatwise Compression . . . 92
A.3.4 Rail Shear . . . 94

B Resin Link Results **97**
B.1 Flatwise Tension 3mm Resin Link Results . . . 97
B.2 Flatwise Tension 5mm resin link Results . . . 97
B.3 Three Point Bending 3mm Resin Link Results . . . 98
B.4 Three Point Bending 5mm Resin Link Results . . . 99
B.5 Four Point Bending 3mm Resin Link Results . . . 100
B.6 Four Point Bending 5mm Resin Link Results . . . 101

C Digital Appendix **103**

List of Figures

2.1 Normal "benchmark" grid-scored core sandwich structure. . . . 4
2.2 Concept "walls" sandwich structure - side and top view - lesin links in blue. . . . 5
2.3 Concept "holes" sandwich structure - side and top view - resin links in blue. . . . 6
2.4 Concept "slanted" sandwich structure - side and top view - resin links in blue. . . . 6
2.5 Top view of resin link structure showing overlap in resin link and resin bridge. . . . 7
2.6 Influence of link diameter on effectiveness ratio and weight increase. . . . 8
2.7 DIC schematic setup and DIC calibration plates. . . . 9
2.8 Flatwise tensile test setup and support fixture layout. . . . 10
2.9 TPB Test setup. . . . 10
2.10 Pictures of the hole drilling step of the production process. . . . 11
2.11 Release agent and lay-up sequence. . . . 11
2.12 Features of the to be infused sandwich plate. . . . 12
2.13 Infusion Process. . . . 13
2.14 Temperature during pre- and post-cure. . . . 14
2.15 Inspection of the sandwich plate after pre-cure; close-up. . . . 14
2.16 Inspection of the sandwich plate after pre-cure: measuring warp. . . . 15
2.17 Table saw and light inspection. . . . 15
2.18 All the cut coupons ready for post-cure. . . . 15
2.19 Coupon inspection. . . . 16
2.20 Coupons before and during the paint process. . . . 16
2.21 Flatwise tensile test loading blocks and coupons. . . . 17
2.22 Heat flow measurements of pre- and post-cured samples. . . . 18

3.1 Example of a wind turbine layout. . . . 19
3.2 Velocity Triangle; Schematising the apparent wind experienced by a section of a wind turbine blade. . . . 20
3.3 Typical wind turbine blade cross-section[2]. . . . 21
3.4 General blade design concepts for modern wind turbines. . . . 21
3.5 Composite - individual properties and composite sandwich layout. . . . 22
3.6 Ashby plots of material category properties. . . . 23
3.7 Different core types used for composite sandwich construction. . . . 24
3.8 Types of contour finishing options for closed-cell sandwich core materials . . . 25
3.9 Maximum stress failure criterion for a brittle material[3]. . . . 27
3.10 Visualisation of failure criteria . . . 27
3.11 First Ply -(FPF) and Last Ply Failure(LPF) - Schematisation of progressive failure analysis[3]. . . . 28
3.12 Impact induced delamination and test setup[4]. . . . 30
3.13 Core facing failure in flatwise and edgewise bending[5]. . . . 31
3.14 Debonding of facings in edgewise compression and three point bending loading. . . . 31
3.15 Core failure in four point bending and flatwise tension. . . . 32
3.16 Induced delamination and possible subsequent buckling failure modes (Figures[6]). . . . 33
3.17 Wrinkling types for composite sandwich structures[7]. . . . 34
3.18 Grid-scored core structures . . . 36
3.19 Core materials with fibre web reinfocements through the thickness. . . . 37
3.20 Core materials with reinforcements through the thickness. . . . 37
3.21 Core materials with strong fibre pin reinforcements through the thickness . . . 37
3.22 Concepts to stop or deflect cracks in sandwich structures . . . 38

4.1 Rail shear test type schematic and test setup picture. . . . 41
4.2 Rail shear stress-strain curves from research by Berthelot et al. [8]. . . . 41

4.3 Resin Y - Stress-strain data. . . . 42
4.4 Flatwise compression (FT) specimens. . . . 43
4.5 Flatwise compression specimens during loading. . . . 44
4.6 FT specimens after testing showing different damage modes. . . . 44
4.7 Stress-strain curves for FT sandwich specimens. . . . 45
4.8 TPB schematic representation and test setup. . . . 45
4.9 TPB sandwich coupons after testing. . . . 46
4.10 Characterisation analysis of TPB test coupons - Flexural stress vs flexural strain 46
4.11 Characterisation analysis of TPB test coupons - Shear stress vs displacement. . . . 47

5.1 Flatwise tension specimens of sandwich structures with 3mm resin links after test. . . . 49
5.2 Flatwise tension specimens of sandwich structures with 5mm resin links after test. . . . 50
5.3 Close-up of flatwise tension specimens after test. . . . 50
5.4 Schematics of the observed fracture shape of the FT tensile specimens. . . . 50
5.5 Stress-strain graphs of benchmark, $3mm$ and $5mm$ resin link specimens for flatwise tension . . . 51
5.6 Flatwise tensile trends of benchmark and $3mm$ & $5mm$ resin link cases. . . . 51
5.7 DIC images for the flatwise tensile test of the 3mm resin link specimens. . . . 52
5.8 FT^{10}_{5mm} before (left) and after (right) crack initiation. . . . 53
5.9 FT^{10}_{5mm} before (left) and after (right) crack initiation. . . . 54
5.10 Three point bending specimens without resin links with either Scrim Up (SU) or Scrim Down (SD) . . . 56
5.11 Three point bending specimens numbers 1-10 with either Scrim Up (SU) or Scrim Down (SD). . . 56
5.12 Three point bending specimens numbers 1-10 with either Scrim Up (SU) or Scrim Down (SD). . . 56
5.13 Three point bending shear diagram. . . . 57
5.14 Stress-strain graphs for three point bending specimens for benchmark and $3mm$ and $5mm$ resin links. . . . 57
5.15 Shear stress-displacement graphs for three point bending specimens for benchmark and $3mm$ and $5mm$ resin links. . . . 58
5.16 TPB trends of benchmark and $3mm$ & $5mm$ resin link cases. . . . 59
5.17 DIC Images for the TPB Test of the 3mm and 5mm resin link specimens. All images captured right before failure. . . . 60
5.18 4 Point bending specimens with resin links with either scrim up (SU) or scrim down (SD) 62
5.19 4 point bending shear diagrams. . . . 63
5.20 4 Point bending specimens for 3mm and 5mm resin links. Top 2 graphs show the flexural stress-strain and the bottom 2 graphs show the shear stress-displacement. . . . 64
5.21 FPB trends of benchmark and $3mm$ & $5mm$ resin link cases. . . . 64
5.22 DIC Images for the FPB Test of the 3mm and 5mm resin link specimens. Images taken right before failure. . . . 65

A.1 0° oriented strain gauge measurements for the edgewise tensile test of the biax coupons. . . . 76
A.2 Front side measurements and computed important parameters. . . . 76
A.3 Edgewise tensile test shear stress vs shear strain curves - front and back facing. . . . 77
A.4 Edgewise tensile test shear stress vs shear strain curves - front and back facing - including average values. . . . 77
A.5 Triax lay-up normal stress-strain and shear stress-strain curves indicating average values for damage, maximum and ultimate stresses and strains. . . . 79
A.6 0° oriented strain gauge measurements for the edgewise tensile test of the biax coupons. . . . 80
A.7 0° oriented strain gauge measurements for the edgewise tensile test of the biax and triax coupons. 80
A.8 Stress-strain curves for biax and triax specimens loaded in flatwise compression. . . . 81
A.9 Stress-strain curves for biax and triax specimens loaded in flatwise compression. . . . 82
A.10 Flatwise compression test type schematic and test setup picture . . . 83
A.11 Flatwise compression stress-strain curves from research by Berthelot et al. [8]. . . . 83
A.12 In-plane compression stress-strain curves from research by Berthelot et al. [8]. . . . 84
A.13 Analysed data from data in Figure A.12a. . . . 85
A.14 Edgewise tension stress-strain curves from research by Berthelot et al. [8]. . . . 85
A.15 Acceptable and unacceptable failure modes for ASTM C364. . . . 87

A.16 ASTM C364 coupon dimensions. 87
A.17 Edgewise compression specimens showing tabs at each end and 1 strain gauge per side. 88
A.18 Edgewise compression specimens during and after loading. 88
A.19 Edgewise compression specimens after loading showing facing damage. 89
A.20 Stress-strain curves for the EC test specimens for both front and back side strain gauges. 89
A.21 Edgewise tensile (ET) specimens showing tabs at each end and 2 strain gauges in perpendicular position on 1 facing. 91
A.22 Edgewise tensile specimens during and after testing - multiple views. 91
A.23 Stress-strain curves for ET tests for both 0° and 90° oriented strain gauges. 92
A.25 Flatwise compression specimens during loading. 93
A.26 FC specimens after testing showing different damage modes. 94
A.27 Analysis of sandwich and PVC core FC tests. 95
A.28 Sxz sandwich shear stress-shear strain curve. 96

List of Tables

2.1 Trade-off of different resin link concepts. . . . 7
2.2 Types, sizes, and amount of plies needed for the sandwich plate lay-up. . . . 12

3.1 Failure modes in sandwich beams[4]. . . . 29

4.1 Airex C70.55 properties as given by the manufacturer[9]. . . . 40
4.2 Mechanical characteristics of the C70.55 foam subjected to through-thickness shear. . . . 41
4.3 Averaged data from all edgewise tensile characterisation tests for resin material. Units for stresses and moduli are [MPa] and units for strains are [%]. . . . 42
4.4 FT: Design and actual coupon dimensions. Average values based on 5 test coupons. . . . 43
4.5 Resulting averaged data for FT tests. Units for stresses and moduli are [MPa] and units for strains are [%]. . . . 44
4.6 TPB: Design and actual coupon dimensions. Average values based on 6 test coupons. . . . 45
4.7 Averaged data from the three point bending SU flexural stress-strain graph. Units for stresses and moduli are [MPa] and units for strains are [%]. . . . 47
4.8 Averaged data from the three point bending SD flexural stress-strain graph. Units for stresses and moduli are [MPa] and units for strains are [%]. . . . 47
4.9 Averaged shear stress vs displacement data from all TPB Characterisation tests benchmark SU Sandwich Structure. . . . 47
4.10 Averaged shear stress vs displacement data from all TPB Characterisation tests benchmark SU Sandwich Structure. . . . 47

5.1 Resulting averaged data for FT benchmark tests. Units for stresses and moduli are [MPa] and units for strains are [%]. . . . 50
5.2 Averaged data from all flatwise tensile characterisation tests for resin link 3mm Sandwich Structure. Data for each specific specimen can be found in Table B.1 in Appendix B.1. . . . 51
5.3 Averaged data from all flatwise tensile characterisation tests for resin link 5mm Sandwich Structure. Data for each specific specimen can be found in Table B.2 in Appendix B.2. . . . 51
5.4 Table showing maximum strain values at the crack position at crack initation for the flatwise tensile test of 3mm resin link specimens. . . . 53
5.5 Averaged data from the benchmark three point bending SU flexural stress-strain graph. Units for stresses and moduli are [MPa] and units for strains are [%]. . . . 58
5.6 Averaged flexural stress-strain data from all TPB characterisation tests for resin link 3mm Sandwich Structure. Data for each specific specimen can be found in Table B.3 in Appendix B.3. . . . 59
5.7 Averaged flexural stress-strain data from all TPB characterisation tests for resin link 5mm Sandwich Structure. Data for each specific specimen can be found in Table B.5 in Appendix B.4. . . . 59
5.8 Averaged shear stress vs displacement data from all TPB characterisation tests benchmark Sandwich Structure. . . . 59
5.9 Averaged shear stress vs displacement data from all TPB characterisation tests benchmark SU Sandwich Structure. . . . 59
5.10 Averaged shear stress vs displacement data from all TPB characterisation tests for resin link 3mm Sandwich Structure. Data for each specific specimen can be found in Table B.4 in Appendix B.3. . . . 60
5.11 Averaged shear stress vs displacement data from all TPB characterisation tests for resin link 5mm Sandwich Structure. Data for each specific specimen can be found in Table B.6 in Appendix B.4. . . . 60
5.12 Table showing maximum strain values right before failure for the three point bending test of $3mm$ and $5mm$ resin link specimens. . . . 61

5.13 Averaged flexural stress-strain data from all FPB characterisation tests for resin link 3mm Sandwich Structure. Data for each specific specimen can be found in Table B.7 in Appendix B.5. . . . 63
5.14 Averaged flexural stress-strain data from all FPB characterisation tests for resin link 3mm Sandwich Structure. Data for each specific specimen can be found in Table B.9 in Appendix B.6. . . . 63
5.15 Averaged shear stress-displacement data from all FPB characterisation tests for resin link 3mm Sandwich Structure. Data for each specific specimen can be found in Table B.8 in Appendix B.5. 63
5.16 Averaged shear stress-displacement data from all FPB characterisation tests for resin link 5mm Sandwich Structure. Data for each specific specimen can be found in Table B.10 in Appendix B.6. 65
5.17 Table showing maximum strain values right before failure for the four point bending test of $3mm$ and $5mm$ resin link specimens. 66

A.1 Specimen sizes for the SBT edgewise tensile test coupons. 75
A.2 Averaged data from all edgewise tensile characterisation tests for both biax and triax materials. Units for stresses and moduli are [MPa] and units for strains are [%]. 78
A.3 Specimen sizes for the SBT edgewise compression test coupons. 79
A.4 Averaged data from all edgewise compression characterisation tests for both biax and triax materials. Units for stresses and moduli are [MPa] and units for strains are [%]. 81
A.5 Specimen sizes for the SBT flatwise compression test coupons. 81
A.6 Averaged data from all flatwise compression characterisation tests for both biax and triax materials. Units for stresses and moduli are [MPa] and units for strains are [%]. 82
A.7 Mechanical characteristics of the C70.55 foam subjected to transverse (through-thickness) and in-plane compression. 84
A.8 Mechanical characteristics of the C70.55 foam subjected to transverse (through-thickness) and in-plane tension. 86
A.9 EC: Design and actual coupon dimensions. Average values based on 6 test coupons. 86
A.10 Resulting averaged data for EC tests for both front and back strain gauges. Units for stresses and moduli are [MPa] and units for strains are [%]. 89
A.11 ET: Design and actual coupon dimensions. Average values based on 6 test coupons. 90
A.12 Resulting averaged data for ET tests for both 0° and 90° oriented strain gauges. Units for stresses and moduli are [MPa] and units for strains are [%]. 92
A.13 Flatwise compression (FC) specimens before testing. 93
A.14 FC: Design and actual coupon dimensions. Average values based on 8 test coupons. 93
A.15 Resulting averaged data for FC tests. Units for stresses and moduli are [MPa] and units for strains are [%]. 94
A.16 Sxz: Design and actual coupon dimensions. Average values based on 9 test coupons. 95
A.17 Averaged data from all rail shear characterisation tests. Units for stresses and moduli are [MPa] and units for strains are [%]. 95

B.1 Data for all flatwise tensile characterisation tests for resin link 3mm sandwich structure. Units for stresses and moduli are [MPa] and units for strains are [%]. 97
B.2 Data for all flatwise tensile characterisation tests for resin link 5mm sandwich structure. Units for stresses and moduli are [MPa] and units for strains are [%]. 98
B.3 Flexural stress-strain data for all TPB characterisation tests for resin link 3mm sandwich structure. Units for stresses and moduli are [MPa] and units for strains are [%]. 98
B.4 Shear stress-displacement data for all TPB characterisation tests for resin link 3mm sandwich structure. Units for stresses and moduli are [MPa] and units for strains are [%]. 99
B.5 Flexural stress-strain data for all TPB characterisation tests for resin link 5mm sandwich structure. Units for stresses and moduli are [MPa] and units for strains are [%]. 99
B.6 Shear stress-displacement data for all TPB characterisation tests for resin link 5mm sandwich structure. Units for stresses and moduli are [MPa] and units for strains are [%]. 100
B.7 Flexural stress-strain data for all TPB characterisation tests for resin link 5mm sandwich structure. Units for stresses and moduli are [MPa] and units for strains are [%]. 100
B.8 Shear stress vs displacement data for all TPB characterisation tests for resin link 3mm sandwich structure. Units for shear stresses are [MPa] and units for displacements are [mm]. 101
B.9 Flexural stress-strain data for all TPB characterisation tests for resin link 5mm sandwich structure. Units for stresses and moduli are [MPa] and units for strains are [%]. 101

B.10 Shear stress vs displacement data for all TPB characterisation tests for resin link 5mm sandwich structure. Units for shear stresses are [MPa] and units for displacements are [mm]. 102

C.1 Overview of the contents of the digital appendix. 103

NOMENCLATURE

Symbol	Unit	Definition
δ_{dmg}	[mm]	Deflection at damage shear stress τ_{dmg}
δ_{max}	[mm]	Deflection at maximum shear stress τ_{max}
δ_{ult}	[mm]	Deflection at ultimate shear stress τ_{ult}
δ_x	[mm]	Beam deflection
ϵ_f=$\epsilon_{flexural}$	[%]	Flexural strain
ϵ_{f_dmg}	[%]	Flexural strain at damage flexural stress σ_{f_dmg}
ϵ_{f_max}	[%]	Flexural strain at maximum flexural stress σ_{f_max}
ϵ_{f_ult}	[%]	Flexural strain at ultimate flexural stress σ_{f_ult}
ϵ_{ij}	[%]	Strain in direction i, j
ϵ_{dmg}=ϵ_{Damage}	[%]	Strain at which damage occurs
ϵ_{max}	[%]	Maximum strain achieved
ϵ_{ult}	[%]	Ultimate achieved strain
γ_{xy}	[%]	Shear strain in the xy plane
σ_f=$\sigma_{flexural}$	[MPa]	Flexural stress
σ_{f_dmg}	[MPa]	Flexural stress for which damage occurs
σ_{f_max}	[MPa]	Maximum flexural stress
σ_{f_ult}	[MPa]	Ultimate flexural stress
σ_{ij}	[MPa]	Stress in direction i, j
σ_{dmg}=σ_{Damage}	[MPa]	Stress at which damage occurs
σ_{max}	[MPa]	Maximum stress achieved
σ_{ult}	[MPa]	Ultimate stress achieved
τ_{xy}	[MPa]	Shear stress in the xy-plane
τ_{dmg}	[MPa]	Shear stress at which damage occurs
τ_{max}	[MPa]	Maximum attained shear stress
τ_{ult}	[MPa]	Ultimate shear stress
λ_{eff}	[-]	Effectiveness ratio
$A_{overlap}$	[mm^2]	Overlapping area
$A_{FullCircle}$	[mm^2]	Area of the full circle
b	[mm]	Sandwich width
b_1	[mm]	Sandwich width in direction 1
b_2	[mm]	Sandwich width in direction 2
E	[MPa]	Young's modulus
E_f	[MPa]	Flexural modulus
F_i, F_{ij}, F_{ijk}	[MPa]	First, second and third order tensor representing the lamina strengths in principal directions
L	[mm]	Sandwich length
P_1	[N]	Midspan loading force
S	[mm]	Support span length
t_c	[mm]	Core thickness
t_s	[mm]	Sandwich thickness

List of Abbreviations

ASTM	American Society for Testing and Materials
CFRP	Class Fibre Reinforced Plastics
CoE	Cost of Energy
DIC	Digital Image Correlation
DSC	Differential Scanning Calorimetry
FE	Finite Element
FSDT	First order Shear Deformation Theory
FPB	Four Point Bending
FPF	First Ply Failure
FT	Flatwise Tension
GFRP	Glass Fibre Reinforced Plastics
GS	Grid-Scored
GSSS	Grid-Scored Sandwich Structure
ISO	International Standardisation Organisation
LPF	Last Ply Failure
PET	PolyEthylene Terephthalate
PMC	Polymer Matrix Composite
PVC	PolyVinylChloride
PU	Poly Urethane
SAN	Styrene-AcryloNitrile
SD	Scrim Down
SU	Scrim Up
TPB	Three Point Bending
UD	Uni-Directional
WT	Wind Turbine
WTB	Wind Turbine Blade

1

INTRODUCTION

1.1. PROBLEM STATEMENT

The wind energy industry is moving to larger rotors as one can benefit from a squared increase in energy yield with blade diameter, while many capital costs remain roughly the same (such as the grid connection). Nevertheless, there are hurdles in increasing the rotor size, of which the most important is caused by the square-cube law: the squared increase in energy yield comes with a cubed increase in blade mass. To overcome this technical constraint, lightweight and cheap composite materials are designed and applied that are capable of handling all expected fatigue and extreme loading patterns over the whole lifetime of the turbine. This is where composite sandwich structures come into play. This type of composite consists of 2 shells on either side of a core material that is bonded together. This core material generally is balsa wood or PVC material. To make manufacturing possible, contour finishing options have to be applied to the core material. By removing material from the core material, these contour finishing options give the material the ability to bend and take the form of the complexly curved blade shell mould. Generally in wind turbine applications, grooves are cut into the core material. These grooves are not cut throughout the whole thickness of the core since this would render the material difficult to handle and position in the mould. So by cutting these grooves, a small layer of core material is left intact to prevent the core from falling apart. As this layer is thin, it is sensitive to small damages that will inevitably form throughout the long operational lifetime of the turbine. In cyclically loaded structures such as a wind turbine blade, every form of local damage can have large consequences to the ultimate load-carrying capability of the wind turbine blade and lead to complete failure of the blade or wind turbine. Improving the damage tolerance of the wind turbine blade structure is therefore important. Damage tolerance is defined in this case as the load resistance of the structure after initial (small) failure. In order to better apply the 'safe life'[1] design philosophy, a good understanding of the failure behaviour of every substructure is necessary. The composite sandwich structure can be seen as one of the smallest substructures of a wind turbine blade. **Gaining more insight in its failure behaviour, or improving its performance can lead to significant savings in weight, cost and performance of the overall wind turbine.**
Thomsen [10] argues that by extending structural elements through the thickness of the sandwich laminate, the damage tolerance as well as the skin/core interface properties can be improved, and thus also the ultimate load-carrying capability. The concept of "Resin Links" fulfills this definition by altering the core material through drilling or cutting operations so that a flow path is created between top and bottom of the core material. Making it so that during infusion, this flow path is filled with resin and after curing, structural elements throughout the thickness of the sandwich laminate are formed by resin material.

1.2. RESEARCH OUTLINE

The purpose of this study is to get a better understanding of the failure of grid-scored sandwich structures in wind turbine applications and how the implementation of resin links affects this failure behaviour. To this extent, firstly the failure behaviour of grid-scored sandwich structures has to be studied after which it can be compared to that of the resin link implemented grid-scored sandwich structures. In order to fulfill the pur-

[1] In 'safe life' design, products are designed to survive a specific design life with a chosen reserve.

pose, the following main research question can be stated;

"What is the effect of resin links on critical loading of grid-scored sandwich structures in wind turbine applications?"

The main question leads to a set of sub-questions and sub-sub-questions, such as;

- What kind of resin link concepts are relevant for wind turbine blade applications?
  - Which concepts are available?
  - Which trade-off parameters are of importance?
- How does the implementation of resin links affect the core shear strength and flatwise failure strength of grid-scored sandwich structures?
  - What tests will be used to determine these properties?
  - What kind of failure behaviour is observed and what is the effect of the resin link sizing on the failure behaviour?

By answering all of the sub-questions, the main question can be solved. In order to do this, the structural and failure behaviour of the grid-scored sandwich structure with and without resin links in wind turbine applications will need to be defined, leading to the main research objective;

"To study the implementation of resin links on the failure behaviour of grid-scored sandwich structures in wind turbine applications by use of coupon testing and DIC."

1.3. HYPOTHESIS

After performing a literature study as presented in Chapter 3, the hypothesis can be stated that incorporating resin links, thus adding resin material, will increase the flexural modulus, shear modulus and the failure strength of the sandwich structure while decreasing its (shear) strain as seen in research on contour cut scored sandwich structures by Trofka et al. [11] Laustsen et al. [12–14], Fathi et al. [15, 16] and Thomsen [17]. Thomsen also adds that the skin/core interface properties can be improved and thus also the ultimate load-carrying capability. The hypothesis for the failure is a higher failure strength and possibly a different failure behaviour since with the implementation of resin links, new load paths are created.

The effectiveness of the resin links depends on the configuration used. For the chosen "Straight" concept, an improvement of the core-facing interface strength at the scrim-side of the structure is expected because it will in fact be linked to the other facing. Also, in general the structure's ability to handle loads is expected to improve by introducing resin links, mostly for through-thickness loads. Increasing delamination strength is hence also expected. A small effect is expected on the shear resistance and shear damage tolerance.

1.4. REPORT OUTLINE

In Chapter 2, the novel resin links concept is discussed including different possible concepts, trade-off and production of the specimens. Chapter 3 acts as a background study of the field of grid-scored structures in wind turbine application, while Chapter 4 characterises the discussed sandwich structures and their constituents. Chapter 5 discusses the experimental results of the resin link specimens and finally conclusions and recommendations are discussed in Chapter 6.

2

RESIN LINKS

2.1. THE CONCEPT

Thomsen [10] argues that by extending structural elements through the thickness of the sandwich laminate, the damage tolerance as well as the skin/core interface properties can be improved, and thus also the ultimate load-carrying capability. He also states that these structural elements should be stiff, strong and allow for load redistribution if local damage occurs. In his paper, Thomsen points out that there are already multiple material systems available that provide these kind of performance characteristics. Examples are 'X-Cor', and 'K-Cor' produced by Albany Engineered Composites.
These and other currently available concepts attempt to improve the failure behaviour of composite sandwich structures as presented in Section 3.2.5. Due to high cost, low availability, and low maturity, these options are probably not of direct interest for wind turbine blade applications, as also argued by Thomsen [10]. However he adds that similar structures adapted for use in wind turbine blade production processes could be developed.

This is where the concept "resin links" comes in. Suzlon Blades Technology proposes to investigate the effect of actually linking the facings of the sandwich structure together by means of resin. Figure 2.1a, 2.1b, and 2.1c show a composite sandwich structure with a **standard unmodified grid-scored core** where the white, green and orange parts represent respectively the GFRP facings, PVC foam and resin. Figure 2.1b shows a 'unit cell' of the grid-scored sandwich beam, where the foam has been removed for visibility of the resin grid and facings. The colored segment (non-grey) is the most basic element of the beam. By mirroring and copying this element, the whole beam can be visualised (as shown in grey).
The "Resin links" concept is an adaptation to this normal grid-scored foam core that is widely used in wind turbine blade shell applications. The cross sectional view as shown in Figure 2.1a clearly shows that the resin grid does not extend fully from the top to the bottom facing. The "resin link" idea is removing foam core material on the scrim side, so that after infusion, a resin link is formed which provides a more rigid connection between the 2 facings of the sandwich structure. Advantages with respect to the solutions proposed in Section 3.2.5 are listed below;

- Uses the same materials as currently used
  - Known material for the manufacturer
  - Proven material
  - High technology maturity
- Easily integrated in the current production process
- Cheaper

Multiple design options can be thought off to make this connection from the grid to the bottom facing, for which examples are shown in Figures 2.2, 2.3 and 2.4, where the added resin by the resin links are indicated in blue. These design options and their geometrical parameters all have their advantages and disadvantages. Different angular placements can possibly provide a better resistance to a specific type of loading or a certain

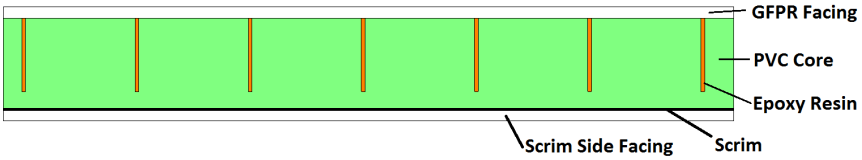

(a) Side view of a grid-scored sandwich structure - indicating facing, core, resin and scrim.

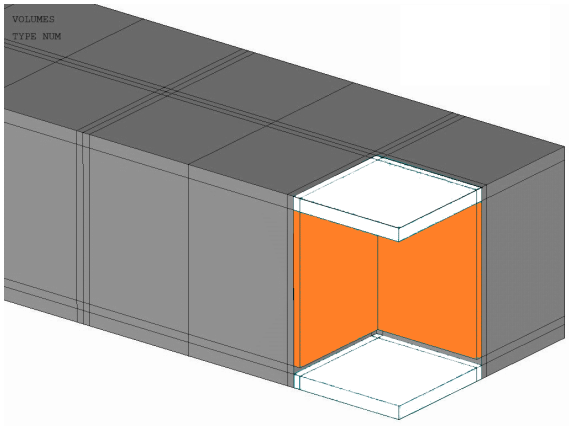

(b) Unit cell of grid-scored beam - foam hidden - shown as part of whole beam.

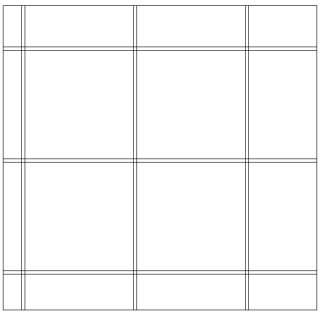

(c) Top view of grid-scored sandwich structure indicating the resin grid position.

Figure 2.1: Normal "benchmark" grid-scored core sandwich structure.

loading direction. The angular placement of, and the length of a resin link are related and have a significant influence on the added weight to the structure. A non-negligible disadvantage of the resin links concept is that by replacing a volume of foam by a volume of resin will increase the overall weight of the structure since the resin has a higher density than the foam. Larger resin links (adding more resin material) will lead to an increase in weight but also in stiffness as observed by Thomsen's analytical homogenisation analysis[17]. However, depending on the position, sizing and the amount of volume replaced, this might lead to a weight efficient increase in performance. Another advantage of this concept is that there are no new materials added to the production process, which thus only needs to be adapted slightly. Also, because of the through-thickness holes, the resin is now able to flow more freely between two sides of the sandwich structure and thus the infusability of the grid-scored structure is improved.
Tooling forms an integral part of blade manufacturing and hence manufacturability, drapeability and handling of the core needs to be taken into account. Manufacturability of the resin link core structure is an important parameter for choosing a concept since a difficult to produce structure will increase the cost. Drapeability of the core is not an issue since removing more core material will make the core more flexible. Removing material however can have a negative effect on the ease of use of the material. The core material needs to be transported and placed in the mould. If the core is too fragile, it could be damaged during handling and these imperfections could lead to a deviation from the design properties.
An increase in cost is expected for the production of this new core type. However most of the manufacturers producing grid-scored cores also offer perforated cores, other forms of contour cuts and combinations of the aforementioned. It can be assumed that the manufacturers already have the machinery and knowledge in house to be able to produce these kind of resin link cores on a (semi-) large scale. Thus the price increment is assumed to be small.

CONCEPT 1: "WALLS"

The "Walls" concept as proposed in Figure 2.2a and 2.2c looks promising. It is basically an extension of the resin grid up to the scrim side facing. Advantages of the concepts shown in Figure 2.2c(1,2) is that a minimum of weight is added while having a large connection area between grid and scrim side facing. Also the infusability is improved a lot. Manufacturing of this concept can be done by using the same circle saw used in cutting the top side grid, or by milling. Milling is definitely a slower and more expensive process than saw

cutting. Also, manufacturers of the core materials will certainly have a circle saw to their disposal, while they might not have a milling machine available. It has to be noted that the core is only held together by small regions of foam and the scrim cloth, and the machining operations induce vibrations into the core material, rendering it unstable and possibly compromising the finished product's quality. The concept variation as shown in Figure 2.2c(1) is practically infeasible because the core would effectively be cut into unconnected square foam pieces. These could be spaced properly and attached to a scrim cloth, however this process is deemed too expensive due to the extra processing step and the arguable finished product's quality of alignment. By leaving the intersections of the top saw cuts intact as shown in Figure 2.2c(2) the structure is a bit more stable during machining and might be produced in a cost and quality acceptable way. Still, a lot of material is removed which will increase the flexibility and decrease the handling of the material; the small foam connections might break or the core might get misaligned.

Although possible, this concept's configurations as described above are assumed to be difficult to manufacture in a cost and quality efficient manner. The concept variation as seen in Figure 2.2c(3), which shows multiple smaller walls, has a higher practical feasibility, however at this point the concept resembles much the "Straight" concept as discussed in the following subsection.

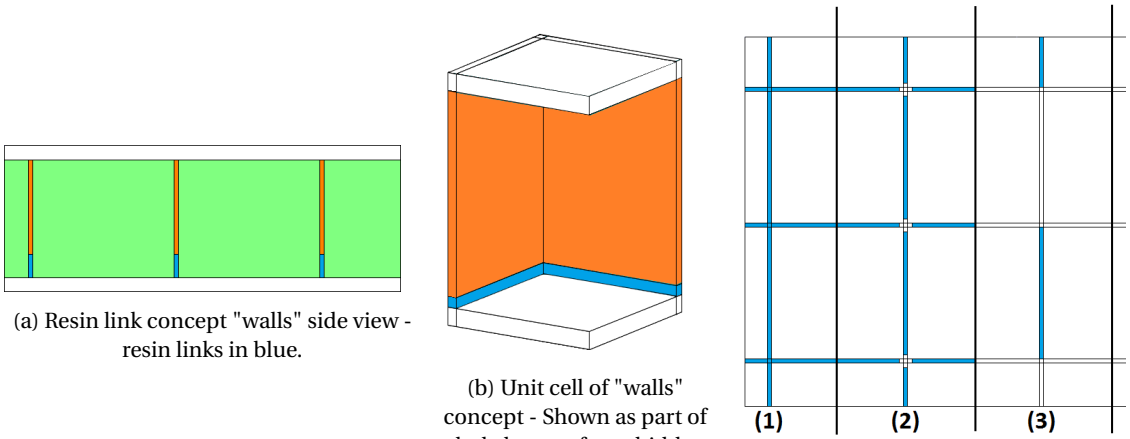

(a) Resin link concept "walls" side view - resin links in blue.

(b) Unit cell of "walls" concept - Shown as part of whole beam - foam hidden, resin links in blue.

(c) Resin link concept "walls" top view - resin links in blue.

Figure 2.2: Concept "walls" sandwich structure - side and top view - lesin links in blue.

CONCEPT 2: "STRAIGHT"

The "Straight Holes" or in short:"Straight" concept is definitely the easiest to manufacture out of the 3 proposed concepts in this chapter. A simple drill or milling machine can be used to manufacture these resin links. By adding a small amount of weight, a resin connection between the two facings can be formed. Also, the infusability of the structure is improved a lot. The structure retains its stability and its handling properties will remain sufficient, but might be compromised when too many holes are drilled into the core structure (Figure 2.3c(2)).

This concept is definitely the easiest to manufacture out of the 3 proposed concepts in this chapter, has a good handleability and drapability, and has average infusability properties in comparison to the other concepts.

CONCEPT 3: "SLANTED"

Concept "Slanted" as seen in Figure 2.4 adds the most weight out of the three proposed concepts, even when only a few resin channels are considered, their length quickly adds a lot of weight. When reducing the length, height and angle to become very small, this concept will resemble the normal "Holes concept. The performance of the "Slanted" Concept is estimated to be the highest because the angular placement gives it the ability to handle shear loads as stated before when discussing 'X-Cor' and 'K-Cor' [10]. Also, if core shear failure occurs, the angular placement of the resin links might deflect the crack as seen in Figure 3.22c, which

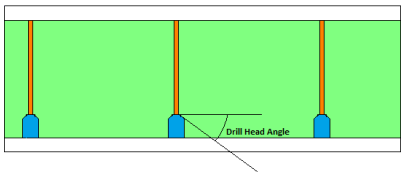

(a) Resin link concept "holes" side view - with indicated drill head angle - resin links in blue.

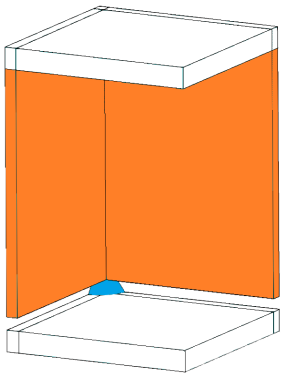

(b) Unit cell of "holes" concept - shown as part of whole beam - foam hidden, resin links in blue.

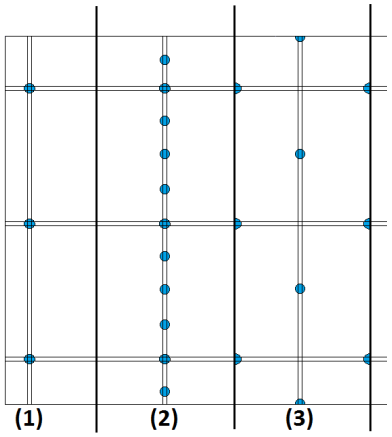

(c) Resin link concept "holes" top view - resin links in blue.

Figure 2.3: Concept "holes" sandwich structure - side and top view - resin links in blue.

is a concept developed by Jakobsen in research on improving core junction failure resistance [18]. Manufacturing this concept is assumed to be doable when using an angled jig. Handling will only be affected in a minor way and resemble the handling properties of normal grid-scored core. This concept splits up from the resin grid into 2 channels increasing the possibility for one of the channels not to be infused completely. This can be solved by halving the number of resin links in the concept, however this could possibly increase the complexity of the occurring failure mechanisms.

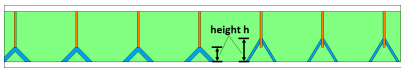

(a) Resin link concept "slanted" side view - resin links in blue.

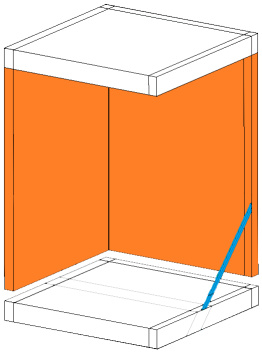

(b) Unit cell of "slanted" concept - shown as part of whole beam - foam hidden, resin links in blue.

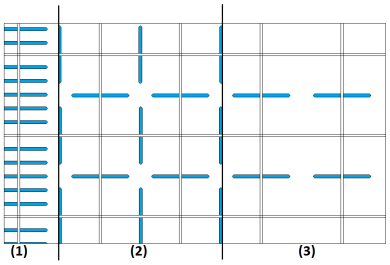

(c) Resin link concept "slanted" top view - resin links in blue.

Figure 2.4: Concept "slanted" sandwich structure - side and top view - resin links in blue.

2.2. CONCEPT TRADE-OFF AND DESIGN

The most likely to succeed concept is chosen by means of a trade-off. Trade-off criteria are; weight, manufacturability, handleability, drapeability and infusability. Cost has been omitted as a trade-off criterion because it is difficult to make an accurate estimate for the cost. It has to be noted that these trade-off criterion scores can be dependent on resin link parameters such as number of holes in each unit cell[1]. An overview of the trade-off is given in Table 2.1, where more ticks are indicating more improvement in the specific criterion.
In this trade-off, the "Holes" concept has the highest total score in the trade-off, due to its overall above av-

[1] A unit cell is defined here as the smallest cut-out section that can be used to represent the whole structure after mirroring (multiple times) in the in-plane directions. Unit cells of each concept are given in Figures 2.1b, 2.2b, 2.3b, 2.4b

erage performance in all trade-off criteria. This concept will be further investigated as the most promising concept.

Table 2.1: Trade-off of different resin link concepts.

Concept	Weight	Manufacturability	Handleability	Drapeability	Infusability	Total
"Walls"	++			++	+++	7
"Straight Holes"	+++	++	++	++	++	11
"Slanted"	+	+	++	++	+	7

As can be seen in the top view in Figure 2.5, depending on the hole size there will be an overlap of resin link and resin bridge. It is assumed that the overlapping part is the part that is contributing the most to the structure's performance. When the diameter of the hole increases, the ratio of contributing part to the whole area described by the hole is decreasing. This ratio is further referred to as the effectiveness ratio as shown in Equation 2.1.

$$\lambda_{eff} = \frac{A_{overlap}}{A_{FullCircle}} \tag{2.1}$$

In order to increase the effectiveness ratio, smaller holes should be chosen. When choosing smaller holes

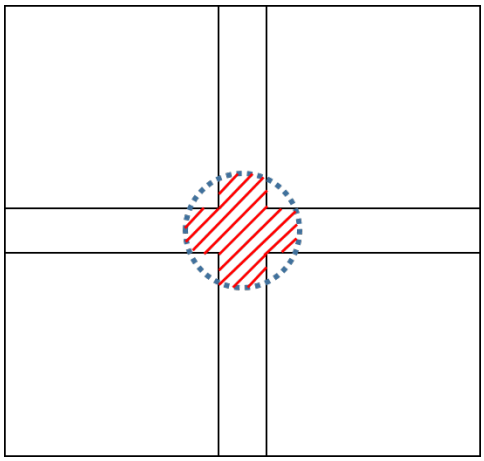

Figure 2.5: Top view of resin link structure showing overlap in resin link and resin bridge.

however, multiple holes (as shown in Figure 2.3c(2)) will be necessary to make a larger inpact on the sandwich structure's performance. It is also important to note that by drilling more holes into the foam core, the structural integrity of the sandwich structure might be compromised. Also drilling more holes increases production time. For these reasons, the choice for a single hole per resin bridge cross-section is made. The effectiveness ratio can be plotted versus an increasing hole diameter size as shown in Figure 2.6a.

Weight is an important parameter to take into account. Since one hole will be drilled in every area of $30x30mm$, drilling large holes that fill up with (the heavier than foam) resin will increase the weight of the structure. The weight increase can be plotted versus the hole diameter as shown in the graph in Figure2.6b.

Taking into account all of the above, for this project, hole sizes of $3mm$ and $5mm$ diameter are chosen to further investigate. These hole sizes have an effectiveness ratio of respectively 97.2% and 76.6%, and increase the weight of the sandwich skin structure by respectively 0.23% and 0.62%. Since resin and foam (45% and 13%) together take up about 58% of the weight of a wind turbine blade[19], these percentages can still be

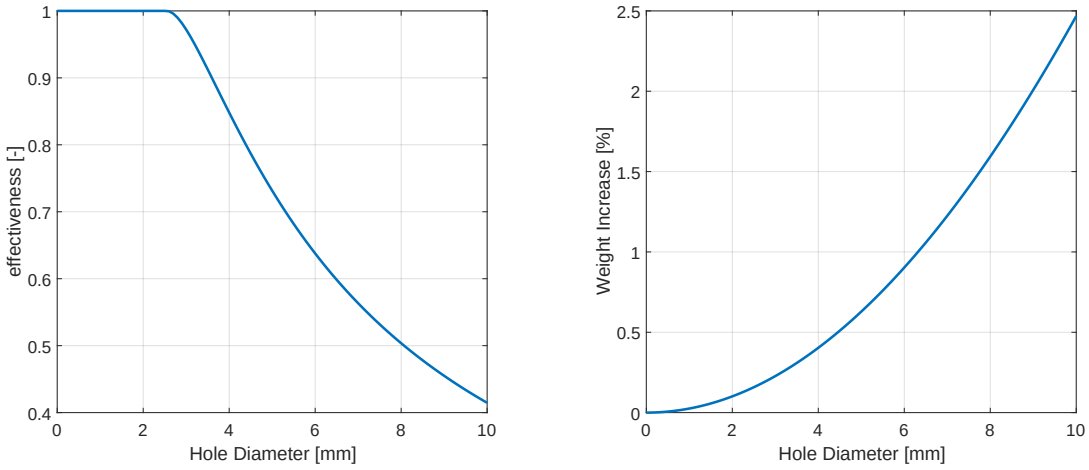

(a) Graph showing the effectiveness of area plotted versus the link diameter.

(b) Graph showing the weight increase [%] plotted versus the link diameter.

Figure 2.6: Influence of link diameter on effectiveness ratio and weight increase.

considered significant.
Choosing for holes smaller than 3mm might have an effect but the effect might be not visible enough. Choosing for holes larger than 5mm will greatly reduce the effectiveness ratio.

For the coupons, exactly the same dimensions, lay-up and materials will be used as the benchmark results. The grid-scored foam core used is even the exact same batch as the benchmark core batch. It is assumed that no degradation has occurred in the past 2 years since the material has been stored away from light sources. The only difference to be found is in the weave type of the flatwise tensional specimens which is a biax weave for the benchmark coupons and will now be changed into a triax weave. It is assumed that this will not affect the out flatwise tensional results since this test type is mostly dependent on the core and not the facings.
The holes will be drilled 3mm deep to make sure a connection is formed between scrim side facing and the resin grid. The thickness of the scrim side foam is measured to be between 1 and 2 mm, so 3mm should suffice for the drill depth.

2.3. TESTING OF THE RESIN LINK COUPONS

In order to successfully complete this project, multiple coupon testings need to be performed incorporating resin links. Testing full size wind turbine blades is very costly, so small scale coupon testing will be used to prove the concept. Raw coupon testing data for the normal grid-scored case without resin links is available from SBT and will be used as a benchmark for this project. Results for the resin link cases will be determined by performing flatwise tensile, three point bending and four point bending tests using test standards ASTM C297 and ASTM C393. These tests will yield information on the flatwise tensile strength and core shear properties of the tested grid-scored sandwich structures with resin links. For the 3 tests described above, the same testing machine will be used (the Zwick 1455 20kN test machine at the faculty of the TUDelft). A Digital Image Correlation (DIC) camera setup will also be used to investigate the strain distributions. The experimental results from testing the coupons will yield loads and displacements in a tabular format. These can be used to compute the relating stresses and strains in the structure at different loads/displacements. From the DIC measurements the actual strain across the side plane of the coupon will be measured. All coupon testing results will be compared to the normal grid-scored case (benchmark), for which testing data is available from SBT.

2.3.1. DIGITAL IMAGE CORRELATION (DIC)

Digital Image Correlation (DIC) will be used during coupon testing for accurate 2D and 3D measurements of changes in images. Concretely in this research, DIC will be used to obtain a 2D strain field of the tested coupons. The DIC setup consists of a dual camera setup (stereoscopy) where the two cameras take pictures at exactly the same time at a certain frequency. Afterwards these pictures are analysed using computer software to compute the displacements and thus strains. The software will basically track the movement of identified pixels or particles. For better particle identification, the to be tracked surface is painted with a speckle pattern as already shown in Section 2.4.
The DIC setup used can be seen in Figure 2.7a. Some practical guidelines for obtaining good results with DIC are;

- Using a (white) light source to obtain better images.
- Letting the whole setup (including lamp) warm up for half an hour, otherwise the changing heat might change the position of the sensor versus the lens and thus change the measured strains.
- The angle between the 2 cameras and the specimen should be between 20 and 30 degrees for the best measurements.

Short guidelines for setting up the cameras;

1. First opening the diaphragm completely.
2. Then focus the camera on the test specimen with lights off.
3. Next turning the light on and adjusting the diaphragm until the specimen is just not overlighted.
4. Calibrating the software using special calibration plates as shown in Figure 2.7b. Depending on the size of the field to investigate, a different calibration plate is needed.
5. Now the setup is ready for coupon testing.

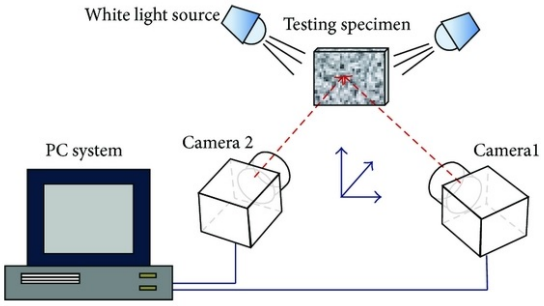

(a) DIC setup schematic[20].

(b) Calibration plates for DIC[21].

Figure 2.7: DIC schematic setup and DIC calibration plates.

2.3.2. FLATWISE TENSILE TEST

The test setup for the flatwise tensile test is shown in Figure 2.8a. As can be seen, the DIC setup requires quite a bit of space in front of the test machine. The cameras use a 12mm lens and are placed rather close to the specimen. From the benchmark tests performed by Suzlon, it is known that at fracture of the specimens no parts go flying around, so it is deemed ok to have this (expensive) equipment placed so close to the specimen. The test coupon is connected to the test machine via 2 loading blocks, these loading blocks are hinged to the supports in a 90° manner, so that the specimen is aligned automatically with the loading direction in a cardanian manner as shown in example Figure 2.8b.

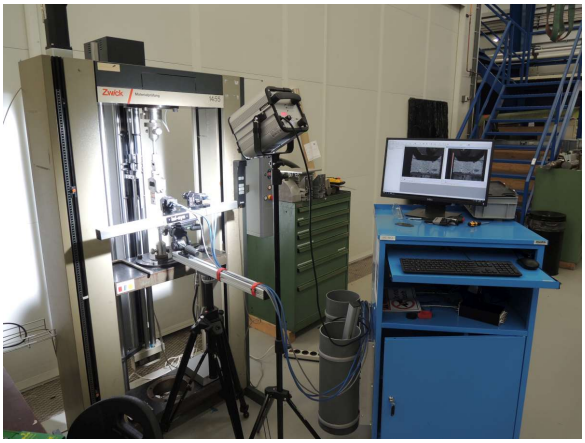

(a) Flatwise tensile test setup.

(b) Example of a 90 degree cardanian support fixture[22].

Figure 2.8: Flatwise tensile test setup and support fixture layout.

2.3.3. THREE AND FOUR POINT BENDING TEST

The test setup for the 3 point bending test is shown in Figures 2.9a and 2.9b. As can be seen, the DIC setup requires quite a bit of space in front of the test machine. The cameras use a 80mm lens and are thus placed further from the specimen than the 12mm lens used for the FT test.
The test coupon is placed in between the top and bottom support of the test machine. The coupon is aligned with the mid-point at the midpoint of the top indenter support as shown in example Figure 2.9b. The support span length of the bottom support is 360mm .

(a) TPB test setup.

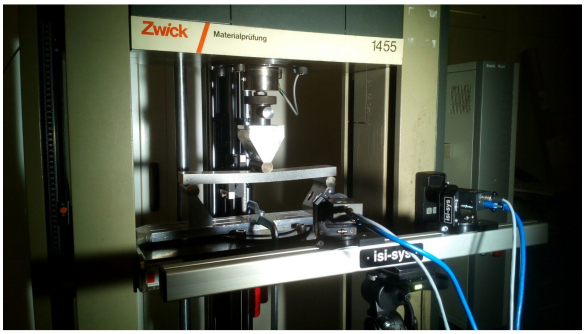

(b) TPB test setup.

Figure 2.9: TPB Test setup.

For the 4 point bending test, the test-setup is the same as for the 3 point bending setup with as difference that the top support is switched out for a support with 2 indenters spaced 180mm from each other. The bottom support stays the same with a support span length of 360mm.

2.4. PRODUCTION OF THE RESIN LINK SANDWICH PLATE AND COUPONS

Production of the sandwich plate starts with a large grid-scored sandwich plate with dimensions of 1220x 1220mm as can be seen in Figure 2.10a. The first operation to be performed is implementing the holes which (after infusion) will become the resin links. Because it is not possible to see the grid's cross-sections from the scrim side of the plate, a jig is used to exactly mark the locations where the holes need to be drilled. The holes are manually drilled into the scrim side of the grid-scored foam core as can be seen in Figure 2.10a. Half of

the plate will have 3mm holes, while the other half will have 5mm holes. The close-up in Figure 2.10b shows that the drilling of the holes does not give a very nice surface finish on the inside of the hole contours. This might affect the mechanical properties of the final sandwich structure. At this point, no attempts to make the holes smoother are made other than drilling at a low rotational speed.

(a) Drilling of holes in the 1220x1220mm PVC core plate.

(b) Close-up of a drilled hole.

Figure 2.10: Pictures of the hole drilling step of the production process.

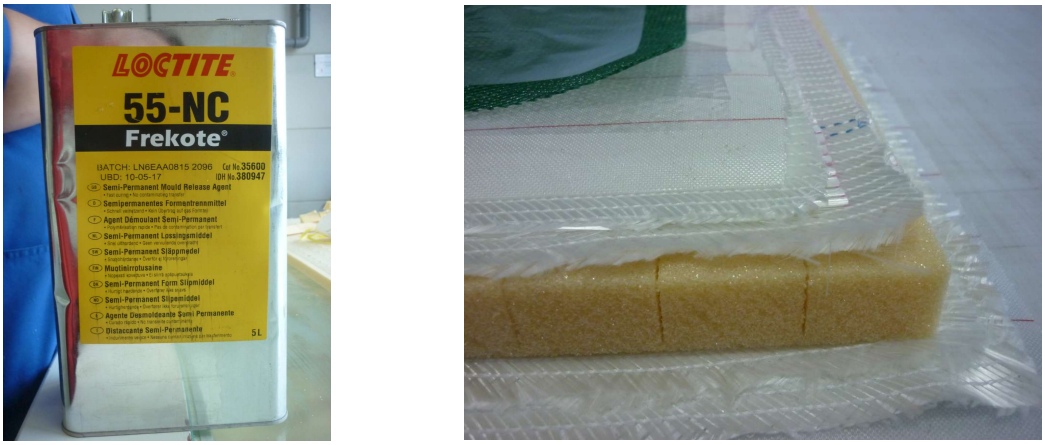

(a) Release agent used.

(b) Lay-up sequence.

Figure 2.11: Release agent and lay-up sequence.

The laminate will be laid up on a glass plate on top of a heat-controllable infusion table. Before commencing the lay-up, Loctite® 55-NC Frekote® is used to clean the table and also apply a mould release agent. This is shown in Figure 2.11a. Fibres, peel-ply, resin transfer mesh, perforated foil and breather are cut in a seperate room to not contaminate the table with loose fibres. The plies needed for the lay-up are summed up in the following shopping list, Table 2.2.

The plies are stacked on the vacuum table one by one, carefully aligning the glass plies with each other and the sandwich core. The lay-up sequence can bee seen in Figure 2.11b. Triangular core slices are added to all sides of the core plate to create a gradual slope from top side of the panel to the bottom side of the panel. On the vacuum side of the core, this slope is covered with tape to block the grid slits and make sure that the air and resin flow does not go to fast to and through these slits. This red tape is shown in Figure 2.12a. On the suction side of the plate, the glass and peel-ply plies are extended 300mm longer than the foam core material.On this end, also breather is laid down to make a connection between the glass plies and the vacuum outlet. This is shown in Figure 2.12b. The outlet is attached to the breather foil, and the inlet is attached to

Table 2.2: Types, sizes, and amount of plies needed for the sandwich plate lay-up.

Type	Size [mm]	Amount of Plies
Glass Fabric Triax $1200 g/m^2$	1600x1270	4
Peel Ply	1600x1000	4
Perforated Foil	1600x1000	1
Resin Infusion Mesh Flow Medium (Green Mesh)	1270x1270	1
Breather	small strips	3
Vacuum Foil	2400x1500	1

the green mesh at the inlet side. Here, a transverse piece of L-profile is used to distribute the inflow of resin in the transverse direction of the sandwich plate. Both in- and outlet are secured to the table using tacky tape. Finally, tacky tape is applied on the glass table around the lay-up, and vacuum foil is laid up on the tacky tape and over the dry laminate stack. The vacuum foil needs to be cut sufficiently large to accomodate creases in the foil, which are induced manually to make sure the vacuum foil is able to follow the contour of the sandwich plate.

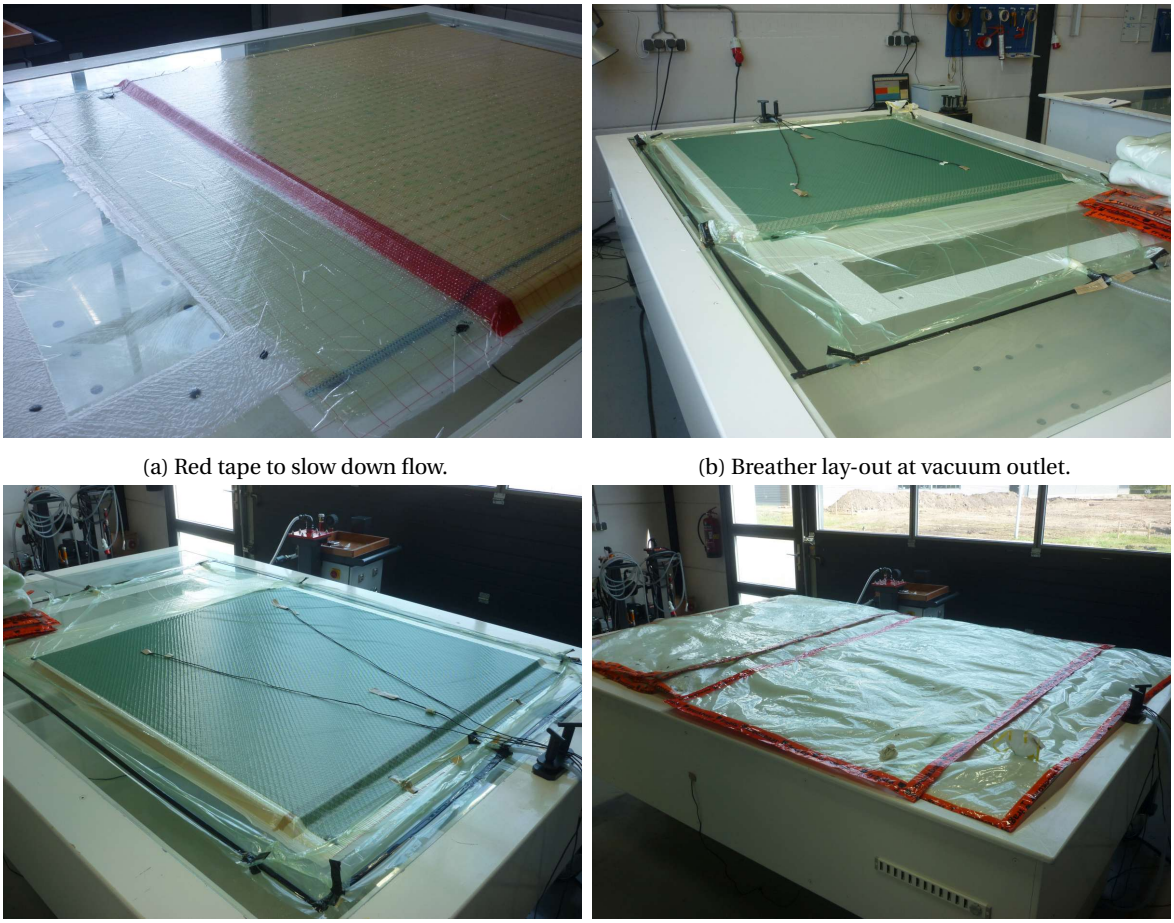

(a) Red tape to slow down flow.

(b) Breather lay-out at vacuum outlet.

(c) Thermocouples attached to the sandwich plate.

(d) Insulation of the sandwich plate during infusion.

Figure 2.12: Features of the to be infused sandwich plate.

Now, the laminate is almost ready for infusion. Thermo couples are applied on top of the vacuum foil on 3 locations of the plate and 1 thermocouple on the infusion table itself, as shown in Figure 2.12c. One thermocouple is placed on the wall of the workshop to measure the ambient temperature. Next, the laminate is put under vacuum to check for leaks. During the vacuum pulling of the laminate, the laminate is checked

for audible leaks, edges of the tacky tape are pressed, and tacky tape is checked for leaks, applying more tacky tape in possible leak locations. Then the vacuum of the laminate is checked. An air leakage of 20mbar at 5 minutes is considered acceptable, and good enough for infusion. After an hour of applying vacuum, the leakaged is measured to be a loss of 8 mbar every 5 minutes, which is well within the acceptable limit of leakage. The resin system has to be mixed in a 100:31 ratio, and around $10kg$ of resin is needed to infuse the whole plate. The resin will be mixed in 2 portions of around $5kg$ to limit the amount of heat that can build up in the buckets due to the exothermic reaction of resin and hardener. Bucket 1 contains $3.99kg$ resin and $1.12369kg$ hardener, for a total of $5.2269kg$ of resin system Y . Bucket 2 contains $3.946kg$ resin and $1.22326kg$ hardener, for a total of $5.16926kg$ of resin system Y. The 2 buckets combined contain $10.39616kg$ of resin which should be enough to infuse the plate and contain a bit extra resin as a safety margin for resin that will be left behind in the buckets and tubing.

The infusion process consists of the infusion itself, a reduction phase (lower vacuum), stabilisation, and pre-cure. The reduction phase starts when the sandwich plate is fully infused . This reduction phase reduces the applied vacuum from -1.086 bar to about -0.7 bar in 3 steps with a duration of 5 minutes between each step. After the reduction, the resin inlet is closed while the vacuum is still open. This is the start of the 30 minute stabilisation phase . After the stabilisation, the plate is pre-cured at 65 degrees celsius for 3.5 hours. During the whole infusion process, the laminate and table are insulated using blankets on top of the laminate as shown in Figure 2.12d. Also, flow front lines are drawn manually on the vacuum foil to visualise the flow process in the laminate as shown in Figure 2.13a. The outlet hose (vacuum hose) is lifted up as a safety measure to prevent resin from flowing down into the vacuum pump directly as shown in Figure 2.13b.
The temperature measured by the thermo couples throughout the infusion process is plotted in Figure 2.14a. Temperature peaks at around 13:19 can clearly be seen. These peaks occur due to the exothermic reaction exhibited by the resin system. The blue line indicates the mould temperature and shows a plateau after the exothermic behaviour. This plateau indicates the pre-cure temperature. During the first part of the pre-cure cycle, it can be seen that the laminate temperatures are still dropping from the exothermic reaction and halfway through the pre-cure settle at about $50^{\circ}C$.

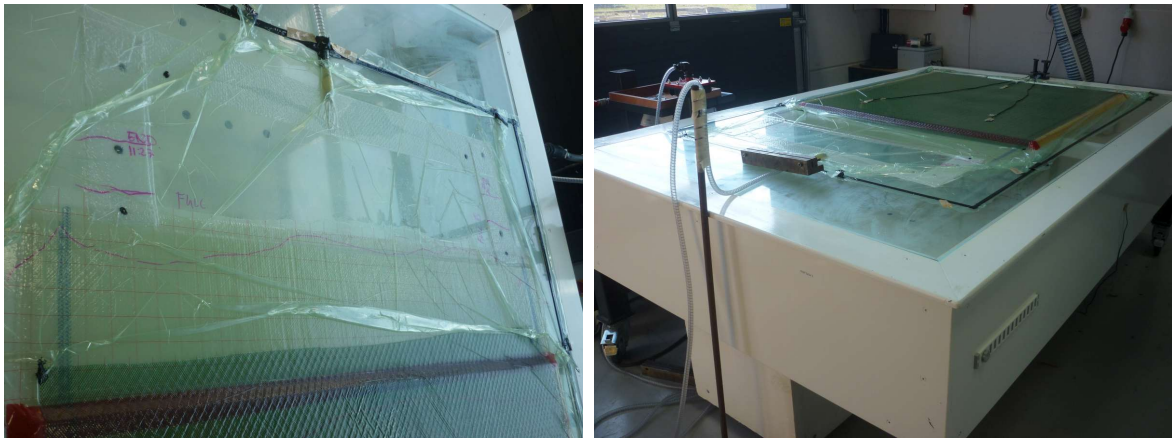

(a) Flow fronts indicated on the vacuum foil. (b) Vacuum hose tilted up as safety measure for overflow.

Figure 2.13: Infusion Process.

After pre-cure, the sandwich plate is left overnight to cool down. The plate is unpacked from the vacuum foil and inspected. Figure 2.15a shows an unexpected wavy behaviour in the green mesh on top of the sandwich plate. This behaviour does not show in the sandwich plate itself as can be seen in Figure 2.15b. A possible explanation for this behaviour is that the temperatures reached during infusion are close to the melting temperature of the green mesh or the vacuum foil .
After unpacking the sandwich plate, it is also noticeable that the plate has warped as shown in Figure 2.16. Placing the sandwich plate on a perfectly flat plate (infusion table) and placing a weight on 1 corner of the plate, the warp can be measured to be approximately $9.58mm$, as also shown in Figure 2.16b in which warp is defined as the distance between the table and the sandwich plate measured on 1 corner while the opposite corner is held down by a weight. This is assumed to be a small amount of warp considering the plate's dimen-

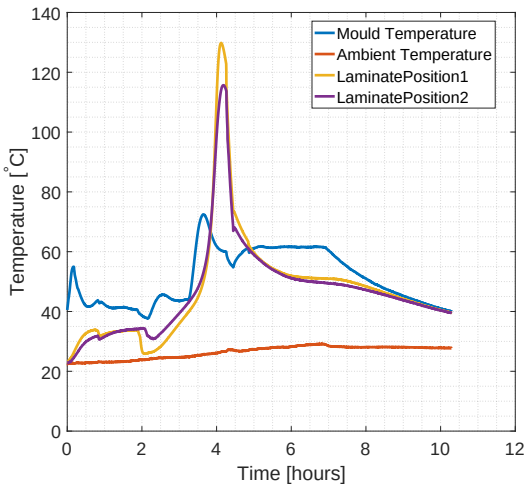

(a) Temperature during infusion and pre-cure.

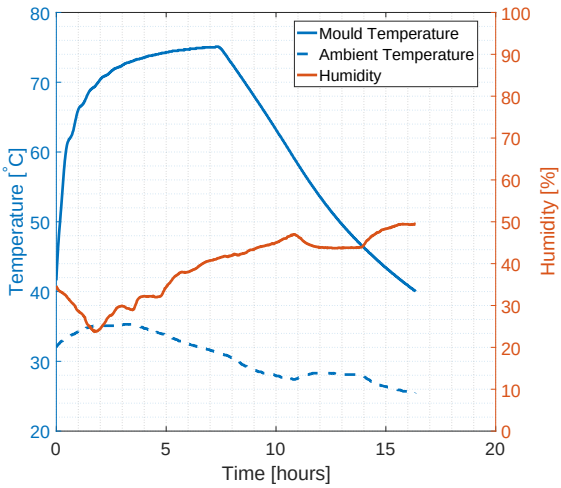

(b) Temperature and humidity during post-cure.

Figure 2.14: Temperature during pre- and post-cure.

sions.

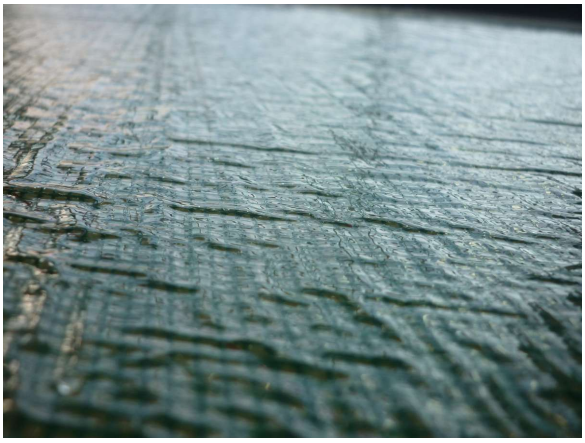

(a) Close-up of the green mesh without vacuum foil showing waviness.

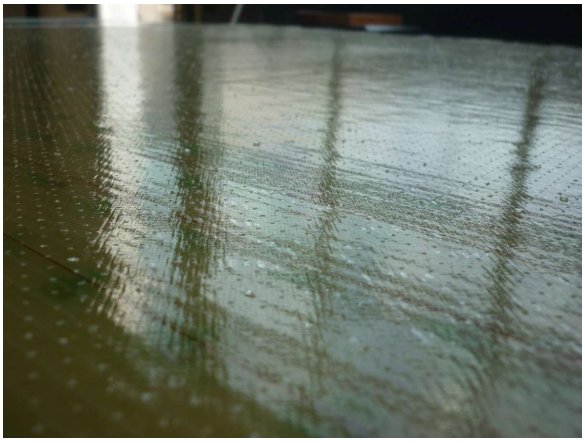

(b) Close-up of the sandwich plate without green mesh and without vacuum foil.

Figure 2.15: Inspection of the sandwich plate after pre-cure; close-up.

The sandwich plate is now ready to be cut into coupons. This is done with a table saw machine as shown in Figure 2.17a. Firstly the sandwich plate is cut into 2 sections to seperate the $3mm$ and $5mm$ cases. Each of these 2 sections is weighed and measured 3 times. An average of these measurements is used for further calculations. The dimensions of the $3mm$ plate are 704x1301x23.5mm with a weight of 7.765kg. The dimensions of the $5mm$ plate are 707x1301x23.6mm with a weight of 7.860kg. The densities of the plates are thus 3.608$kg/m3$ and 3.621$kg/m3$ for respectively the $3mm$ and $5mm$ plate, showing that the $5mm$ plate is slightly more dense, as expected. Inspecting the panels by holding them up to the daylight as shown in Figure 2.17b shows the positions of the resin bridges and resin links in the grid-scored sandwich panel, and also shows that the holes are correctly positioned at their cross-sections.

After measuring and weighing the seperate panels, the panels are further cut into coupons with the table saw. All the resulting coupons are shown in Figure 2.18a. After cutting into coupons, the coupons will undergo a post-cure cycle for which they are placed in an oven at 75 degrees celcius for 7.5 hours. The temperature graph for the post-cure cycle can be found in Figure 2.14b.

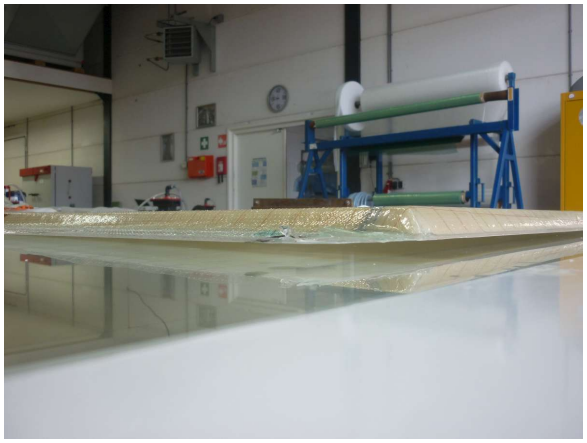

(a) Close-up of the plate showing warp. There is a clear gap between the sandwich plate and the table.

(b) Close-up of measuring the warp = distance measured with calipers between table and sandwich plate.

Figure 2.16: Inspection of the sandwich plate after pre-cure: measuring warp.

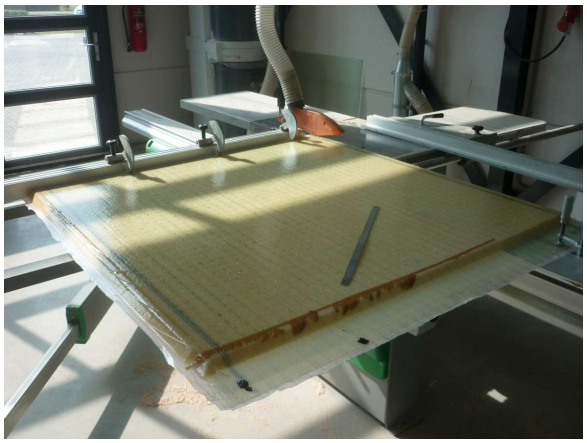

(a) Table saw.

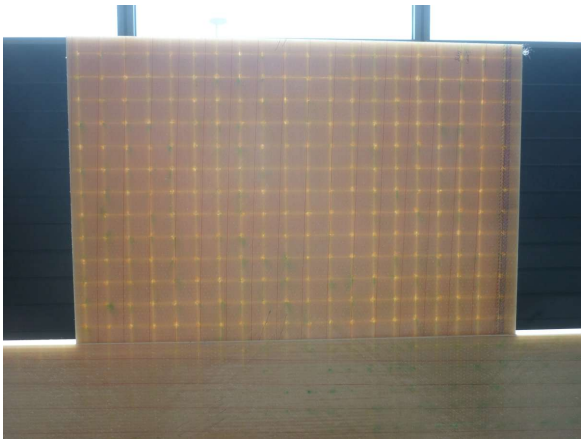

(b) Inspection of the sandwich plate by light.

Figure 2.17: Table saw and light inspection.

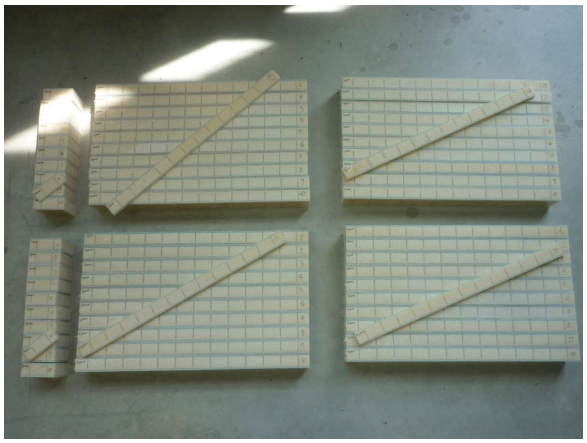

(a) All coupons cut by the table saw.

(b) Coupons ready for post-cure.

Figure 2.18: All the cut coupons ready for post-cure.

When inspecting the coupons, for example those shown in Figure 2.19a, it can be seen that the coupons are not all exactly the same size. However, the size variations are considered to be small enough to not influence the tests. Also when looking at close-ups of the sides of the coupons, such as shown in Figure 2.19b, it can be seen that the sawing machining operation has at some places removed small bits of core material.

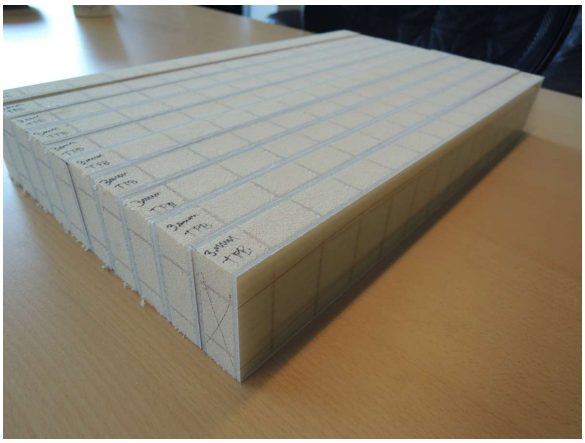

(a) $3mm$ TPB specimens showing a small deviation in widths.

(b) Close-up view of coupon sides.

Figure 2.19: Coupon inspection.

Since DIC measurements will be performed on the coupons, they will need to receive a speckle pattern. To this extent, the coupons firstly receive 2 layers of white spray paint to fill the pores of the foam core, and afterwards a speckle pattern sprayed with black spray paint. Figure 2.20a shows all the coupons laying ready for their first coat of paint. After 2 layers of basecoat, the coupons' pores are filled a lot more deeply as can be seen in Figure 2.20b .

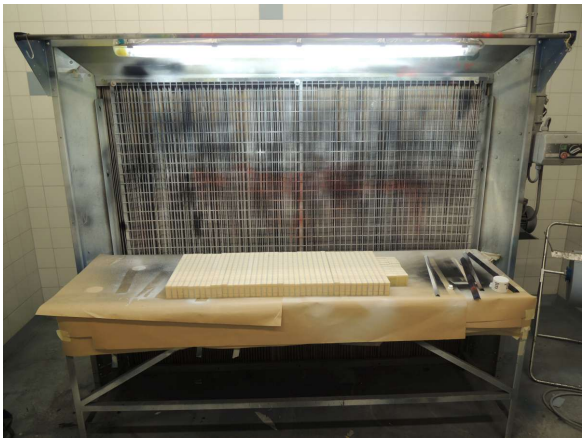

(a) Coupons ready to receive their first layer of paint.

(b) Coupons after 2 layers of white spray paint.

Figure 2.20: Coupons before and during the paint process.

The 50x50mm flatwise tensile coupons need to be glued to loading blocks at least a day in advance before testing them. In order to ensure a good bond between specimen and loading block, the loading blocks are sandblasted first and then cleaned with aceton. The difference between a fresh loading block, and a sandblasted and clean loading block can be clearly seen in Figure 2.21a. The glue used to bond the specimens to the loading blocks is the 3M Scotch-Weld 9323 B/A Structural Adhesive. In order to glue the specimens to the loading blocks in a straight manner, plastic L-profile beams and rubber bands are used to keep them nicely aligned as is shown in Figure 2.21b. The glue is mixed together with glass beads to ensure a constant bond

thickness across the specimens. After 2 hours, the glue has set and can be post-cured in the oven for 2 hours at 65 degrees celcius.

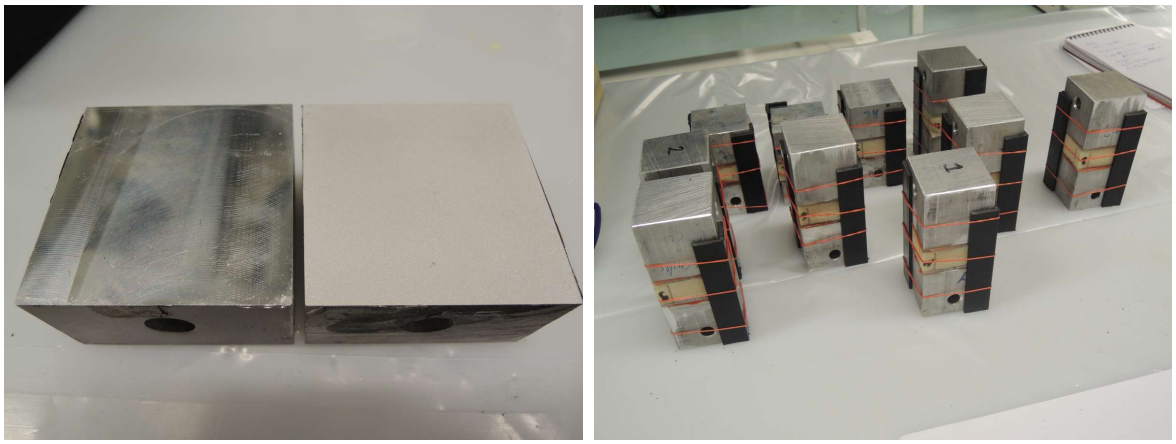

(a) Loading blocks before (left) and after (right) sandblasting.

(b) Gluing test coupons to loading blocks with L-profiles for guidance.

Figure 2.21: Flatwise tensile test loading blocks and coupons.

A thermal analysis using Differential Scanning Calorimetry (DSC) is performed on the resin system after pre-cure, and after post-cure. In this technique, the difference in amount of heat required to increase the temperature of a sample with respect to a reference sample is measured. Figure 2.22 shows graphs for the pre-cured and post-cured sample respectively. The effect of the post-cure cycle can clearly be seen by comparing these two graphs. Both graphs show a measurement starting from room temperature at 25 degrees Celcius and 0.0 heat flow. Here the measurements start while the temperature is increased up to 260 degrees Celcius. After reaching this point, the sample is cooled down gradually back to room temperature. It can be seen that during cooling down, the heat flow follows a different path than during warm-up. After reaching room temperature, a second run is started in which the sample will be heated again up til 160 degrees Celcius. For the pre-cured sample, it can be seen that the 2nd run shows a very different behaviour than its first run, whereas for the post-cured sample, the behaviour is very similar and overlapping.
From the post-cure graph, it can be seen that there is only a small area enclosed by the graphs (red arced area in Figure 2.22b) which is an indicator for the post-cure quality. The smaller, the better (consistent performance).

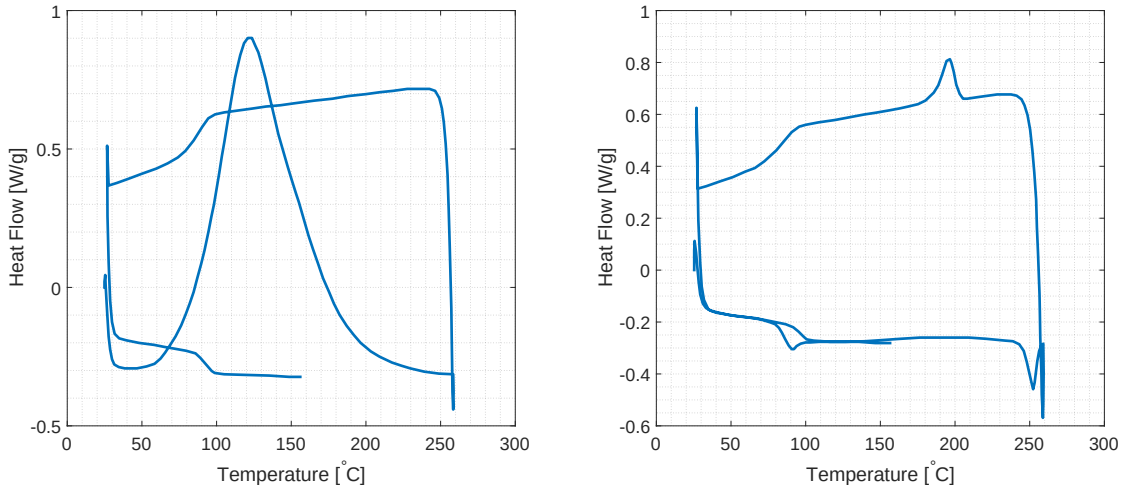

(a) Heat flow measurement of pre-cured sample.

(b) Heat flow measurement of post-cured sample.

Figure 2.22: Heat flow measurements of pre- and post-cured samples.

3

LITERATURE STUDY

In this chapter a literature study will be done on subjects related to grid-scored sandwich structures in wind turbine applications. At first, a wind turbine blade's design will be elaborated in Section 3.1 including structural lay-out, materials used and manufacturing. Contour finishing options for core materials will be considered in more detail in Section 3.1.3. Having discussed the typical design and lay-out of a wind turbine blade, failure of the complete structure and its substructures will be reviewed in more detail in Section 3.2. In this section, again special attention will be given to the failure behaviour of contour cut sandwich cores and in specific grid-scored sandwich structures.

3.1. WIND TURBINE BLADE DESIGN

In this section, focus will be on the design of the wind turbine blade and not the nacelle or supporting tower, hence not all subsystem designs will be handled in detail. Some general lay-outs and planforms of a wind turbine blade will be handled in Section 3.1.1. The materials used for construction of a blade are examined in Section 3.1.2 of which contour finishing options will be further elaborated in Section 3.1.3.

3.1.1. BLADE LAYOUT

The design process of a wind turbine blade structure starts with the aerodynamic design of the blade. The outer aerodynamic shape of the blade, together with the external wind loading conditions will lead to an estimate of the structural loading in and through the wind turbine blade. These loads can then be used to design a load bearing structure inside the confinements of the outer shell. As already stated in the previous section on wind turbine loading, the structural stability of the blade should be checked under all different normal and extreme load cases, hence the structure is optimised for fatigue and extreme loads. The most critical loads in the design of a wind turbine blade are tip deflection, buckling under extreme loading, and fatigue loading. Less critical but also important are the location of the elastic axis, location of the shear centre and the aero-elastic stability.

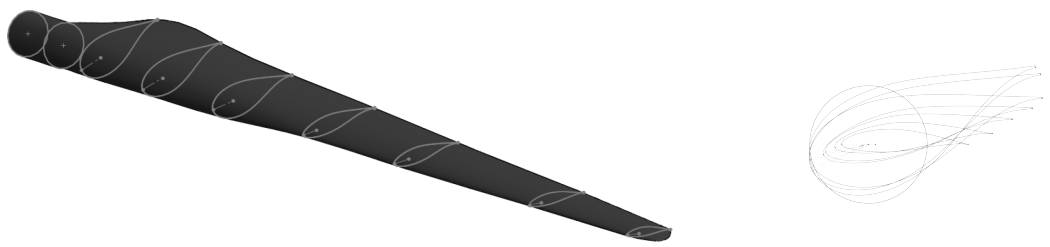

(a) Blade lengthwise layout.

(b) Blade cross-sectional layout.

Figure 3.1: Example of a wind turbine layout.

AERODYNAMIC LAY-OUT

An example of a wind turbine blade lay-out is shown in Figure 3.1. It can be seen that the cross-sectional shape and structural design of a wind turbine blade vary along its length. In the past, sometimes a blade root had a square cross-section, but nowadays, at the root of the blade the cross-sectional shape is round so that it fits the hub's circular pitch bearing. Away from the root, the blade cross-section transforms into an airfoil shape. The resultant velocity vector experienced by these airfoils is composed of the freestream wind velocity and the radial velocity created by rotation of rotor as shown schematically by the velocity triangle in Figure 3.2. This radial velocity Ωr increases linearly along the blade span towards the tip, while the freestream velocity U can be assumed to be constant across the rotor. Hence along the blade length, the apparent inflow angle will decrease and the apparent velocity will increase. Thus it can be stated that along the span of the turbine, the operating conditions vary and hence the optimal airfoil at each radial position is different. As also shown in Figure 3.1, the blade is twisted along its length to have an optimal angle attack at every position.
At the tip of the blade, in general thin airfoils with a high lift to drag ratio and high maximum lift coefficient

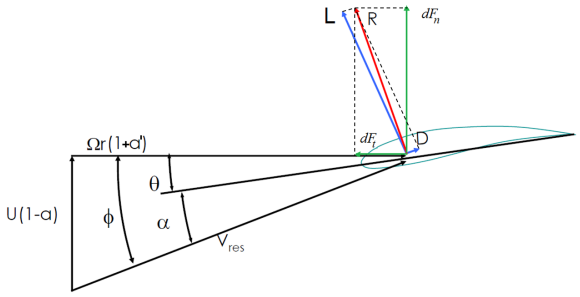

Figure 3.2: Velocity Triangle; Schematising the apparent wind experienced by a section of a wind turbine blade.

are used in order to generate an as high as possible torque. They need to be thin because the drag at the tip is most critical on the produced torque. Also for stall regulated wind turbines a thinner airfoil at the tip is more favourable because it stalls easier. The thickness of the airfoil varies from about 36% at the root to 18% at the tip. The torque is defined as lift times the radius, hence the more towards the tip, the airfoils are contributing the most to the total torque of the wind turbine and thus to the power production. Towards the tip of a wind turbine blade, the planform generally is rounded and tapered in order to reduce the tip losses flowing from the pressure to the suction side of the blade.

An important note to add is that the aerodynamic design is not necessarily a manufacturable design, or might lead to a heavy structure. For example the twist angle in a purely aerodynamic design can be around 70-80 deg, while in operational wind turbines it is mostly only 45 degrees at maximum because of producability of the spar[23]. Hence an ideal aerodynamic design is generally not manufacturable and compromises need to be made in an iterative design process while considering all design disciplines.

STRUCTURAL LAY-OUT

As already stated before, once the aerodynamic shape has been designed, the structural lay-out is designed to fit in the confinement of the outer shell and carry its loads. Also the structure has to be stiff enough so that the blade cannot bend too much and hit the tower, and make sure that loading does not change the aerodynamical properties of the blade too much leading to a possibly unfavourable design. The most critical parameters in the design of the wind turbine blade structure are extreme loading, tip deflections, buckling and fatigue loading [2]. Less critical are the location of the elastic axis and shear center, and the aero-elastic stability [2].

Since the wind turbine blade is only supported at the root, the mechanical stresses in the blade increase from tip to root, where the root section transfers all loads to the hub, nacelle and tower. In order to carry this increasing load, the structure needs to be stronger towards the root section. The longer the blade is, the higher the aerodynamic loads, but generally also the higher the weight of the blade since material needs to be added to carry the loads.
At the root the cross-section is round and generally made of a monolithic[1] composite laminate to be able to

[1] made of one material, in composites this generally means that all fibres used are of the same material

carry the high loads and transfer them to the hub. The result is a heavy and thick laminate at the root which can be in the range of 80-100mm for larger wind turbines. In new large wind turbine designs, these laminates are sometimes a glass-carbon hybrid laminate to increase the performance to weight ratio of this heavy structure. Away from the root, the cross-section changes from round to airfoil shaped.
The typical substructures that are in every design can be seen in Figure 3.3. These are girder(s), shear web(s) and a skin that is partly sandwich and partly monolithic. The objective of this integrated structure is to have various materials co-operate in an efficient way in order to contribute to a low cost of energy (CoE).

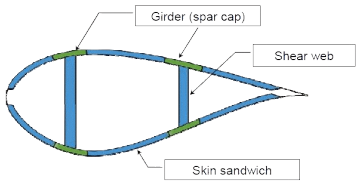

Figure 3.3: Typical wind turbine blade cross-section[2].

Different configurations of girders, shear webs and skin are used in modern wind turbines. These configurations can be split up in two concepts namely the box beam concept and the stiffened skin concept as shown in Figure 3.4. The box beam concept gives the structure a good torsional and bending stiffness, however it is a less efficient structure for lead-lag bending. In the stiffened skin concept, either the full skin is stiffened, either discrete girders are used (2 or more girders, 1 or more shear webs). This concept is more efficient for lead-lag bending and shear loads, however the joints at leading and trailing edge are more critical.

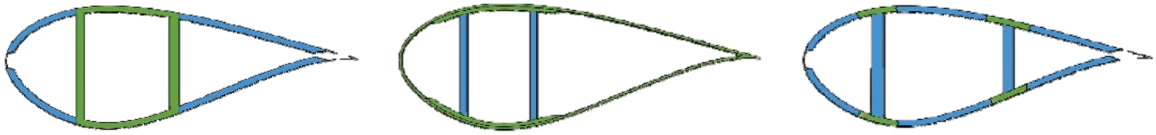

(a) Box beam concept[2]. (b) Stiffened skin concept[2]. (c) Stiffened skin concept[2].

Figure 3.4: General blade design concepts for modern wind turbines.

In these design configurations, every element is designed for a specific purpose. The girder caps are designed to carry most of the flapwise bending load, and axial normal loads. The girder webs are mainly designed to carry the flapwise shear forces and give the blade its shear stiffness in flapwise direction. They are generally constructed of a composite sandwich structure with thin bi-axial (+-45deg) face sheets. They give the blade its axial stiffness in the flapwise direction (and hence maintain a safe tower clearance). The stiffness of the blade should be tailored so that it avoids dynamic excitation of the whole wind turbine system. The edgewise bending load is carried mostly by the reinforced skin part of the blade (leading and trailing edge).

Because of the increasing load from the tip to root, the thickness and weight of the girders and shells are also increasing to cope with the increasing loads. For the composite blade structure this thus leads to ply drops in the spanwise direction of the blades (from root to tip). The materials used in the discussed blade cross-sections will be further elaborated in the next section (3.1.2).

3.1.2. MATERIALS

For the proposed blade design concepts, appropriate materials have to be used. There are a lot of parameters that might influence the choice of the material used, such as; cost, availability, processability, weight/density, strength, fatigue resistance, stiffness, fracture toughness, environmental resistance, etc. Material requirements for use in wind turbine applications are high material strength to withstand the extreme loads, high fatigue strength to cope with the cyclical load, high material stiffness to maintain the intended aerodynamic shape, buckling resistance and tower clearance, and a low density to minimise the cost and reduce gravity

forces.

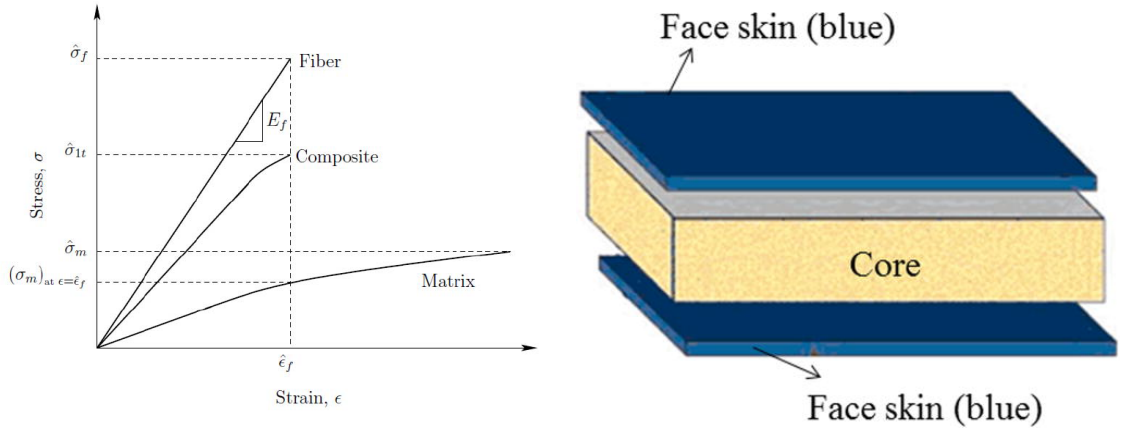

(a) Composite materials, stress-strain curve of laminate and individual constituents[3].

(b) Exploded view of a composite sandwich structure[24]

Figure 3.5: Composite - individual properties and composite sandwich layout.

Composite materials consist of (at least) two constituent materials. These materials have significantly different properties, and are combined into a new material with new properties different from the individual material properties as shown schematically in Figure 3.5a. In aerospace engineering, boats and wind turbines, polymer matrix composites (PMCs) are commonly used because of their high stiffness and strength to mass ratio as seen in Figures 3.6a and 3.6b. These composites generally consist of fibres (glass, carbon, aramid, etc.) embedded in a matrix material (polyester, epoxy, vinyl-ester, etc.). The fibres provide the composite material with high specific strength and stiffness while the matrix keeps the fibres together, transfers loads between fibres, compensates peak stresses, provides minimum distance between fibres, and protects the fibres. Generally, a composite is built up of multiple different plies or lamina, together forming the laminate. The resulting material generally has strong anisotropic properties because the material properties are highly influenced by the orientations of the embedded fibres. A big advantage of composites is the ability of choosing the fibre directions per ply and thus the material properties can be tailored to the designers specifications. In the rest of this document only polymer matrix composites will be discussed and will be simply referred to as composites.

Composite sandwich structures are a specific type of composite structure consisting of two relatively thin outer layers adhesively bonded to a relatively thick core layer as sketched in Figure 3.5b. The outer layers are usually thin but mostly stiff and strong composite laminates while the core usually is ductile and is not a high strength material. But because of the thickness of the core, the result is a high bending stiffness, lightweight, stiff and strong global sandwich structure. When applying a bending moment load to a sandwich beam, the core material will handle the shear stresses while the facings will take up this load as bending/compression stresses. Thus for composite sandwich structures, the ideal loading is transverse shear or bending. The core properties can be of a big influence on the flexural rigidity and failure mechanisms.

In modern commercial wind turbines, glass fibre reinforced polymers (GFRPs) are the most commonly used type of polymer matrix composite materials (PMCs) because of its good strength to weight ratio, high fracture toughness, fatigue resistance and thermal stability. They are used in a combination of monolithic and sandwich composites. In select structural parts of wind turbine blades, carbon fibre reinforced polymers (CFRPs) are used (eg the spar caps).
With the trend of blades becoming longer, the use of carbon fibre reinforced polymers (CFRPs) and carbon-glass hybrids is an important topic of research in the wind energy industry [10]. The most apparent advantage of CFRPs is that they are significantly stiffer and lighter than GFRPs, however the major initial drawback of CFRPs is the higher cost, lower damage tolerance and the fact that its (compressive) strength properties are greatly affected by the fibre alignment.

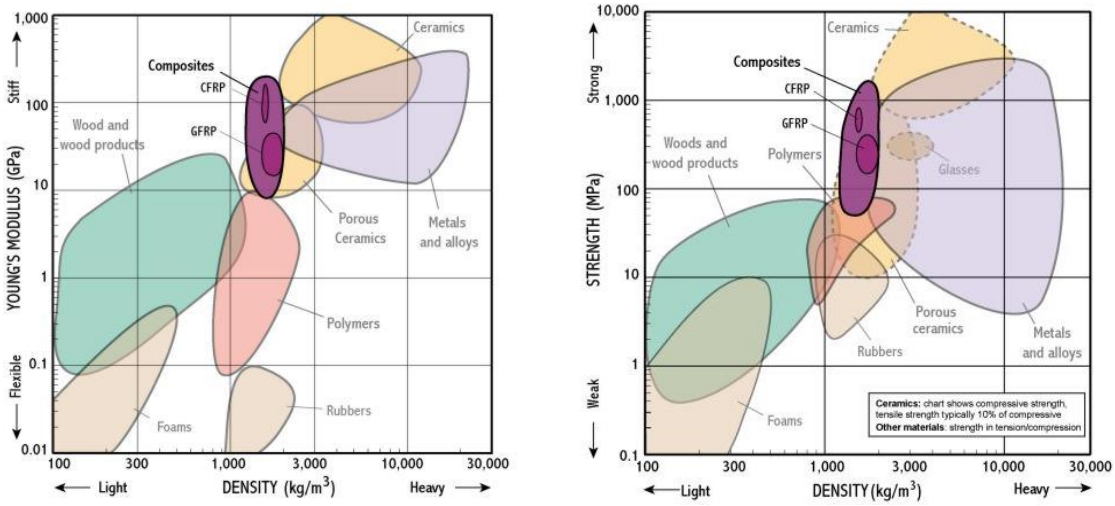

(a) Ashby plot of material categories' Young's modulus vs their density[25].

(b) Ashby plot of material categories' strength vs their density[25].

Figure 3.6: Ashby plots of material category properties.

The sandwich core materials used for wind turbine blade design may be polymeric foams (e.g. PVC, PET, SAN), balsa wood or less frequently of a honeycomb type [10]. Examples of these core types are shown in Figure 3.7. Balsa wood is the cheapest option and widely available because of the fast growing balsa tree. However disadvantages are that it is only available in a couple of densities and the structural properties are more scattered because the 'production process' cannot be controlled. Polymeric foams in wind turbines are almost solely used in the closed cell variant because of its higher properties and low moisture absorption[2] coefficient. The difference between the two cell types[3] is shown in Figure 3.7d.
The blade root laminate generally consists almost entirely out of monolithic GFRP. Some reports show that also sometimes CFRP are used in small quantities in the root section. Uni-directional and bi-axial (+-45deg in the blade's axial direction) fibres or fibre mats are generally used in approximately a 50:50 ratio.

Spar caps in wind turbine blades are consisting mostly of uni-directional (UD) fibre materials (glass or carbon) in a high thickness (can be in the range of 40-50mm). Properties of UD fibre composites are that they are linear elastic to failure, have abrupt failure (almost no plastic deformation) and have a much higher tensional strength than compression strength (of which the latter property is especially applicable to UD carbon).

The spar webs of a wind turbine are usually built up from a composite sandwich structure with a balsa or polymer foam core. The core generally is a plain sheet core since it is a straight beam. The lamina of this sandwich are mostly biaxial, oriented in +-45 degrees with respect to the lengthwise direction of the spar. The webs are designed to take up the blade's flapwise shear loads for which the +-45 degree orientation is optimal.

The blade's skins can be either sandwich panels or stiffened monolithic PMC panels. The skins in modern wind turbine blades are consisting partially of monolithic GFRP and mostly of GFRP sandwich structure. The GFRPs used here are mostly bi-axial (+-45deg in the blade's axial direction). The cores used for the sandwich structure are the same as for the spar webs. However to be used in single or even double curved shells, they are generally contour cut to facilitate the production process, as will be elaborated in Section 3.1.3.

The materials used in the above mentioned sections of the blade can vary depending on position (lengthwise, spanwise, suction/pressure side of blade), to obtain a structure better fit for the loading at this point. To this extent, for example, lamina can be added or removed, core density can be changed, core type can be changed, core material can be changed, etc.

[2] Moisture absorption generally leads to degradation of the composite sandwich structure.
[3] Same material, different production process; during the production process of the foam, air or gas is trapped. In closed-cell foams, the gas forms discrete pockets vs connected pockets in open-cell foams.

(a) PVC foam[26].

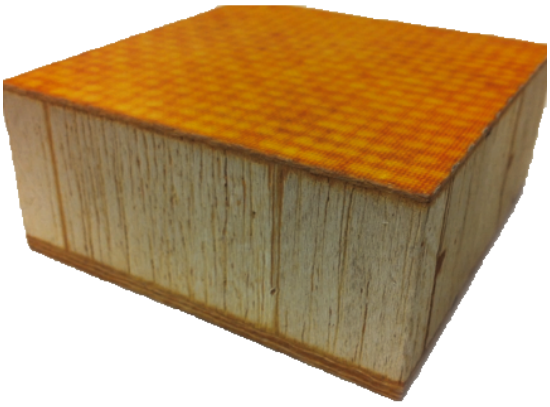

(b) Balsa wood core sandwich panel[27].

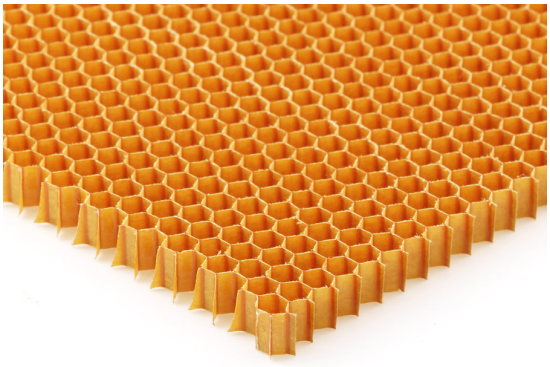

(c) Airex honeycomb[28].

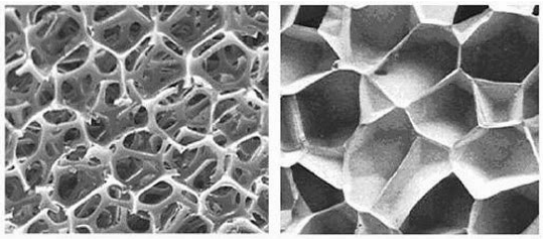

(d) Open (left) and closed (right) cell polymer core[29].

Figure 3.7: Different core types used for composite sandwich construction.

3.1.3. CONTOUR FINISHING OPTIONS

Contour finishing options are widely used in wind turbine and marine industry to improve infusability of the core material and to improve bending of the core for placement in a curved mould. These options generally describe ways in which a core material can be machined. Basically this covers the drilling of holes and cutting or milling of grooves in resulting in various configurations of perforated and (grid-)scored cores. Some examples can be seen in figure 3.8. Plain sheet cores cannot bend a lot, and hence contour cut sandwich cores are used in curved or more complex structures. The dimensions of these cuts are mostly differing per manufacturer and per application. When these cores are used in vacuum infusion processes, the grooves/holes in the core material will fill up with resin, resulting in a non-homogeneous core material with a ductile core and brittle resin reinforcements. Several sources indicate reinforcing effects of the resin channels occurring in contour cut sandwich structures. However there are also disadvantages to the use of these types of cores such as a higher resin uptake, thus higher weight, and a more complicated palette of failure modes, which will be further discussed in section 3.2.4.

Research by Trofka [11] on the effects of contour cuts on shear properties of ductile foam cores has shown that contour cuts have a significant effect on the shear properties of the sandwich panel. The study showed that for all the types of contour finishing options, while the shear strain decreased, the shear strength and shear modulus increased meaning that the sandwich construction became less ductile in general. It was also shown that the more resin throughout the core, the more the shear properties were affected, the lower the elongation before failure and the lower the energy absorption.
Fathi et al. [15] and Massüger et al. [30] have confirmed that the resin filled contour cuts have a positive effect on the resistance against transverse shear stresses, hence increasing the shear strength of the material. Also, Massuger [30] states that while the panel stiffness increases by implementing contour cuts, on the other hand the bending strength is reduced. This is confirmed in research by Trofka [11].

A short study on the fatigue resistance of different contour cut sandwich panels has been performed by Massüger et al.[30] which showed that the effect of contour finishing options has little or no effect on the fatigue properties of the structure. However it might be advisable to perform more tests on this subject before solidifying this conclusion.

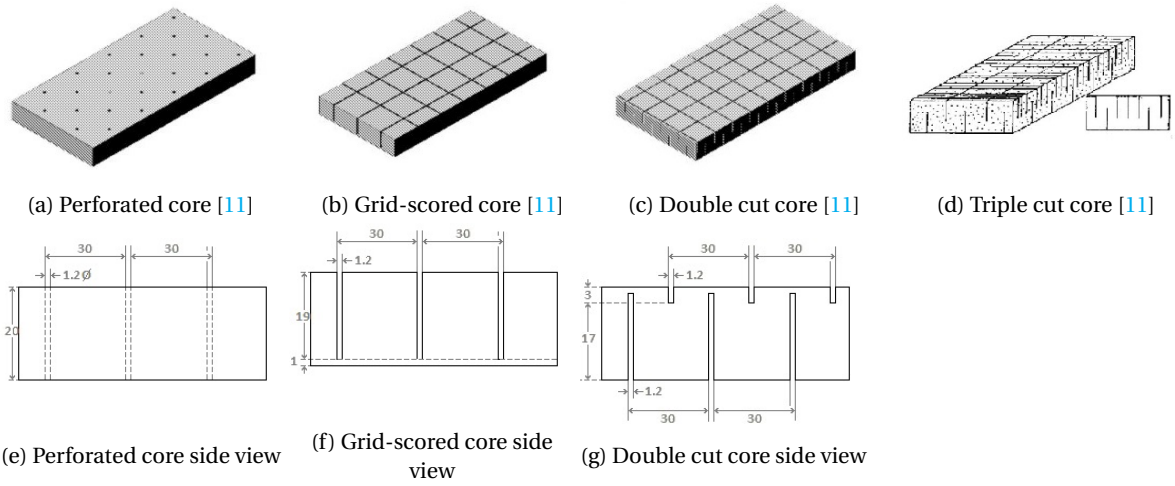

(a) Perforated core [11] (b) Grid-scored core [11] (c) Double cut core [11] (d) Triple cut core [11]

(e) Perforated core side view (f) Grid-scored core side view (g) Double cut core side view

Figure 3.8: Types of contour finishing options for closed-cell sandwich core materials

Perforated cores (Figure 3.8a) are used in composite sandwich structures because of the improved through-thickness flow of the resin for vacuum infusion processes. The perforations do however have an effect on the mechanical properties of the resulting sandwich panel [11, 31]. May-Pat et al. [31] investigated this influence on a coupon scale. They found the amount of filling of the perforations with resin has a big influence on the compression properties of the sandwich panel. Also with respect to failure reduction, the filled perforations caused a temporary minor crack arrest, after which propagation continued. May-Pat et al. [31] also concluded that defects in the structure, in specific partially filled perforations caused stress concentration which had a deteriorating effect on the mechanical properties of the sandwich panel.

Plain sheet cores and perforated cores cannot bend a lot, and hence grid-scored sandwich cores, as seen in Figure 3.8b, are used in curved or more complex sandwich structures. The dimensions of these cuts are mostly differing per manufacturer and per application. They can also be tailored on demand. Similar to the perforated cores, the grid-scored cores also improve the resin flow through the specimen during infusion, but only in longitudinal and transverse direction. During infusion, the grooves in the core material fill up with resin, resulting in a non-homogeneous core material with a ductile core and brittle resin grid. It can be assumed that, just as for perforated foam cores, resin-free locations can occur which increase the foams ability to deform under shear, leading to an inhomogeneous strain state throughout the core. Laustsen et al. [14] have added that the difference in properties between the stiffer resin grid and more ductile (foam) core, causes local stress concentrations. These might cause fracture onset and lead to failure of the whole sandwich assembly [32].

Research in the field of composite sandwich structures with grid-scored cores is not abundant. The most contributing author in the field of grid-scored cores for sandwich structures is Steffen Laustsen, who has investigated failure behavior of such sandwich panels for wind turbine applications subjected to multi-axial loading conditions as to better approach reality [14] and has developed a test rig specifically for multi-axial testing of a curved sandwich panel [33]. From these studies, he concluded with two simple failure criteria with which failure initiation in-situ[4] the resin grid for foam cored sandwich structures can be determined [14]. The first criterion resembles the tunneling crack problem and the (correct) input parameters are more difficult to determine than those for the second proposed principal strain criterion that only requires data that can be found by performing a simple uni-axial test [14]. In a previous sensitivity analysis performed by Laustsen, he concluded that the stresses and strains in a grid-scored sandwich panel are influenced the most

[4] in-situ; located in

by the radius of curvature of the panel, the slit width of the resin bridges, and the shear modulus of the foam [13]. In the same paper he concludes on the interfaces between the constituents that it is very sensitive to the radius of curvature. For higher curvatures, the stress differences between resin and foam are higher. The in-plane elastic modulus of the core also has an influence on the local stress states at both interfaces [13].
Research on edgewise loading of grid-scored sandwich panels has been done by Mathieson [34] and Manalo [5], of which the latter used phenolic core materials with densities of 850 and $990 kg/m^3$ which do not resemble wind turbine core materials with densities of between 30 and $200 kg/m^3$. The failure behavior observed was compressive skin failure. Mathieson [34] used a $30 kg/m^3$ PU core which is more comparable to cores used in wind turbine applications and observed skin wrinkling as failure behaviour.
Thomsen [17] has simplified the rule of mixtures approach in order to model grid-scored PVC core sandwich structures more easily. Basically this is a homogenisation procedure which is not of particular interest of this project's study, but might prove to be useful when doing general computations. It has to be noted however that Thomsen only validated his results in this paper with analytical and FE methods, no actual test coupon validation has been done. Laustsen [14] used this method to model the structure outside of the area of interest to reduce computation time.

Double cut sandwich core, also sometimes referred to as flexicut core as shown in Figure 3.8c, is scored in a grid pattern on both sides of the core material. If these scores are deep enough, the 2 opposing grids might intersect, leading to a perforation of the core. This perforation together with scoring on both sides improves resin flow of the structure. Similarly as for grid-scored cores, also for double cut cores the reinforcing effect is seen [11, 15, 30].

Core junctions are basically a transition from one core type to another, or a transition to the next part of core due to length constraints in manufacturing. Due to local bending of the face sheets and tension and compression of adjacent cores, large stress gradients occur at the core junctions [35, 36].
Research on core junctions might seem very closely related to grid-scored sandwich structures, however Laustsen [14] argues that "the generic core junction case does not accurately describe the grid-scored core case since the geometric and material description is not comparable". According to Laustsen the load distribution and stress concentrations are differing greatly for grid-scored and core junction cases. Nevertheless, core junctions are an important field of research because they appear in every large sandwich construction simply because the core material cannot be produced in full-scale size for large sandwich constructions.

3.2. STRUCTURAL FAILURE OF COMPOSITE SANDWICH STRUCTURES IN WIND TURBINE APPLICATIONS

In this section failure of composite sandwich structures, as used in wind turbine applications, will be discussed. Firstly the failure criteria used for composite structures will be discussed in Section 3.2.1 Next, failure of composite laminates and composite sandwich structures will be further elaborated in Sections 3.2.2 and 3.2.3 followed by a even more detailed discussion on failure of contour cut composite sandwich structures in Section 3.2.4.

3.2.1. FAILURE CRITERIA

When increasing applied force on a solid material, it will break at some point. In engineering, this is commonly referred to as failure. The point and manner in which a material fails depends on both material properties and loading conditions. Failure criteria are used to mathematically express failure for a specific material. It defines a function which indicates stress and strain spaces for a material's failed and unfailed state. An example of a failure criterion is given in Figure 3.9. It shows the maximum stress failure criterion for a certain material, where, as long as the stress state of the material is within the envelope's outlines, the material will not fail. When the material is on the edges of the enveloppe it is just about to fail, and when it crosses the border, it has failed. From the figure it can be seen that for this material, the strength in the two principal directions is the same, and the material has a higher compressive strength than tensile strength.
The maximum stress failure criterion is one of the most simple failure criteria, and is generally best fitting for isotropic brittle materials. For use in more complicated materials such as composites, these criteria are of insufficient accuracy.
Because of the anisotropic nature of composite materials, the strength of the material is not only dependent

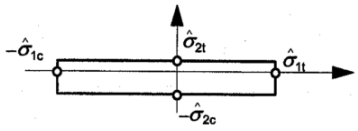

Figure 3.9: Maximum stress failure criterion for a brittle material[3].

on the magnitude, but also the direction of the applied loading. For every composite discussed further in this document, it will be assumed that every ply in said composite has orthotropic strength and stiffness properties. Because of this, a wide range of failure mechanisms is possible, and the composite can be regarded as a structure rather than as a material.

Failure criteria for a single ply in a fibre reinforced polymer composite can be divided into two main groups, namely failure criteria not associated with failure modes, and failure criteria associated with failure modes[37]. Note that the failure criteria described in these two categories can only be used to predict lamina failure, thus these do not cover all failure types.

FAILURE CRITERIA NOT ASSOCIATED WITH FAILURE MODES

The failure criteria in this category use mathematical expressions to describe the failure surface as a function of the material strengths. The basis of these expressions generally lie in the process of adjusting an expression to a curve obtained by experimental tests [37]. The Tsai-Wu failure criterion is the most general tensor polynomial failure criterion for composite materials [38], as shown in Equation 3.1, where $i, j, k = 1, ..., 6$ for a 3D case and parameters F_i, F_{ij} and F_{ijk} represent the lamina strengths in the principal directions. Usually the third-order tensor F_{ijk} is omited [39] for simplification. Since the failure of the lamina is insensitive to a change of sign in shear stresses, all terms with a shear stress to the first power are zero $F_4 = F_5 = F_6 = 0$. Ultimately leading to the explicit quadratic Equation 3.2. A visual representation of the Tsai-Wu failure criterion is given in Figure 3.10a. In this example, every combination of stresses outside of the ellipse means that the lamina fails. By varying parameters F_i and F_{ij} to better fit the Tsai-Wu curve to experimental results, other well-known quadratic failure criteria can be obtained such as [37]; Azzi-Tsai, Hoffman, Chamis and Tsai-Hill. Another visual representation including the shear strength is shown in Figure 3.10b. These criteria take into account the non-isotropy of a composite laminate, but do not take into account the non-homogeneity of the laminate, which governs the failure type.

$$F_i \cdot \sigma_i + F_{ij} \cdot \sigma_i \cdot \sigma_j + F_{ijk} \cdot \sigma_i \cdot \sigma_j \cdot \sigma_k \geq 1 \quad \text{with i,j,k=1,...,6 for a 3-D case} \tag{3.1}$$

$$F_1\sigma_1 + F_2\sigma_2 + F_3\sigma_3 + 2F_{12}\sigma_1\sigma_2 + 2F_{13}\sigma_1\sigma_3 + 2F_{23}\sigma_2\sigma_3 + F_{11}\sigma_1^2 + F_{22}\sigma_2^2 + F_{33}\sigma_3^2 + F_{44}\sigma_4^2 + F_{55}\sigma_5^2 + F_{66}\sigma_6^2 \geq 1 \tag{3.2}$$

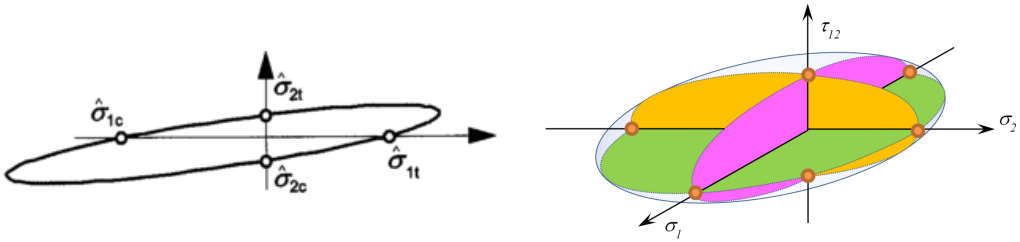

(a) Visualisation of the Tsai-Wu failure criterion

(b) Quadratic ply failure envelope[40].

Figure 3.10: Visualisation of failure criteria

FAILURE CRITERIA ASSOCIATED WITH FAILURE MODES

In these criteria, the fact that composites are non-homogeneous and lead to different failure modes of the constituents is considered. Mathematical expressions relating different failure modes with material strengths are given by these criteria. Using these criteria, predictions can be made concerning which type of failure

mode will occur, and hence can be used in a progressive failure analysis. For uni-axial states of stress, non-interactive failure criteria can be used to predict failure. Examples of these criteria are; maximum strain criterion and maximum stress criterion, which predict fibre compressive or tensional failure, matrix compressive or tensional failure, and matrix shear failure. For multi-axial states of stress, using these failure criteria might lead to errors in prediction. Interactive failure criteria in this category do take into account the interactions between stresses and strains in a ply. Every type of failure has a different mathematical expression to check for failure. Examples of interactive failure criteria are Hashin, Hashin-Rotem and Puck.

3.2.2. FAILURE OF COMPOSITE LAMINATES

So far failure criteria to predict ply failure have been discussed. From experimental evidence [41], it can be concluded that failure in a laminated composite is very often progressive in nature, occurring by a process of damage accumulation. Failure of a single lamina does not necessarily imply failure of the whole laminate. Also, when considering a full laminate instead of a single ply, other failure mechanisms can occur such as delamination and complex inter- and intralaminar interactions. In order to make a prediction for the laminate ultimate strength, progressive failure analysis needs to be considered. The easiest way to consider failure analysis is to use a stiffness reduction scheme, also known as a "ply-discount" method. This procedure considers loading increments until lamina failure, and then reduces the elastic properties of the failed ply to be zero, or some small value. After this reduction, load on the structure is increased to look for the next ply failure. The process is repeated until final ply failure is reached as schematically represented in Figure 3.11.

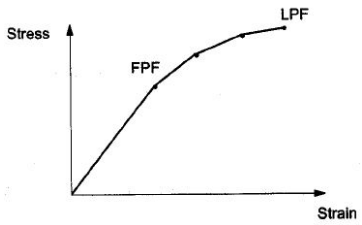

Figure 3.11: First Ply -(FPF) and Last Ply Failure(LPF) - Schematisation of progressive failure analysis[3].

3.2.3. FAILURE OF COMPOSITE SANDWICH STRUCTURES

Mahfuz [42] argues that “if the core is made from foam, the strength of the core material and the debond strength at the core-skin interface almost entirely dictates the performance of structural sandwich composites especially under flexure”. Fathi [15] adds that generally, the core is the weakest component of the sandwich structure and will fail before the facings. Daniel et al. [4], Gdoutos et al. [43], [44] and Abot et al. [45] have reviewed and discussed failure modes of composite sandwich beams. They all confirm with Fathi et al. that, out of all the factors that have an influence on the onset of failure and the failure mode, the core material’s properties are the most influential.

Composite sandwich structures are built up from different components with different properties forming a global structure with anisotropic properties. These are reasons for composite sandwich structures to display various failure modes under different loading types, or a combination of failure modes for a combination of loading types. Gdoutos et al. [43] concluded that the onset of failure for every mode is influenced by the geometric dimensions, properties of the constituents, and type of loading. Because of the nonlinear and inelastic behavior of the constituent materials, and the complex interaction of failure modes, analysis is difficult [4]. However, it is possible to predict the failure modes by stress analysis with carefully chosen failure criteria in the critical regions of the beams including 3D-effects [43]. Numerical investigation of sandwich structures is usually reliable, however prediction of failure proves still to be difficult [33].

Failure modes for composite sandwich structures exist in different types such as; tensile and compressive failure of the facings, debonding of the core-facing interface, core failure, facing wrinkling, global buckling. As stated before, it is possible that a failure mode triggers or interacts with another failure mode. The initiation of the various failure modes in composite sandwich beams depends on the material properties of the

constituents (facings, adhesive, core), geometric dimensions and type of loading. To this extent, Daniel et al. [4] argue that all separate constituent have to be fully characterised to be able to make accurate predictions of failure. When applying failure criteria, they should account for the complete state of stress at a point, including two- and three-dimensional effects [43].

In his research on failure modes of composite sandwich beams [4], Daniel et al. summarised their observed failure modes and which failure criteria to use to predict this observed failure. These findings are used as a basis for making Table 3.1, which describes which failure criteria to use to predict certain types of failure modes in composite sandwich beams with a PVC core. Further subsections will discuss in more detail the failure types with corresponding load cases and failure criteria.

Table 3.1: Failure modes in sandwich beams[4].

Mode	**Criterion**
Indentation & impact failure	Core state of stress reaches failure condition; critical compressive stress in face sheet under combined local and global bending
Face sheet tensile/compressive failure	Composite failure criterion (e.g., maximum stress, Tsai–Wu)
Face sheet debonding	Maximum shear stress of adhesive, or interfacial fracture toughness
Core failure	State of stress in foam reaches failure condition (e.g., Tsai–Wu)
Face sheet wrinkling	Face sheet stress equals critical local buckling stress
Global Buckling	von Karman plate equations; non-zero out of plane deflection

INDENTATION AND IMPACT

Daniel et al. [4] argue that indentation can be problematic for the load carrying ability of a sandwich panel. Indentation results from local compressive core failure and is followed by local face sheet bending. As discussed further in the buckling section, this will reduce the effective sandwich stiffness and lead to failure of the structure. Indentation failure and the test setup as done by Daniel et al. is shown in Figures 3.12a and 3.12b.

For composite sandwich structures, the relationship between load introduction and deflection under that load is also called contact law or indentation and plays a critical role in sandwich structures with compressible cores under both quasi-static and impact loading [45]. Laustsen et al. [33] adds that these localized loads may induce through-thickness normal stresses and induce high loads in the core material and the core-facing interface. This in contrast with high transverse stiffness cores (such as alu honeycomb) that prevent indentation under load. Abot [45] argues that this load-deflection relationship is highly influenced by the local rigidity of the beam under the load. Thus for testing of composite sandwich coupons, load introduction should be taken into account. This is generally done by using rounded, non-sharp load introduction points in the test setup.

Where indentation can be seen as a quasi-static load introduction, impact has to be seen as a dynamic load introduction. For composite sandwich structures, there are four failure modes to be identified with increasing level of impact energy, namely [46].

1. Elastic recoverable deformation; (lowest energy impact level), global deformation occurs within the elastic range without permanent (plastic) deformation.
2. Local deformation/indentation; core crushing leads to permanent local deformation followed by local bending and stretching of the face sheet (no face sheet failure).
3. Face sheet delamination and/or debonding from the core; energy below the point of penetration. In this case additional failure modes have been identified including extensive core indentation/cracking, face sheet buckling, delamination within the facesheet, and debonding between face sheet and core.
4. Penetration/perforation through the specimen; failure is initiated with matrix cracking and delaminations, after which fibre fracture occurs.

Impact on a wind turbine blade can occur in different forms, for example hail or bird strikes. These highly localized external loads might induce local yielding and/or deformation of the foam core and/or facings. This

defect in itself might serve as a basis of failure initiation for the rest of the structure. Impact damage is not always visible with the naked eye, or might not show on the outer surface of a structure, however this does not mean that the effects on the residual structural mechanical properties are non-negligible. From his research, Daniel [46] et al. conclude that structures with PVC cores generally absorb more energy from the indentation and thus are more stable than structures with balsa cores. If impact leads to plastic deformation, the structure's stiffness will be reduced and it will be more susceptible to buckling under in-plane compression [4]. In-plane compression is part of the edgewise bending load which acts on the wind turbine blade's shells and thus impact might have a deteriorating effect on the ability of the blade's shell to carry it's load.

(a) Delamination failure mode after impact[4].

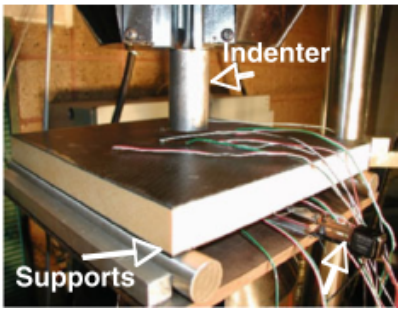

(b) Impact test setup[4].

Figure 3.12: Impact induced delamination and test setup[4].

FACE SHEET COMPRESSIVE FAILURE

Generally, composite sandwich laminates have a higher tensile strength than compressive strengths, hence compressive failure is more likely to occur. This is untrue for composite laminates with randomly ordered fibre mat facings as argued by [47].
This type of failure occurs under pure in-plane bending or bending and low shear with cores of sufficiently high stiffness in the through-the thickness direction[4, 43]. Gdoutos [43] adds that this type of failure can also occur under edgewise compression. The core needs to be of high enough stiffness to keep the facings stable enough for the sandwich to fail under compression loading. Examples of compressive facing failure in flatwise and edgewise bending are shown in Figure 3.13. This type of failure can be predicted using a simple maximum stress failure criterion for the composite facing material.

Research by Daniel et al. [4] and Gdoutos et al. [43, 44] has pointed out the under circumstances where the PVC core is sufficiently stiff enough, loading a composite beam under three or four point bending indeed leads to compressive failure of the top face sheet. Manalo [5] researched the failure behaviour of composite sandwich beams under edgewise three point bending. In this test setup, the compressive face sheet behaviour is also observed for sufficiently stiff cores. Manalo argues that the contribution of the high strength core material in the flexural and shear stiffness is significant and should be included to determine the overall behaviour of the composite sandwich beams.
Daniel et al. [4] argues that it is sufficient to predict compressive facing failure in three point bending using a simple moment equilibrium relation which does not include the core stiffness, only its thickness. This is assumed by Daniel to be true for relatively thin skins and relatively low core stiffness with respect to the facing stiffness. He adds that if the core stiffness in the through-the thickness direction is not sufficiently high, the specimen will fail in face wrinkling. Research by Gdoutos et al. reaches the same results as Daniel's research and also poses a failure criterion for compressive facing failure in terms of the applied moment, geometrical dimensions of the beam, and the facing compressive strength. Gdoutos et al. [44] also observed that for edgewise compression loading on a foam core composite sandwich structure, a softening non-linearity occurred, while for in-plane tension, a strengthening non-linearity occurred during testing. Daniel adds that either a simple maximum stress criterion or the Tsai-Wu failure criterion can be used to predict compressive facing failure.

Concluding; This type of failure occurs in beams under pure bending or bending and low shear, or under edgewise compression with cores of sufficiently high stiffness in the through-the thickness direction. The

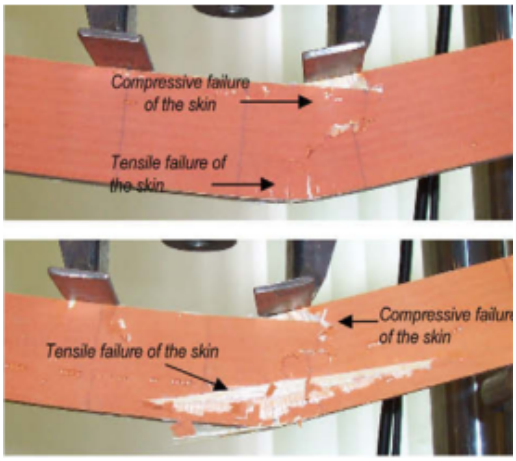

(a) Compressive and tensile facing failure in edgewise bending[5].

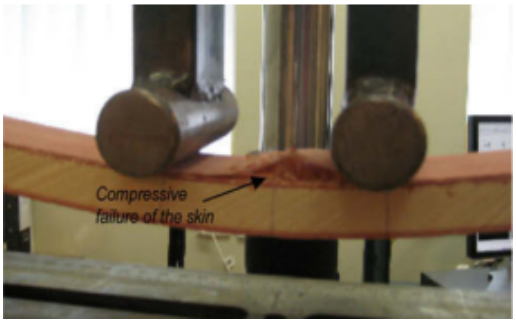

(b) Compressive facing failure in flatwise bending[5].

Figure 3.13: Core facing failure in flatwise and edgewise bending[5].

core has to be stiff enough to keep the facings stabilised until their compressive strength is reached. Tsai-Wu or maximum stress criterion can be used to predict this failure mode.

FACE CORE DEBONDING

Face core debonding, also known as face sheet debonding, signifies a failure of the interface between face sheet and core material, of which a schematic example is shown in Figure 3.16a. The face core debond strength is defined by the fracture toughness of the interface, which is by the type and properties of the materials used. Failure criteria used for prediction of this failure mode are maximum shear strength of adhesive (in case of adhesively bonding of facings to core), or inter-facial fracture toughness [4] (infusion of whole sandwich panel).

(a) Debonding of facing after edgewise compressive load[48].

(b) Debonding of facing in three point bending test[48].

Figure 3.14: Debonding of facings in edgewise compression and three point bending loading.

Experimental evidence by Triantafillou et al. [49] shows that this failure mode is only likely to occur when there is a large initial crack in the interface or when preceded by another mode of failure such as face yielding, face wrinkling or core shearing. This has been confirmed by Daniel et al. [4], who have added that it is also likely to occur under or after impact loading. Triantafillou et al. [49] have also found that failure by debonding in many cases occurs when the elastic strain energy in the faces is small compared to that in the core. They have even stated a minimum core-to-face-strain-energy ratio of 5.9 after which debonding can take place. In the same research specimens were built with different density cores with core-to-face-strain-energy ra-

tios of between 8 and 55. They concluded that crack propagation happened either in the core for lower core densities and in the face-core interface for higher core densities ($> 192 \frac{kg}{m^3}$). Generally, face core debonding is investigated starting from an initial crack introduced to the sandwich structure. Fracture mechanics was used by Triantafillou et al. [49] to predict the load for which the strain energy release rate is high enough for the crack to grow, which lead to well relatively good correlation results. However, it had some restrictions such as it did not account for cracks with a length longer than the core thickness. In later research, Zenkert [50] used an improved method to predict the debonds using interfacial fracture mechanics principles. The bi-material fracture mechanics approach as proposed by Suo and Hutchinson [51] is the most used failure prediction method for interface failure of sandwich composites used today.

Debonding of the sandwich lowers the stiffness of the structure and makes it susceptible to buckling under edgewise compression [4], as also proven in research by Hansen [52], Triantafillou et al. [49], and Avery et al. [53]. Debond fracture testing has been performed by Truxel et al. [54] using a pre-crack and a peeling test on various types of cure surface preparations and manufacturing procedures. Kardomateas et al. [55] have studied the buckling, post-buckling and debonding behaviour of a sandwich beam in bending. As seen in research by Truxel et al. [54], specimens with grooved cores showed locally high fracture resistance and temporary crack arrest by the transverse grooves, this will be further discussed further in the section on contour cut sandwich failure.

Concluding; face core debonding is generally a failure mode only occuring after initial damage or a different kind of failure. A prediction on face core debonding can be done using fracture mechanics methods or maximum shear stress of adhesive, or interfacial fracture toughness.

CORE FAILURE

As stated before, the core properties are highly determining for performance of a sandwich structure. It is primarily selected to carry the shear loading, which is usally one of the reasons to use a sandwich structure. Core failure by shear is a very common failure mode in sandwich structures. Standard test methods that can lead to core failure are; rail shear, three or four point bending, flatwise compression/tension.

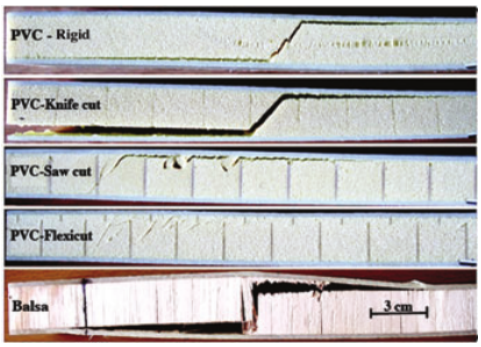

(a) Core failure in four point bending test for different core types[15].

(b) Core failure in flatwise tensile test[47].

Figure 3.15: Core failure in four point bending and flatwise tension.

For test methods such as flatwise compression/tension, rail shear, and short beams under three point bending, the core is mainly subjected to a semi-uniform shear load and failure occurs when the shear strength of the core material is reached. For longer span beams in three point bending, the normal stresses become larger until they become of equal magnitude a the shear stresses [4]. In this bi-axial state of stress, an appropriate failure criterion should be chosen. PVC core materials are not completely isotropic, they are better represented in an orthotropic way [56–58]. The Tsai-Wu failure criterion fits well for the PVC core material under bi-axial loading [43], which is confirmed by Daniel et al. [4].

Daniel et al. have observed in their research on the failure modes of sandwich beams that plastic deformation of the core, whether due to shear alone or a combination of compression and shear, degrades the

supporting role of the core and precipitates other more catastrophic failure modes, such as facing wrinkling. During testing, as long as the core material acts in its linear elastic state, shear stress (and strain) are distributed rather uniformly. When entering the nonlinear/plastic range, yielding of the core material occurs and the shear stress and strain become highly non-uniform, peaking at the center. Core failure is accelerated when compressive and shear stresses are combined, as is also indicated by the Tsai-Wu stress criterion. Yielding of the core leads to a stiffness decrease and less stability for the facings, precipitating other forms of failure such as facing wrinkling failure.

Core shear failure under three and four point bending has been investigated by multiple research sources [4, 5, 34, 43, 44, 47, 59]. They all observed core shear failure in core's midplane in the middle of the sandwich beam followed by immediate core cohesive failure in a 45 degree angle with the core mid-plane up to the facings. This can be seen in Figure 3.15a. For long beam specimens this core shear crack propagated further in a core facing debonding. Manalo [60] reported that shear failure occurred under the load introduction points and that the core shear failure mode is brittle and sudden, accompanied by a loud noise with appearance of the first shear crack. For pure bending cases, a simple stress/strain failure criterion might be sufficient for failure prediction, however the Tsai-Wu failure criterion gives a better prediction.

For flatwise tensile tests, as performed by [47] the core also failed in its midplane, but due to the uniform load distribution, the core fails cohesively and the crack propagated in the core mid-plane until complete fracture of the specimen as shown in Figure 3.15b. In load cases such as this a simple maximum stress or strain failure criterion can be used for prediction of the failure load.

It can be concluded that failure of the core generally occurs due to a shear failure and that the Tsai-Wu failure criterion can best be used to predict failure.

BUCKLING - FACING WRINKLING

As stated in the previous failure modes, often buckling or wrinkling is observed as a follow-up failure to initial core, facing, impact, or debonding failure due to a loss in stiffness or support of the initial failure. The occurrence of buckling is defined by Mahfuz et al [48] as when a structure converts membrane strain energy into strain energy of bending without any change of externally applied load. He adds that membrane forces also alter the bending stiffness of a structure, and buckling occurs where compressive membrane forces are large enough to reduce bending stiffness to zero. Buckling can significantly reduce the compressive strength and stiffness of composite structures and can lead to the development of other failure modes [6]. The presence of the core is very important for the failure load prediction because of its transverse shear effects. If these are not properly accounted for, the predicted buckling load will be very unconservative [7]. Predicting the global buckling load can be done with the von Karman anisotropic plate equations for large deflections and solving for at which load the out-of plane deflection is non-zero. The failure load is dependent on facing and core stiffness, core thickness and aspect ratio of the plate. The core's properties are very influential on the buckling load of composite sandwich plates.

Research on buckling of composite sandwich plates is abundant. However, global buckling as often observed

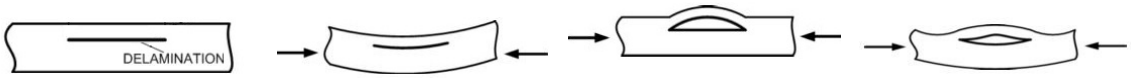

(a) Delamination (b) Global buckling (c) Local buckling (wrinkling) (d) Mixed buckling

Figure 3.16: Induced delamination and possible subsequent buckling failure modes (Figures[6]).

in composite laminates is not often reported to occur. Gdoutos et al. [43] , Daniel et al [4] and Frostig [61] argue that global buckling of a composite sandwich structure only occurs if the core is of sufficient stiffness in the through-the-thickness direction, as also confirmed by Daniel et al. [4]. Otherwise, facing wrinkling is more likely to occur, which is the typical observed type of buckling failure observed in most research on foam cored sandwich structures. Facing wrinkling is also known as local (short-wavelength) buckling
Gdoutos et al. [43] have used Heath's formula for prediction of facing wrinkling with good correlation. Face sheet wrinkling will occur when a critical value is reached for the compressive stress of the face sheet. This critical stress is dependent mostly on the facing and core moduli. Daniel et al. [4] add that this critical stress is significantly reduced when the supporting core has been degraded as also supported by research results

from Mahfuz [42], Gdoutos [62], and multiple others. Research on finding a theory for predicting the critical compressive stress for the facing after core degradation has been done by amongst others Mahfuz et al. [48] and Hasselbach et al. [63] who have investigated the effect of core-skin debonding and core density on the initiation of buckling.

To investigate buckling or wrinkling of composite sandwich structures, mostly columns under compression or beams in pure bending are investigated. For columns under edgewise uni-axial compression, the critical global buckling load is mostly dependent on the thickness and stiffness of the core. According to Gdoutos et al. [43], the facing wrinkling can be predicted satisfactorily by an expression by Hoff and Mautner [64] and defends only on the facing and core moduli. However there are a lot more models that can be used to predict facing wrinkling, each with its own range of applicability. Dobyns [65] has discussed a lot of different models, their accuracy and applicability in his research "Correlation of Sandwich Facesheet Wrinkling Test Results with Several Analysis Methods".

Edgewise loading on the wind turbine blade's shells can consist of a shear loading, in-plane bending moment, or a combination of the two. Almost all of the in-plane loading is carried by the facings while the core stabilises the facings during the loading and handles the out of plane shear and compressive behaviour [43].

Mathieson et al. [34] performed research on the in-plane bending and failure mechanism of sandwich beams with GFRP skins 1.6mm (≈ this studies skin thickness) and soft polyurethane foam core. He concluded that all specimens failed primarily by local instability of the skins near failure of sandwich beams under in-plane bending, skin wrinkling in compression was observed. The polyurethane core used in Mathieson's study has a density of $32 kg/m^3$. After normalizing for weight, its properties are about 30% less than those of the PVC foam core Divinycell by DIAB (as used in this research project).
Manalo et al. [5] also performed in-plane flexural tests on GFRP sandwich beams using phenolic foam cores of 850 and 990 $kg/m3$. This is a completely different density than Mathieson's study (~$32 kg/m^3$) and the PVC core considered for this study ($60 kg/m^3$). The facings however are all made out of similar GFRP, and are of similar thickness. The geometric dimensions of the sandwich panel however come close to the dimensions of Mathieson's study. Manalo concluded that for all specimens, the facings failed in compressive and tensile failure. The difference in results with respect to Mathieson's study is due to the much higher mechanical properties of the core material.
From Mathieson's and Manalo's research, it appears that the lay-up, geometry and material properties of a sandwich structure define the failure mode that it will encounter under flexural loading.

Facing wrinkling can occur in different types, namely symmetric, anti-symmetric and mixed mode wrinkling as can be seen in Figure 3.16. Generally symmetric wrinkling occurs. Kassapoglou [7] argues that only for very thin cores, anti-symmetric wrinkling is possible.

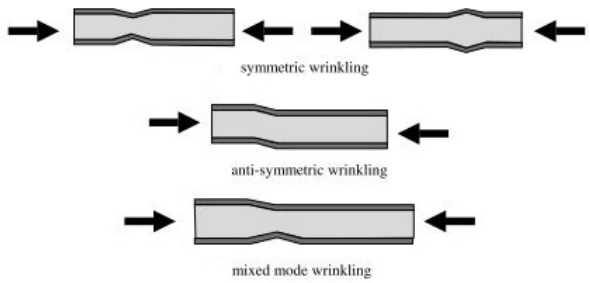

Figure 3.17: Wrinkling types for composite sandwich structures[7].

Thomsen et al. [10] argue that severe interlaminar and through-thickness normal stresses can be induced by buckling phenomena. Which determine in many cases the ultimate load-carrying capability of wind turbine blade structures [66–69]. Thomsen [10] adds that thus, composite sandwich material systems with improved/enhanced damage tolerance as well as innovative crack stopper and load introduction concepts will be key issues.

3.2.4. FAILURE OF CONTOUR CUT SANDWICH STRUCTURES

Not a lot of research has been done in the field of failure of composite sandwich structures with contour cut cores. As argued by Laustsen et al. [14], this is probably due to the fact that the strength problems (failure problems) with these types of structures are mostly related to specific applications and are thus also specific for each manufacturer. As discussed before, the contour cuts are filled with resin during production. Laustsen adds that the presence of the much stiffer resin throughout the core material can induce stress concentrations which might lead to local failure in the sandwich structure. In general, research by Laustsen et al. [13], Trofka [11], May-Pat et al. [31], and Fathi et al. [15], has shown that the introduction of resin in the core has a significant effect on the through-thickness shear properties of the resulting structure. Generally it has been concluded that the strength and modulus of the structure increase while the maximum shear strain to breakage decreases. In other words the structure behaves more brittle, less ductile, and as a result the toughness decreases, this leads to lower energy absorption and lower elongation before failure [11].

Perforated foam cores as shown in Figure 3.8a are used in composite sandwich structures because of the improved through-thickness flow of the resin for vacuum infusion processes. The perforations do however have an effect on the mechanical properties of the sandwich panels produced. May-Pat et al. [31] investigated this influence on a coupon scale. They found the amount of filling of the perforations with resin has a big influence on the compression properties of the sandwich panel. Also with respect to failure reduction, the filled perforations caused a temporary minor crack arrest, after which propagation continued. Also a light improvement in shear modulus and strength has been observed. May-Pat et al. [31] also concluded that defects in the structure, in specific partially filled perforations, caused stress concentration which had a very deteriorating effect on the mechanical properties of the sandwich panel. No criterion to predict failure for perforated pvc foam cores has been proposed by May-Pat et al.

Grid-scored cores are used to either improve (or tailor) resin flow throughout the structure during infusion, either increase the drapeability of the core, or both. Nomenclature can be different between manufacturers, but the saw-cut core is generally known as grid-scored (GS) also shown in Figures 3.8b and 3.8f. On the bottom side of the GS core, a scrim cloth (glass fibre material) is attached in order to increase the handleability of the material. The most contributing author in the field of GS cores for sandwich structures is Stephen Laustsen, who has investigated failure behaviour of such sandwich panels for wind turbine applications subjected to multi-axial loading conditions as to better approach reality [14] and has developed a test rig specifically for multiaxial testing of a curved sandwich panel [33]. From these studies, he concluded with two simple failure criteria with which failure initiation in-situ the resin grid for foam cored sandwich structures can be estimated [14].
Laustsen performed tests on single curved grid score sandwich panels as shown in Figure 3.18b. For the multi-axial tensile test, he concluded that resin bridge fracture occurred in the longitudinal bridges (in x-direction Figure 3.18b) followed by debonding of facing and resin grid. These fractions went through the thickness of the plate. The locations for resin bridge fracture occurred on the longitudinal resin bridge however did not seem influenced by the location of the transverse bridges. The fracture in the grid has been further investigated using a computed tomography scan of the resin bridge. As shown in figure 3.18a, it can be seen that the nominal slit width does not very well define the actual amount of resin in the core. Laustsen observed very small edge cracks originating from the 'open' foam cells in the resin/foam interface. An important observation from the multi-axial tensile tests is also that the transverse load component did not appear to have any significant influence on the failur load of the longitudinal resin grid. For the multi-axial compression test, he observed again a resin bridge failure, however now in the transverse grid, which caused face sheet wrinkling. Laustsen argues that because of the resin grid fracture, load redistributions occurred leading to eventually buckling of the rear facing. The uni-axial tensile test also lead to similar failure behaviour as the multi-axial tensile test. In these tests, the epoxy resins exhibited a brittle failure behaviour where failure strains were observed to be much lower than claimed by manufacturers (0.5-0.8% in stead of 6-8%). Laustsen concluded with a three point bending tests from which he observed shear failure of the core into 45 degree angled cracks through the thickness of the core, similar to plain core sandwich structures. However in this case, the crack could only propagate along the scrim side of the sandwich structure, while at the other side fracture propagation was inhibited by the resin walls. Laustsen et al. concluded with two failure criteria for fracture in-situ the resin grid. One based on a fracture mechanics approach, where the resin bridge is considered as a brittle layer constrained between two tough substrates [14]. However in order to use this criterion, intensive experimental characterisation of the effective resin grid width and the critical energy release rate of the resin are

needed as input. The second criterion he proposed is a lot simpler maximum principal strain criterion. This criterion only needs input obtained from a simple uni-axial tensile test.

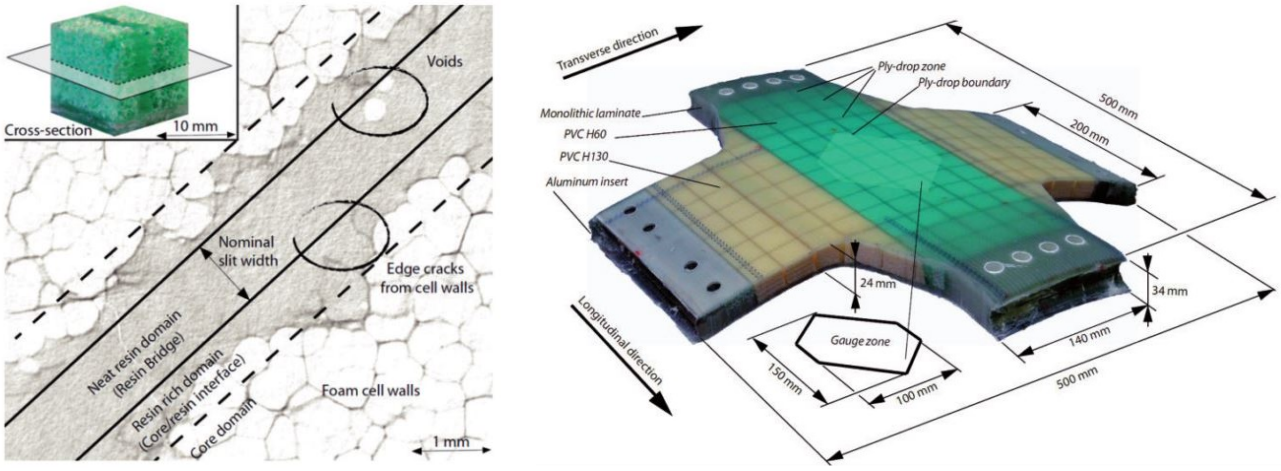

(a) Computed Tomography (CT) scan of resin bridge in foam core[14].

(b) Curved grid-scored core panel[14].

Figure 3.18: Grid-scored core structures

Fathi et al. performed four point bending tests on different plain and contour cut sandwich structures. For the grid-scored specimens they observed core shear failure followed by a 45 degree shear core crack upto the facing interface, which on the scrim side could propagate into debonding, and on the other side was hindered by presence of the resin grid. Fathi et al. also performed tests on double cut cores, also known as flexicut cores, as shown in Figure 3.8c. Failure behaviour for this core type under four point bending starts similar to failure in a grid-scored foam core, but crack propagation is hindered on both sides of the beam because of the presence of the resin grid. This structure performed better in terms of failure resistance. Fathi concluded his research stating that the stiffness and shear strength of the beams with cut cores, are increased sizeably, while at the same time sacrificing deflection at break and ductilities suggesting that the resin-filled cuts do not allow for sufficient plastic deformation of the cures under shear stresses. In her research on flexicut cores, Trofka [11] made similar conclusions. Also Truxel et al. [54] made observations on the high fracture resistance of specimens with grooved cores, where depth of the grooves was observed to be an important parameter.

3.2.5. IMPROVING FAILURE CAPACITY OF COMPOSITE SANDWICH STRUCTURES

As a conclusion to Section 3.2, solutions for improving the failure capacity of composite sandwich structures are discussed. Multiple concepts have been developed or are under development. However, the general trend is that they all add (new) material to their core, possibly reducing the specific strength of the material.

Options for improving sandwich failure behaviour are the incorporation of glass fibre reinforcement structures. This can be done in the form of glass fibre mat webs, for example Tycor and NexCore as shown in Figures 3.19a and 3.19b. During infusion, the webs are impregnated with resin, hence creating strong and stiff webs in the sandwich core. The sandwich performance increases while sacrifices are made in terms of cost, drapeability, and weight.

Z-pinning and stitching are very efficient techniques to improve interlaminar properties of composites. Z-pinning, also known as Z-pins/Z-fibres, in which thin and stiff structural pins are inserted in the laminate, typically by an ultrasonic process as also shown schematically in Figure 3.20a. Usable materials are; glass & carbon fibre, steel, etc. Stitching is done by sewing a structural thread (kevlar, polyethylene, ...) through the plies of a laminate to produce a preform with a 3D fibre structure as shown in Figure 3.20b. Although they improved interlaminar composite properties, they also cause localized fibre fracture and can cause fibre misalignment by the production process. Stitching can also be done in composite sandwich structures, where

(a) Tycor[70]

(b) NexCore[71]

Figure 3.19: Core materials with fibre web reinfocements through the thickness.

Aymerich [6] has reported an up to two times increase in buckling load. Stitching in contour cut sandwich structures is practically not feasible.

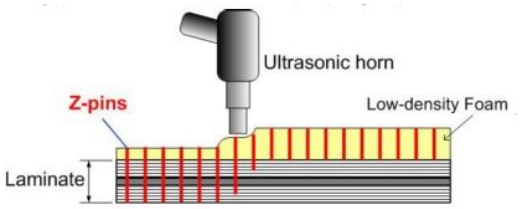

(a) Z-pinning process[6].

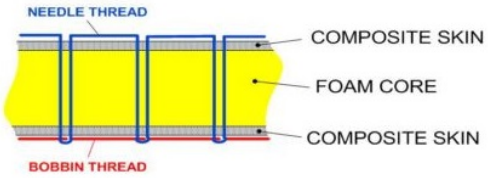

(b) Stiching of sandwich composite laminate[6].

Figure 3.20: Core materials with reinforcements through the thickness.

Related directly to wind turbine applications; Thomsen [10] argues that by extending structural elements through the thickness of the sandwich laminate, the damage tolerance as well as the skin/core interface properties can be improved, and thus also the ultimate load-carrying capability. He also states that these structural elements should be stiff and strong and allow for load redistribution if local damage occurs. Thomsen points out in the same paper that there are already multiple material systems available that provide these kind of performance characteristics. Examples are X-Cor, and K-Cor produced by Albany Engineered Composites, see schematic Figures 3.21a and 3.21b. These core materials incorporate a truss network of pultruded carbon fibre rods. Because of the angled application of the rods, the truss network carries both shear and compressive loads. Due to high cost, low availability, and low maturity, these materials are probably not of direct interest for wind turbine blade applications, as also argued by Thomsen. However similar structures adapted for use in wind turbine blade production processes could be developed.

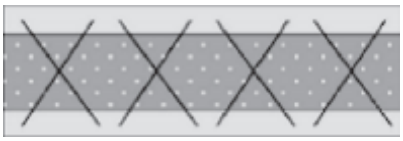

(a) X-Cor[72]

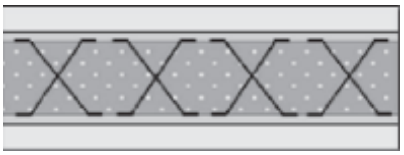

(b) K-Cor[72]

Figure 3.21: Core materials with strong fibre pin reinforcements through the thickness

Damage tolerance of composite sandwich structures has been improved by introducing Shear Keys by [73] as shown in Figure 3.22a. These keys consist of fibreglass. After core failure in shear, these shear keys act as a peel stopper, actually stopping crack growth before it can lead to peeling of the skin as shown in Figure 3.22b. A similar concept has been introduced for fracture resistance in core junctions as shown in Figure 3.22c by [18].

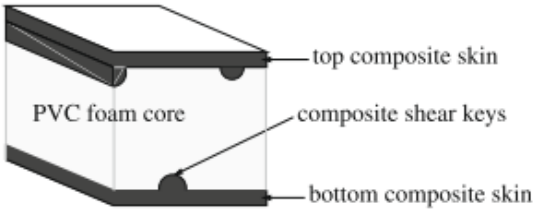

(a) Shear key concept[73].

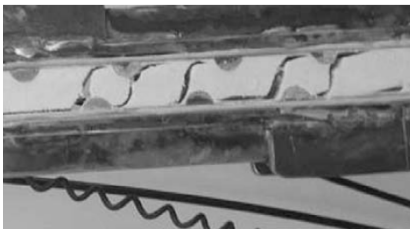

(b) Shear key concept preventing crack growth[73].

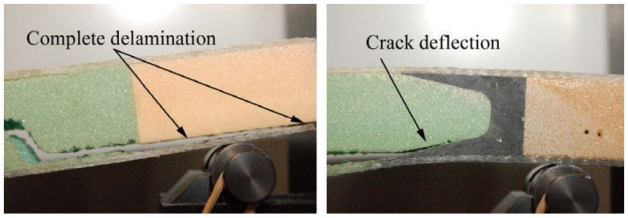

(c) Core junction crack deflection concept[18].

Figure 3.22: Concepts to stop or deflect cracks in sandwich structures

4

MATERIAL CHARACTERISATION

This chapter discusses the mechanical characterisation of grid-scored sandwich structures and its constituents. These are important to serve as a benchmark to the tested resin link structures. The facings will not be discussed in this chapter since they are of the least importance for the failure behaviour of the sandwich structure loaded in bending and in flatwise tension because they don't have a significant effect on the core shear properties and the core tensile properties. They can however for reference be found in Appendix A.1. The properties of the core are of the highest influence for the failure strength and behaviour of a sandwich structure loaded in bending or in flatwise tension. Hence the core material is important to characterise in mechanical terms. In grid-scored sandwich structures, the core is made out of a combination of PVC core material and resin material, hence both of these materials will be characterised in this chapter.
Furthermore this chapter also discusses the tests performed by SBT on normal grid-scored sandwich structures without the addition of resin links. These will further be called benchmark tests and serve as a benchmark for the resin link test case as will discussed in Chapter 5. The benchmark sandwich structure has been tested in flatwise tension/compression, edgewise tension/compression, three point bending and rail shear. Of these tests, four are discussed in the appendix and the other two are discussed in this chapter, namely the flatwise tensile and three point bending test. The first test is of importance since it yields the flatwise tensile strength, and the second test is of importance since it yields the core shear properties. Three point bending and flatwise tensile tests of the sandwich structure including resin links are discussed in Section 5 and will there also be compared to the tests discussed in this chapter.

4.1. PVC CORE CHARACTERISATION

This section discusses the characterisation of the PVC foam core material which is of importance for the research since the core properties have a significant influence on the shear and flatwise tensile properties of the resulting sandwich structure.
It has to be kept in mind that the properties of the foam can vary depending on the production batch, as also indicated by the manufacturer. In the following section, the derivation of the non-linear shear behaviour properties of the C70.55 core material as studied by Berthelot et al. will be investigated and discussed because the shear properties and behaviour are of importance for this research. Its tensile and compressive non-linear behaviour is further analysed and discussed in Sections A.2.2 and A.2.1 in the appendix.

The used core material is the Airex® C70.55 foam produced by 3A Composites, which is a closed cell, cross-linked polymer foam (PVC). The number "55" indicates its density which according to the manufacturers lies in the typical range of $54 - 69 kg/m^3$. The rest of the material's properties as specified by the manufacturer are shown in Table 4.1. From the manufacturer's data it is important to note that with a varying density, also the structural properties of the foam core material are varying. Minimum values are supplied by the manufacturer, making fail safe design easier. However it has to be kept in mind that this varying range of properties can be a cause of deviating test results. Although these properties can be used to give a good indication of the material behaviour under different load cases, they do not include any non-linear material behaviour.

Table 4.1: Airex C70.55 properties as given by the manufacturer[9].

Typical Properties for AIREX® C70.55	Test Standard	Units	Avg Value	Minimum
Density	ISO 845	kg/m^3	60	54
Compressive Strength (perpendicular to the plane)	ISO 844	N/mm^2	0.90	0.75
Compressive Modulus (perpendicular to the plane)	ISO DIN 53421	N/mm^2	69	55
Tensile Strength (in the plane)	ISO 527 1-2	N/mm^2	1.3	1.0
Tensile Modulus (in the plane)	ISO 527 1-2	N/mm^2	45	35
Shear Strength	ISO 1922	N/mm^2	0.85	0.70
Shear Modulus	ASTM C393	N/mm^2	22	18
Shear elongation at break	ISO 1922	%	16	10
Thermal conductivity (at room temperature)	ISO 8301	$W/m.K$	0.031	
Standard Sheet	Width Length Thickness	$mm \pm 5$ $mm \pm 5$ $mm \pm 0.5$	1150 2450 5 to 70	

Although these properties can be used to give a good indication of the linear material behaviour under different load cases, they do not include any non-linear material behaviour. The PVC foam shows a strong ductile behaviour where the linear behaviour of the foam is limited to only a few percent of strain, while the non-linear behaviour can go up to multiple times the linear-elastic strain range. In order to obtain a better insight in the ultimate failure strength and failure behaviour of the foam and sandwich structures, it is important to investigate its non-linear behaviour.

A study performed by Berthelot et al. [8] aims to evaluate the non-linear behaviour of foam sandwich materials in FE analyses. In the study, the same C70.55 core material as discussed above is used. Since the linear behaviour of this foam type is only limited to a few percent of strain, it is important to characterise its non-linear stress-strain response to make accurate predictions for the rest of the strain range.

SHEAR CHARACTERISATION

In order to determine the shear properties of the C70.55 core material Berthelot et al. used the ASTM C273 standard, in which the shear load was applied in parallel to the foam's top and bottom panels. This test type is also referred to as "Rail Shear". A linear displacement transducer was used to measure the relative displacement between the top and bottom support as is also shown in Figure 4.1b which shows the test setup. Five test specimens were tested with dimensions of $200mm$ x $60mm$ with a thickness of $15mm$. Information on the accuracy or the statistical significance of the results is not available.

Figure 4.2a shows obtained stress-strain curves for one of the tests. The behaviour observed is typical for closed-cell foam cores [8], where in the first portion of the graph up to a strain of approximately 4%, the foam material behaves linearly elastic as expected for both foam densities tested. Then transitions into non-linear behaviour with an almost constant stress-strain slope (plateau) until final failure at about 26% strain. The shear modulus is about $22.8MPa$ for the shown test specimen. The higher density foam type tested shows similar behaviour with a higher Young's modulus, higher plateau, and a higher failure strain. Berthelot et al. reported that the higher density foam reached a lower failure strain in contrast to the graph shown in Figure 4.2a. Arguably the behaviour shown in the figure has already reached final failure at 18% or 23% strain. It is assumed that the lower failure strain Berthelot et al. reported comes from an analysis on all 5 test specimens.

For this test, Berthelot et al. specified a test standard used. It is assumed that the shear test and it's results as given by Berthelot et al. are accurate and will be further used in this research. Their test results are summarised in Table 4.2.

CONCLUSION ON CHARACTERISATION OF THE CORE

All tests on the PVC core material that are described in this report, have not been performed by the author of this report, but by Berthelot et al. It is therefore not possible to make an accurate estimation on the quality of the tests performed by Berthelot et al. However judging by the detail in the report by Berthelot et al. and the number of quality publications by Berthelot et al., some credibility can be given. The research performed

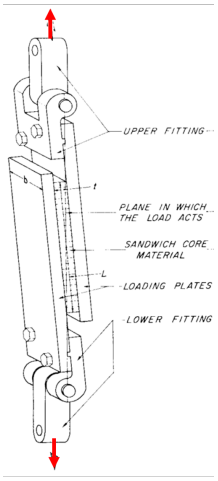

(a) ASTM C273: rail shear test [74].

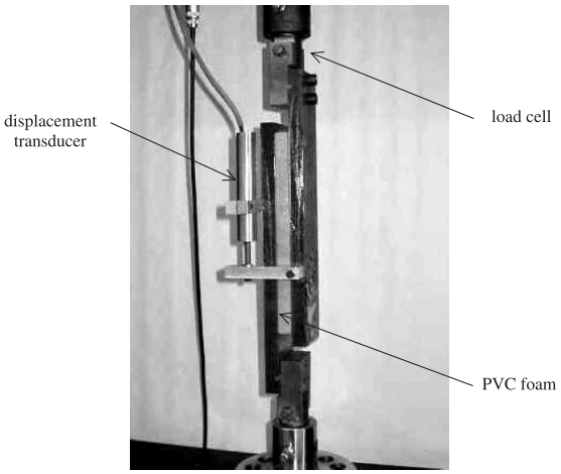

(b) Rail shear test setup [8].

Figure 4.1: Rail shear test type schematic and test setup picture.

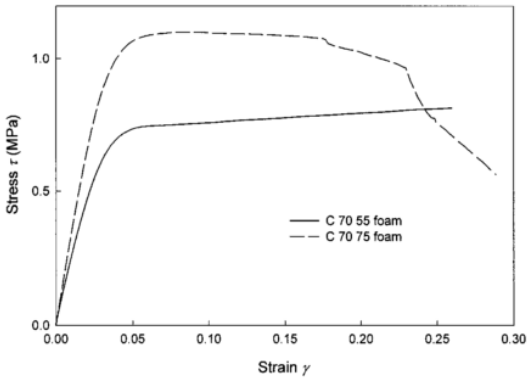

(a) Rail shear results [8].

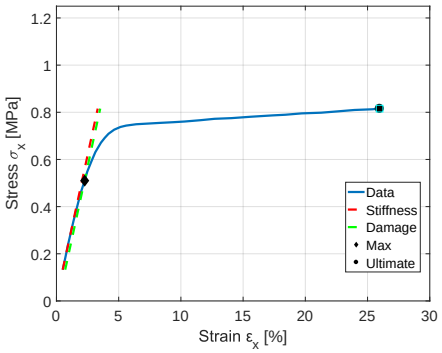

(b) Approximation to C70.55 Data Set in Figure 4.2a

Figure 4.2: Rail shear stress-strain curves from research by Berthelot et al. [8].

Table 4.2: Mechanical characteristics of the C70.55 foam subjected to through-thickness shear.

Properties	Through-Thickness Shear
Shear Modulus G [MPa]	22
σ_{Damage} [MPa]	0.6
ϵ_{Damage} [%]	2.5
σ_{Ult} [MPa]	0.8
ϵ_{Ult} [%]	27

by Berthelot et al. at least yields objective data on the core performance in contrast to the manufacturer data which might be more biased.

From all tests (compressive, tensile and shear found in Sections A.2.1, A.2.2 and 4.1), it can be stated that for small strains (up to ±3% the behaviour is linear-elastic, however the largest part of the stress strain curve shows non-linear behaviour (up to larger strains of almost 80% in compression). Berthelot et al. add as a test conclusion that the Poisson's ratio for this linear deformation is 0.42, and during non-linear deformation the effective Poisson's ratio can be close to zero. The foam material's non-linear behaviour differs depending on the type and direction of loading.
When comparing the data specified by the manufacturer and the data acquired by Berthelot et al. [8], it can be concluded that the data given by Berthelot et al. is a lot more detailed than the manufacturer's data. Also

the compressive modulus as defined by the manufacturer are seen very different than those obtained from Berthelot et al.'s tests (69MPa by manufacturer, 22 MPa by Berthelot et al.). The manufacturer states that depending on the batch of foam material, the properties might change, however a factor 3 difference in compressive modulus might indicate that the properties stated by one of the 2 parties are wrong. Hence usage of either of the data sets has to be done with care.

4.2. RESIN CHARACTERISATION

Characterisation of the resin material is of importance for this research since by implementing resin links, more resin material will be inserted into the core material. The core material is in its turn of significant importance for the shear properties and tensile strength of the sandwich structure.
Due to confidentiality agreements, the name of the used resin system cannot be specified, henceforth throughout the report, the resin system will be named resin Y. Only tensile test data is available for the resin Y material, hence characterisation will only be performed for the tensile properties. The data has been given by the supplier of the resin system. Data of 5 tested specimens is available, for which the stress-strain curves are plotted in Figure 4.3a. These results are behaving as expected for a ductile resin type material. The average stiffness, stress and strain values values for damage initiation, maximum and ultimate failure are computed and indicated in Figure 4.3b. All data is also summarised in Table 4.3.

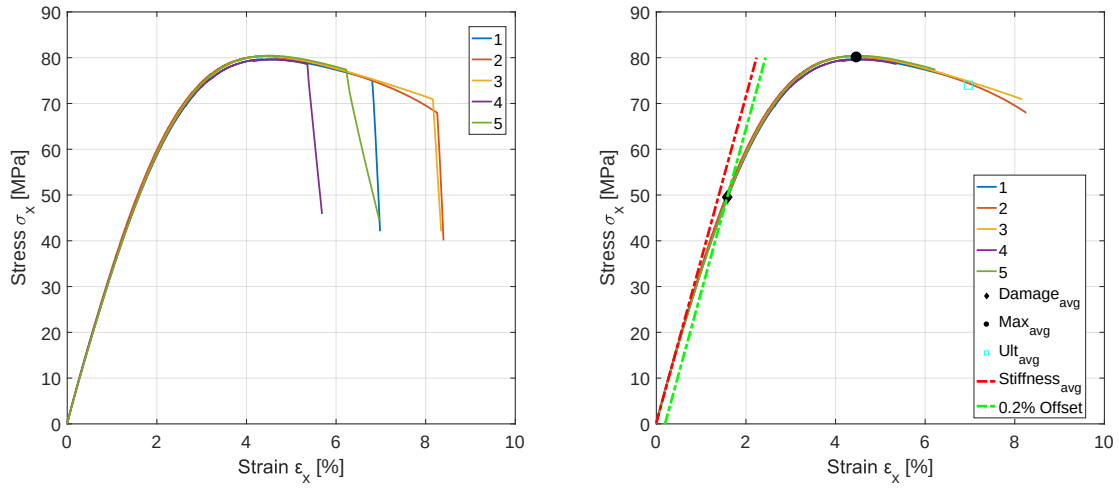

(a) Resin Y - Stress-strain curves for 5 tested specimens.

(b) Resin Y - Analysis of stress-strain curve.

Figure 4.3: Resin Y - Stress-strain data.

Table 4.3: Averaged data from all edgewise tensile characterisation tests for resin material. Units for stresses and moduli are [MPa] and units for strains are [%].

Resin, n=5	ε_{dmg} [%]	σ_{dmg} [MPa]	ε_{max} [%]	σ_{max} [MPa]	ε_{ult} [%]	σ_{ult} [MPa]	E [MPa]
Mean	1.58E+00	4.95E+01	4.47E+00	8.01E+01	6.96E+00	7.40E+01	3.57E+03
Standard Deviation	4.29E-02	1.16E+00	7.82E-02	4.00E-01	1.25E+00	4.47E+00	4.91E+01
Variance	1.84E-03	1.34E+00	6.11E-03	1.60E-01	1.56E+00	2.00E+01	2.41E+03

4.3. GRID-SCORED SANDWICH STRUCTURES - CHARACTERISATION

The sandwich panels considered in this section have the following constituents; Advantex SE1500 glass fibre mats (either bi-axial or tri-axial weave), Airex C70.55CK PVC foam core (as discussed in Section 4.1) and resin

system Y[1] (as discussed in Section 4.2). On these panels, six different tests have been performed by SBT in 2015. Of these tests, three are discussed in the appendix and the other three are discussed in this section, namely the three point bending, rail shear and flatwise tensile test. The first two tests are of importance since they yield core shear properties and the third test is of importance since it yields the flatwise tensile strength. Three point bending and flatwise tensile tests of the sandwich structure including resin links are discussed in Section 5 and will there also be compared to the tests discussed in this chapter.

4.3.1. FLATWISE TENSION

The used test method is "ASTM C 297 - 94" or "Standard Test Method for Flatwise Tensile Strength of Sandwich Constructions"[75]. The test setup is similar to the one shown in Figure A.10. IBy applying this test method to coupon testing, its flatwise tensile strength and modulus can be obtained. This test is also often used for an indication of the quality of the bond between core and facings. The constituents used in the sandwich coupons are Advantex SE1500 bi-axial glass fibre mats, Airex C70.55CK PVC foam core and resin system Y. These materials are compliant for use with this test standard. For this test, five test specimens were tested. Test specimen dimensions are $100mm$ x $100mm$ with a total thickness of $22.20mm$ on average. The design and actual (measured) coupon dimensions are given in Table 4.4, which are also compliant for the test standard.

Table 4.4: FT: Design and actual coupon dimensions. Average values based on 5 test coupons.

Dimension	Design Value	Measured Value
Width1 b_1 [mm]	100	99.72
Width2 b_2 [mm]	100	99.54
Sandwich thickness t_s [mm]	22	22.20
Core Thickness t_c [mm]	20	20.02

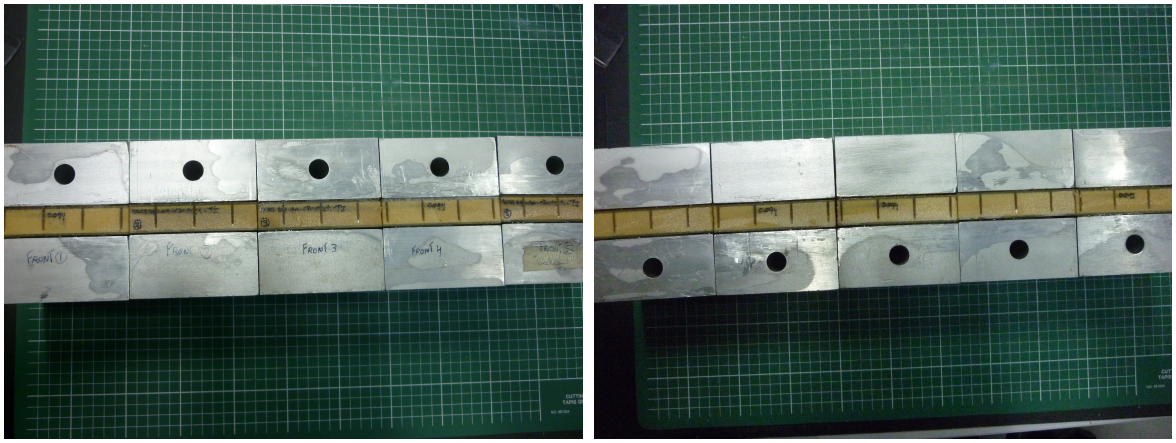

(a) Side view 1 of FT test specimens.

(b) Side view 2 of FT test specimens.

Figure 4.4: Flatwise compression (FT) specimens.

Figures 4.4a and 4.4b show the coupons from a front and a side view. Figure 4.5a shows a specimen in the test setup during loading. Figures 4.5b, 4.6a and 4.6b show the specimens from a top, front and side view after final failure. It can be seen that coupons 1 and 2 have failed due to adhesive failure of the coupon to the loading block. These measurements should thus be omitted from further analysis. The three remaining specimens all failed in tensile core failure at the location of the scrim, as could be expected.

Characterisation analysis on these test specimens will be done in a similar manner as before. The tensile stress is acting on the full area of the facing and hence is simply equal to $\sigma_{compressive} = Force_{applied} / Area_{facing}$. The stress-strain curves obtained in this manner are shown in Figure 4.7 and the characterisation analysis of these results in terms of Young's moduli and damage/max/ult stress/strain are summarised in Table 4.5. An important note to be made is the visible toe region for which a correction is necessary as also discussed in

[1] Resin system name cannot be specified due to a confidentiality agreement with Suzlon Blades Technology

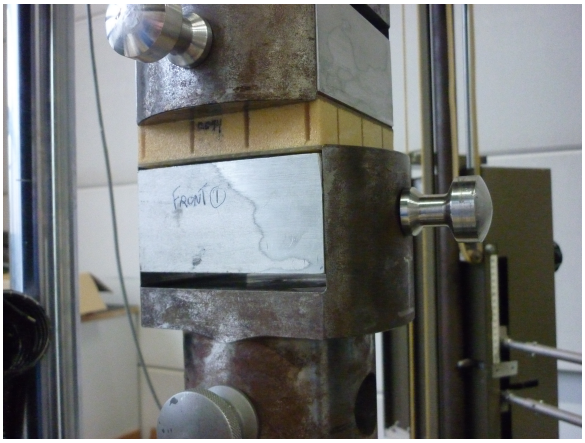

(a) FT specimen during test.

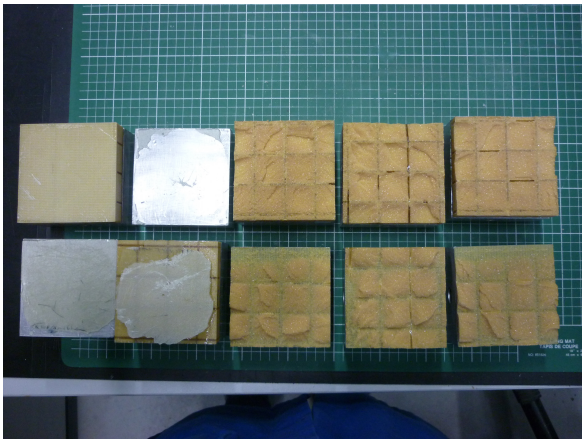

(b) FT specimens top view after test.

Figure 4.5: Flatwise compression specimens during loading.

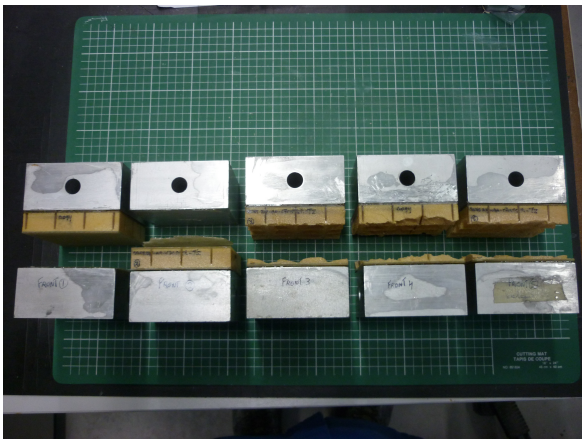

(a) FT specimens front view after test.

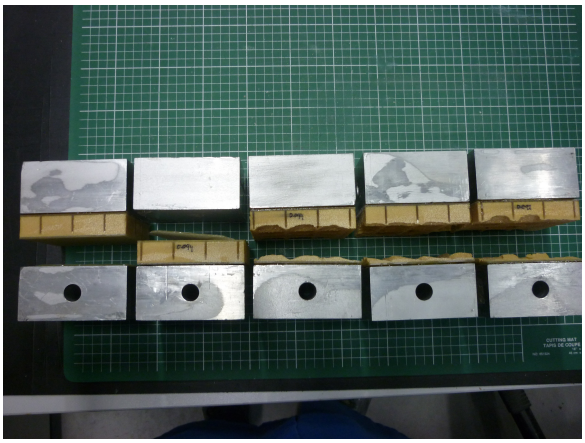

(b) FT specimens side view after test.

Figure 4.6: FT specimens after testing showing different damage modes.

Appendix A.1.3 with help of Figure A.8b.

Table 4.5: Resulting averaged data for FT tests. Units for stresses and moduli are [MPa] and units for strains are [%].

Sandwich Structure Benchmark, n=3	ε_{dmg} [%]	σ_{dmg} [MPa]	ε_{max} [%]	σ_{max} [MPa]	ε_{ult} [%]	σ_{ult} [MPa]	E [MPa]
Mean	2.88E+00	1.67E+00	3.09E+00	1.71E+00	3.45E+00	1.60E+00	6.43E+01
Standard Deviation	6.57E-01	9.94E-02	5.31E-01	4.55E-02	4.94E-01	1.42E-01	1.18E+01
Variance	4.31E-01	9.87E-03	2.82E-01	2.07E-03	2.44E-01	2.03E-02	1.39E+02

4.3.2. THREE POINT BENDING

The used test method is "ASTM C 393/C 393M - 06" or "Standard Test Method for Core Shear Properties of Sandwich Constructions by Beam Flexure"[76]. A schematic representation of the test setup is shown in Figure 4.8a. By applying this test method to coupon testing, the core shear properties can be obtained. The constituents used in the sandwich coupons are Advantex SE1500 tri-axial glass fibre mats, Airex C70.55CK PVC foam core and resin system Y. These materials are compliant for use with this test standard. For this test, six test specimens were tested. The design and actual (measured) coupon dimensions are given in Table 4.6, which are compliant for the test standard requirements.

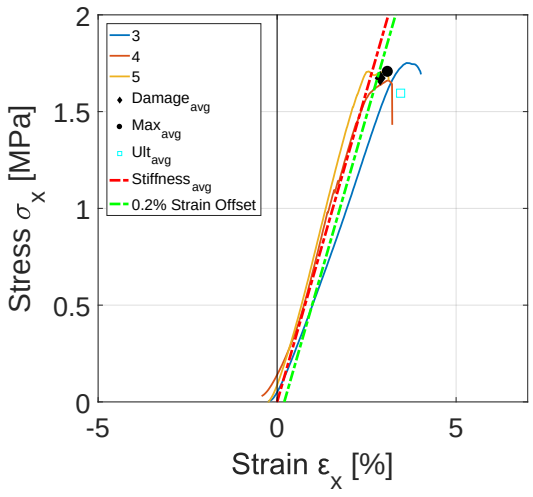

Figure 4.7: Stress-strain curves for FT sandwich specimens.

Table 4.6: TPB: Design and actual coupon dimensions. Average values based on 6 test coupons.

Dimension	Design Value	Measured Value
Width b [mm]	60	59.36
Length L [mm]	400	399.67
Sandwich thickness t_s [mm]	22	23.25
Core Thickness t_c [mm]	20	20.00

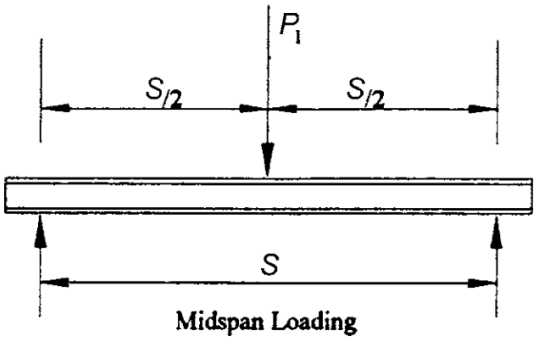

(a) TPB schematic representation [76].

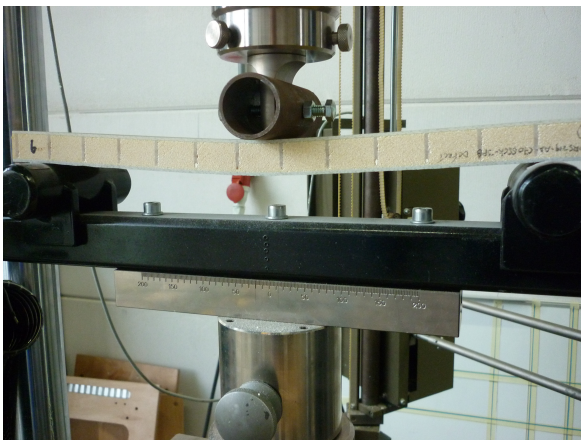

(b) TPB setup.

Figure 4.8: TPB schematic representation and test setup.

Figure 4.8b shows a specimen in the test setup during loading. Figures 4.9a and 4.9b show respectively scrim positioned up (SU) and scrim positioned down (SD) specimens from a front view after final loading. It can be seen that all specimens failed in core shear failure and thus in a mode accepted by the test standard.

Characterisation analysis on these test specimens will be done in a similar manner as before. The shear stress is acting on the full area of the core and can hence be computed using Equation 4.1. The displacement is measured and the flexural stress and strain can be calculated using Equations 4.2 and 4.3. The shear stress versus displacement ($\tau_{xy} - \delta_x$) curves for both SU and SD are shown in Figure 4.11, the flexural stress versus flexural strain ($\sigma_f - \epsilon_f$) curves for both SU and SD are shown in Figure 4.10 in which it can be seen that for these specimens the 0.2% strain offset does not make sens and should be taken a lot smaller to find the

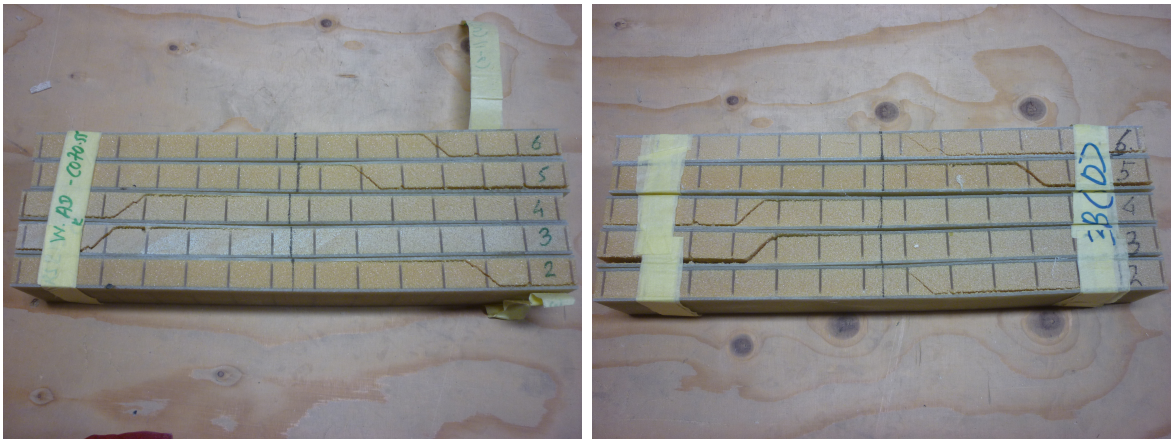

(a) TPB sandwich scrim up front view after test (b) TPB sandwich scrim down front view after test

Figure 4.9: TPB sandwich coupons after testing.

damage initiation point. The characterisation analysis of these results in terms of Young's moduli and damage/max/ult stresses are summarised in Tables 4.7 and 4.8.

$$\sigma = \frac{P}{(t_s + t_c) \cdot b} \tag{4.1}$$

$$\sigma_f = \frac{3 \cdot P \cdot S}{2 \cdot b \cdot t_s^2} \tag{4.2}$$

$$\epsilon_f = \frac{6 \cdot \delta \cdot t_s}{S^2} \tag{4.3}$$

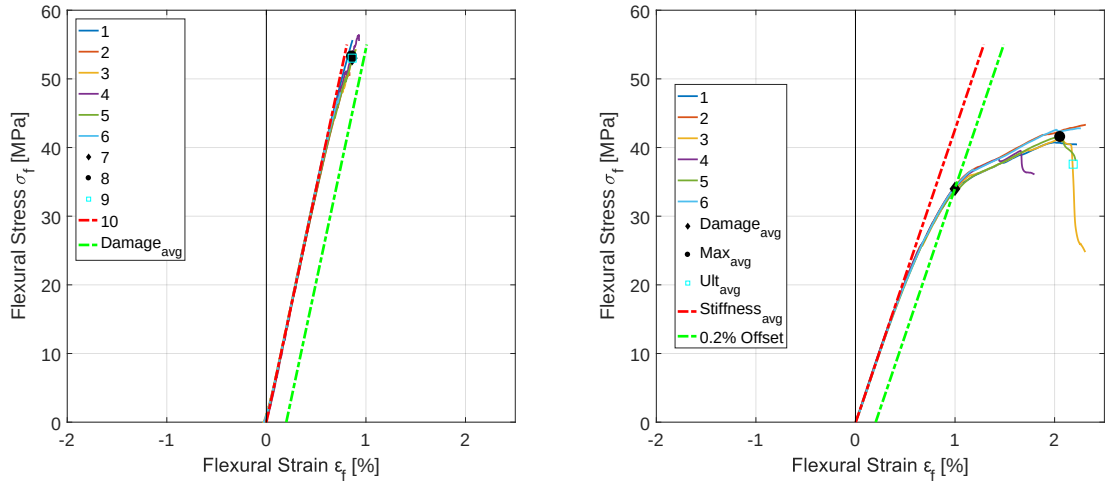

(a) TPB sandwich SU flexural stress-strain curve (b) TPB sandwich SD flexural stress-strain curve

Figure 4.10: Characterisation analysis of TPB test coupons - Flexural stress vs flexural strain

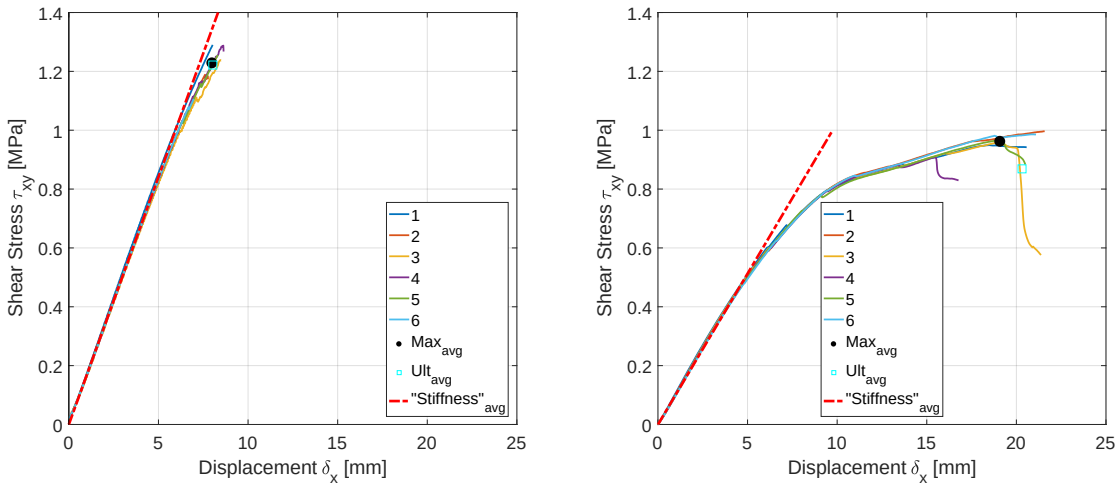

(a) TPB sandwich SU shear stress-displacement curve

(b) TPB sandwich SD shear stress-displacement curve

Figure 4.11: Characterisation analysis of TPB test coupons - Shear stress vs displacement.

Table 4.7: Averaged data from the three point bending SU flexural stress-strain graph. Units for stresses and moduli are [MPa] and units for strains are [%].

Sandwich Structure Benchmark SU, n=6	ε_{dmg} [%]	σ_{dmg} [MPa]	ε_{max} [%]	σ_{max} [MPa]	ε_{ult} [%]	σ_{ult} [MPa]	E [MPa]
Mean	-	-	8.58E-01	5.33E+01	8.62E-01	5.30E+01	6.80E+03
Standard Deviation	-	-	6.77E-02	3.14E+00	6.66E-02	3.08E+00	9.65E+01
Variance	-	-	4.59E-03	9.88E+00	4.44E-03	9.50E+00	9.31E+03

Table 4.8: Averaged data from the three point bending SD flexural stress-strain graph. Units for stresses and moduli are [MPa] and units for strains are [%].

Sandwich Structure Benchmark SD, n=6	ε_{dmg} [%]	σ_{dmg} [MPa]	ε_{max} [%]	σ_{max} [MPa]	ε_{ult} [%]	σ_{ult} [MPa]	E [MPa]
Mean	9.99E-01	3.40E+01	2.05E+00	4.16E+01	2.19E+00	3.76E+01	4.28E+03
Standard Deviation	1.32E-02	5.35E-01	2.28E-01	1.38E+00	1.95E-01	6.85E+00	3.82E+01
Variance	1.75E-04	2.86E-01	5.21E-02	1.91E+00	3.81E-02	4.69E+01	1.46E+03

Table 4.9: Averaged shear stress vs displacement data from all TPB Characterisation tests benchmark SU Sandwich Structure.

Sandwich Structure Benchmark SU, n=6	δ_{dmg} [mm]	τ_{dmg} [MPa]	δ_{max} [mm]	τ_{max} [MPa]	δ_{ult} [mm]	τ_{ult} [MPa]
Mean	-	-	8.00E+00	1.23E+00	8.03E+00	1.22E+00
Standard Deviation	-	-	6.21E-01	7.02E-02	6.09E-01	6.91E-02
Variance	-	-	3.85E-01	4.93E-03	3.71E-01	4.77E-03

Table 4.10: Averaged shear stress vs displacement data from all TPB Characterisation tests benchmark SU Sandwich Structure.

Sandwich Structure Benchmark SD, n=6	δ_{dmg} [mm]	τ_{dmg} [MPa]	δ_{max} [mm]	τ_{max} [MPa]	δ_{ult} [mm]	τ_{ult} [MPa]
Mean	5.59E+00	5.52E-01	1.91E+01	9.61E-01	2.03E+01	8.69E-01
Standard Deviation	5.79E-01	4.40E-02	2.13E+00	3.10E-02	1.79E+00	1.57E-01
Variance	3.35E-01	1.94E-03	4.54E+00	9.59E-04	3.20E+00	2.46E-02

5

EXPERIMENTAL RESULTS

In this chapter, the results of the resin link specimens are presented, discussed, and are compared to each other and to the benchmark grid-scored sandwich structure. The numerical results shown have been analysed following the same procedures as used in Chapter 4.

5.1. FLATWISE TENSION RESULTS

From inspection of the failed specimens, as can be seen in Figures 5.1 and 5.2, all of the sandwich specimens for both 3mm and 5mm resin links have failed at the scrim side. For the flatwise tensile tests, it does not matter whether the scrim is placed up or down in the test setup. Looking at the fractured specimens closely in Figures 5.3a, it can be seen that fracture goes through the resin links for the $3mm$ case. The resulting fracture surface takes the shape of a 'pillow' as can be seen in Figure 5.4, where the edges of the pillow are located directly underneath the resin bridges. Fracture thus occurs in the foam region directly under the resin bridge. This behaviour is very similar to the behaviour observed in the benchmark tests (see Figure 4.6).
For the $5mm$ case as seen more up close in Figure 5.3b, a similar fracture surface 'pillow'-trend as the $3mm$ case is observed, however while fracture still goes through the resin link, for the $5mm$ case it is in some specimens seen propagating through the resin bridge. This indicates that the $5mm$ resin links in some cases are large enough to act as a peel stopper[1]. Fracture through the resin bridge might occur when the bridge is not completely filled up with resin during infusion. Due to a larger $5mm$ resin link taking up more of the load, failure can now be seen to occur at less strong locations such as imperfect resin bridges.

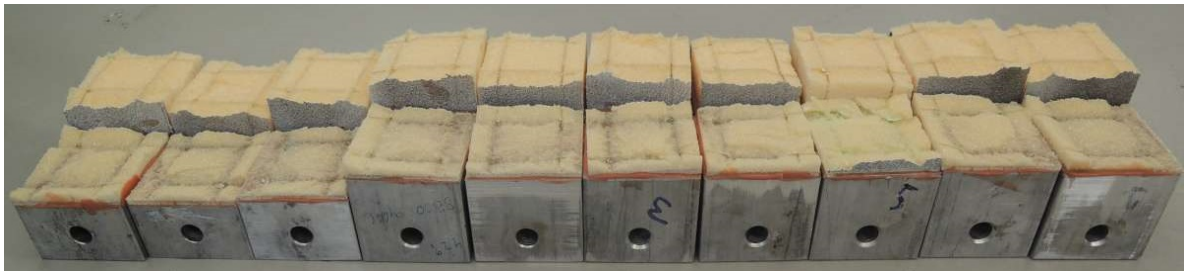

Figure 5.1: Flatwise tension specimens of sandwich structures with 3mm resin links after test.

For each test, the Zwick testing machine provides the applied force and displacement throughout the test. The characterisation of the tests will be analysed in the same fashion as they have been analysed in Section 4.3.1. The resulting stress vs strain graphs are shown in Figures 5.5b and 5.5c. It has to be noted that the stress indicated here is the average stress in the specimen. From the figures and from the result summary given in Tables 5.2 and 5.3 it can be seen that the standard deviation and variance for each of the tested specimen sets are small.Figure 5.5a shows the benchmark stress strain results for comparison.

[1] structure that (temporary) resists crack growth as discussed previously in Section 3.2.5.

Figure 5.2: Flatwise tension specimens of sandwich structures with 5mm resin links after test.

(a) Close-up of 3mm flatwise tension specimen.

(b) Close-up of 5mm flatwise tension specimen.

Figure 5.3: Close-up of flatwise tension specimens after test.

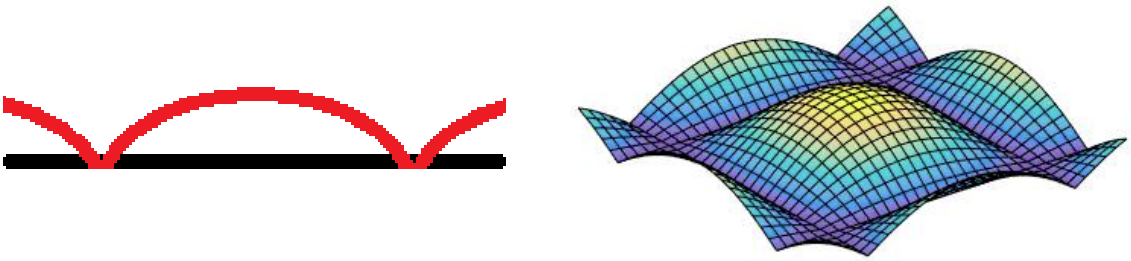

(a) 2D schematic of the 'pillow'.

(b) 3D Schematic of 'pillow'.

Figure 5.4: Schematics of the observed fracture shape of the FT tensile specimens.

When comparing the benchmark with resin links in both 3 and 5mm configuration, no noticeable trend can be discovered as can be seen in Figure 5.6. When considering only the 3 and 5mm resin links in the same figure, it can be stated that; The more resin is added, thus the larger the resin links are, the more the maximum strain increases, while the maximum stress and stiffness decreases.

Table 5.1: Resulting averaged data for FT benchmark tests. Units for stresses and moduli are [MPa] and units for strains are [%].

Sandwich Structure Benchmark, n=3	ε_{dmg} [%]	σ_{dmg} [MPa]	ε_{max} [%]	σ_{max} [MPa]	ε_{ult} [%]	σ_{ult} [MPa]	E [MPa]
Mean	2.88E+00	1.67E+00	3.09E+00	1.71E+00	3.45E+00	1.60E+00	6.43E+01
Standard Deviation	6.57E-01	9.94E-02	5.31E-01	4.55E-02	4.94E-01	1.42E-01	1.18E+01
Variance	4.31E-01	9.87E-03	2.82E-01	2.07E-03	2.44E-01	2.03E-02	1.39E+02

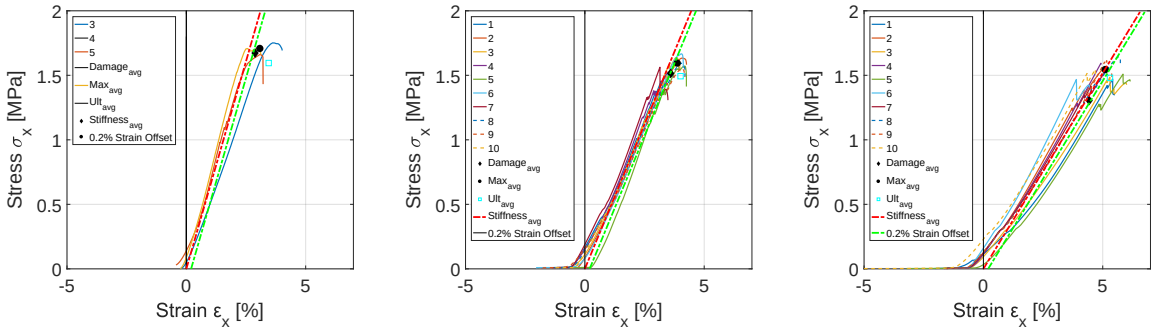

(a) Benchmark FT results. (b) 3mm resin links FT results. (c) 5mm resin links FT results.

Figure 5.5: Stress-strain graphs of benchmark, $3mm$ and $5mm$ resin link specimens for flatwise tension

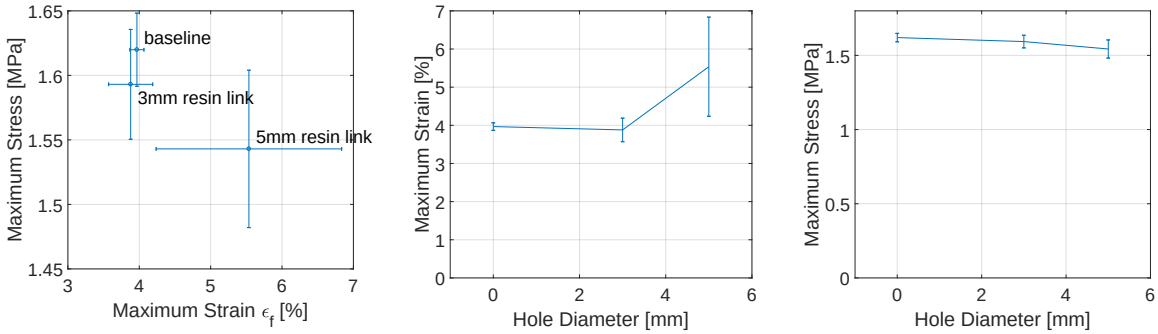

(a) Flatwise tensile trend in maximum flexural stress/strain. (b) Flatwise tensile trend in maximum flexural strain. (c) Flatwise tensile trend in maximum flexural stress.

Figure 5.6: Flatwise tensile trends of benchmark and $3mm$ & $5mm$ resin link cases.

Table 5.2: Averaged data from all flatwise tensile characterisation tests for resin link 3mm Sandwich Structure. Data for each specific specimen can be found in Table B.1 in Appendix B.1.

Sandwich Structure 3mm resin links, n=10	ε_{dmg} [%]	σ_{dmg} [MPa]	ε_{max} [%]	σ_{max} [MPa]	ε_{ult} [%]	σ_{ult} [MPa]	E [MPa]
Mean	3.59E+00	1.51E+00	3.88E+00	1.59E+00	4.01E+00	1.49E+00	4.48E+01
Standard Deviation	3.77E-01	1.09E-01	3.09E-01	4.26E-02	2.52E-01	8.11E-02	2.87E+00
Variance	1.42E-01	1.18E-02	9.53E-02	1.81E-03	6.37E-02	6.57E-03	8.24E+00

Table 5.3: Averaged data from all flatwise tensile characterisation tests for resin link 5mm Sandwich Structure. Data for each specific specimen can be found in Table B.2 in Appendix B.2.

Sandwich Structure 5mm resin links, n=10	ε_{dmg} [%]	σ_{dmg} [MPa]	ε_{max} [%]	σ_{max} [MPa]	ε_{ult} [%]	σ_{ult} [MPa]	E [MPa]
Mean	4.43E+00	1.30E+00	5.11E+00	1.54E+00	5.30E+00	1.48E+00	3.04E+01
Standard Deviation	1.14E+00	3.42E-01	5.47E-01	6.10E-02	5.54E-01	7.59E-02	4.62E+00
Variance	1.30E+00	1.17E-01	2.99E-01	3.72E-03	3.07E-01	5.76E-03	2.13E+01

Throughout the testing of every specimen, stereoscopic images are recorded with a frequency of $2Hz$. These images are analysed using the software package VIC-3D by Correlated Solutions. The flatwise specimens are analysed using the following settings; subset=81 and step=7. The standard subset is 29. A higher subset also induces a longer computation time. For these settings the computational time is about 45 minutes per specimen.

Since all flatwise tensile 3mm resin link specimens show a very similar pattern during loading, DIC images of only 1 specimen are shown in Figure 5.7. All other images and videos showing strain fields during the whole loading cycle can be found in the external Digital Appendix on the enclosed DVD. From the strain fields shown in Figure 5.7b, the position of the resin bridges can be clearly seen. At the resin bridges, the strain field is close to zero (purple in the figure). The strain field reaches maximal strain concentrations at the tips of the resin bridges in the scrim.
Since the DIC system made 2 images per second, it can be used to trace back crack initiation by starting from final failure and tracing the figures back in time to find at which point in time the crack has initiated on the observed side of the specimen. This way of finding crack initiation is not perfect, but due to the high resolution images, it can be determined well. Figure 5.7a shows the DIC ϵ_{yy} strain field of specimen FT^6_{3mm} at the point in time where a very small crack has initiated. It can be seen that the maximum ϵ_{yy} strain at this point in time is 0.0969066 which correlates very well with the maximum tensile strain of 9.8% found for the core material in Section 4.1. Between the (visible) crack initiation and final failure (Figure 5.7d), there are 6 seconds in which the crack grows and the maximum ϵ_{yy} strain indicated by the VIC-3D software keeps increasing up to a maximum value of 24.3% (Figure 5.7b). This observed strain increase is practically unfeasible for the core material and is thus an error occuring to the presence of the crack. Strain values measured by DIC software near a crack can thus be erroneous.
All of the 3mm and 5mm resin link specimens showed similar failure behaviour. They all failed at the scrim

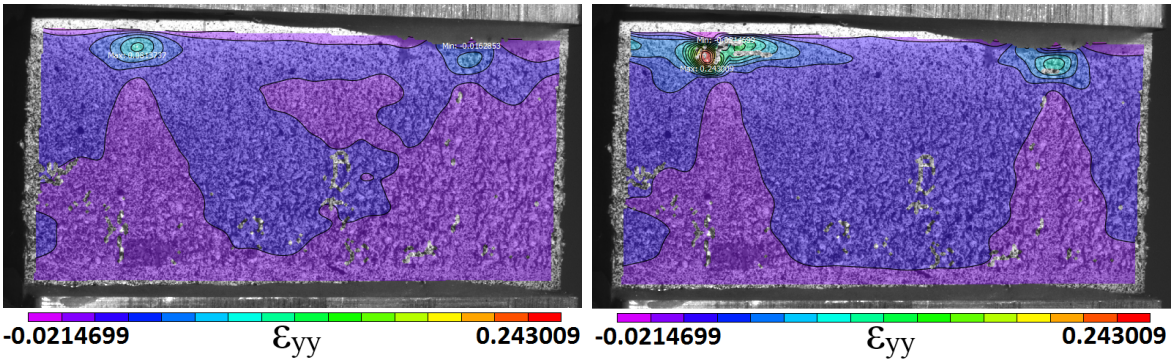

(a) DIC Image at crack initiation (top left).

(b) DIC Image immediately before final failure.

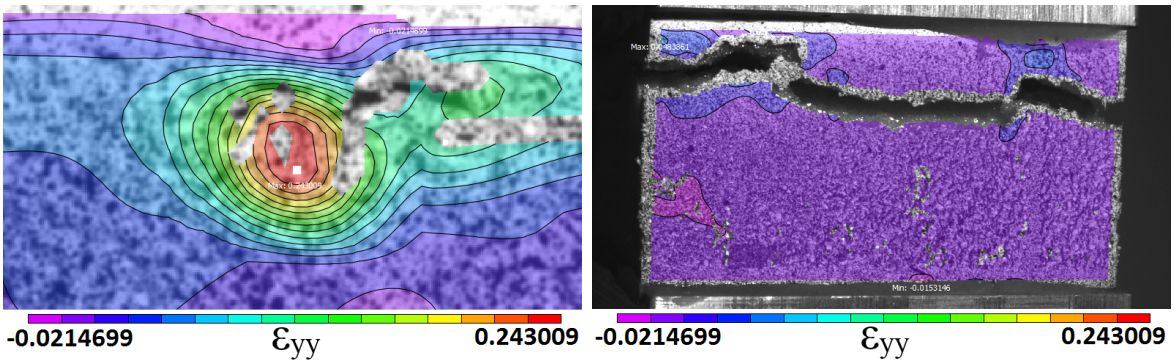

(c) Close-up of fig 5.7b showing large crack.

(d) DIC image at ultimate failure.

Figure 5.7: DIC images for the flatwise tensile test of the 3mm resin link specimens.

side of the specimen, and have all cracked through the resin links or exactly where the resin link and the resin bridge meet eachother. Crack propagation mostly goes through the scrim under the resin bridges, but in some $5mm$ cases, resin bridges get cracked. In some DIC videos, this crack is the first crack that shows up in the filmed side of the specimen.
The 3mm resin link specimen's maximum strain values at crack initiation at the crack position are given in Table 5.4. These values have been taken from DIC analysed measurements. Since the DIC only films 1 side of the specimen, and failure can initiate on a different side of, or also inside of the specimen, the strain values at failure can differ quite a bit. However, the strain fields observed by DIC all show the same lay-out as shown in Figure 5.7a. The specimens that have their initial failure close to the observed side of the specimen are FT^2_{3mm}, FT^4_{3mm}, FT^6_{3mm} and FT^8_{3mm}. These specimens display a crack initiation strain ϵ_{yy} close to the exper-

imentally determined tensile failure strain of 9.8% in Section 4.1.
Figure 5.7d shows specimen 6's strain field immediately after failure. It indicates that there might be plastic deformation remaining in the blue non-zero regions of the strain field.

Table 5.4: Table showing maximum strain values at the crack position at crack initation for the flatwise tensile test of 3mm resin link specimens.

Specimen ID	**Image Number**	ϵ_{yy}^{max} **At Crack Initiation** [%]
FT_{3mm}^{1}	1-0081	3.81
FT_{3mm}^{2}	2-0291	8.77
FT_{3mm}^{3}	3-0348	7.12
FT_{3mm}^{4}	4-0387	9.53
FT_{3mm}^{5}	5-0291	5.12
FT_{3mm}^{6}	6-0350	9.69
FT_{3mm}^{7}	7-0275	5.62
FT_{3mm}^{8}	8-0320	8.11
FT_{3mm}^{9}	9-0326	4.01
FT_{3mm}^{10}	10-306	7.52
	Mean	6.93
	Standard Deviation	2.18
	Variance	4.75

For the 5mm resin link case, some differences have been observed in comparison to the 3mm resin link case. Only one out of 10 of the $5mm$ specimens (FT_{5mm}^{2}) shows exactly the same behaviour as the 3mm resin link cases have shown.
Two out of the ten 5mm resin link specimens (FT_{5mm}^{5} and FT_{5mm}^{10}) show an almost uniform strain distribution through the thickness as can be seen in Figure 5.8a. This distribution only changes when crack initiation shows in the viewed surface to a distribution as shown in Figure 5.8b. This distribution resembles the case when the resin link carries all of the loading and the rest of the foam structure follows the same strain deformation as the resin (bridge+link). Maybe these two specimens have a larger hole diameter or were saw cut closer to the resin bridge parallel to the field of view. The remaining seven cases show similar behaviour

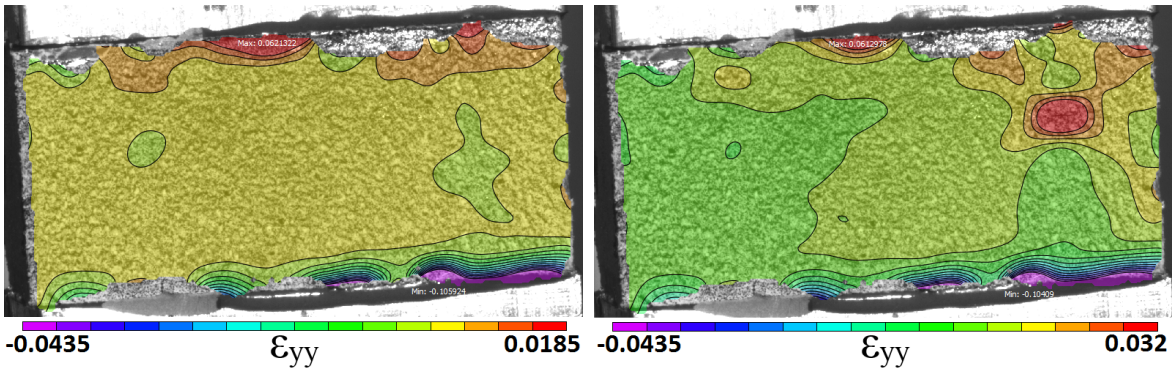

(a) FT_{5mm}^{10} before crack initiation.

(b) FT_{5mm}^{10} after crack initiation.

Figure 5.8: FT_{5mm}^{10} before (left) and after (right) crack initiation.

to each other, where before cracking the strain field looks like the one shown in Figure 5.9a. After cracking the strain field looks like the one shown in Figure 5.9b. This specific specimen shows 2 crack initiations, 1 in each resin bridge. Some other specimens only show 1 crack initiation on one of the 2 bridges, where the non-cracked resin bridge shows a more uniform strain distribution. From Figure 5.9a it can be seen that the strain

distribution over the resin bridge is no longer close to zero over the whole domain. After crack initiation, the strain in the resin bridges is reduced back to close to zero. This shows that the larger 5mm in stead of 3mm resin links take up a higher portion of the tensile loading, and that for the $5mm$ case the resin link carries the load together with the resin grid, hence the strain in the resin bridge tends more to uniformity. The resin grid will generally fail first, probably due to an (infusion) imperfection, after which the resin link will carry all of the loading and the resin bridge cannot anymore due to the crack, hence the strain in the resin bridge goes back to close to zero.

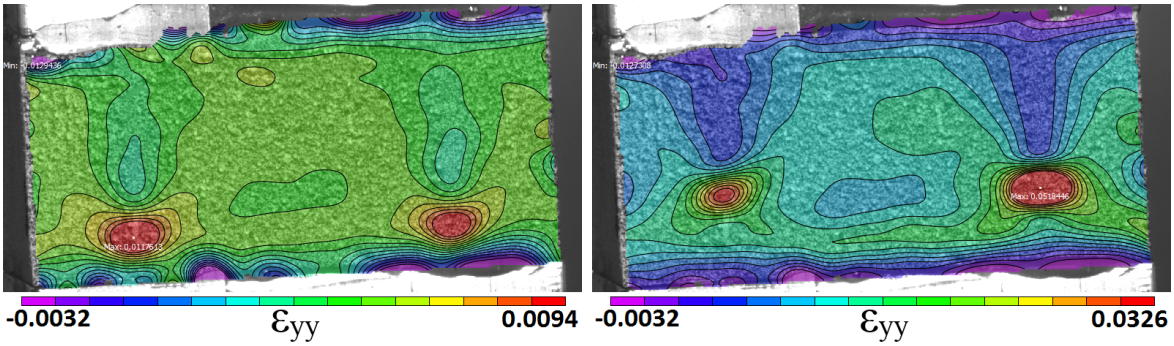

(a) FT^{3}_{5mm} before crack initiation.

(b) FT^{3}_{5mm} after crack initiation.

Figure 5.9: FT^{10}_{5mm} before (left) and after (right) crack initiation.

DISCUSSION OF RESULTS

The benchmark flatwise tension case only contained three usable specimens for further analysis. This is rather low to produce statistically significant results since the test standard recommends to have at least 5 usable specimens to analyse. However, they are the only test data available, hence they will be used with care. For both the 3mm, and 5mm resin link case, all flatwise tensile tests went well without any unexpected failures. All specimens showed a very uniform load-deflection behaviour with respect to each other, and by analysing this behaviour, the flatwise tension strength of the core has been determined with a low amount of scatter, indicating that the production of the test specimens, test setup, and testing itself has been performed well.

For the 3mm resin link case, the specimens all fail in the same manner, namely at the scrim side of the sandwich structure. This is the same behaviour as observed in the benchmark case. This kind of failure makes sense since this is the area of the sandwich structure where there is the least amount of resin present. The only resin present in the scrim side area is that of the resin links, which from post-failure inspection is seen to fracture through the resin link indicating that the resin link is too small to effectively change the failure mechanism for the sandwich structure loaded in flatwise tension.
From the DIC imagery, it has been shown that all the 3mm resin link specimens show the same behaviour, indicating that the same failure mechanism is at work for all those specimens. DIC shows fracture occurring in the foam material at values within a few percent to 9.8% strain as given as a tensile failure strain by the manufacturer. Initial fracture is observed to occur always in the foam areas in extension of the resin bridges, where from DIC measurements also strain concentrations occur as shown clearly in Figure 5.7b. This behaviour can be explained by the difference in stiffnesses between foam core material and resin material. Since the resin material has a much higher stiffness than the foam material, it pulls more of the load to itself. However, the resin bridge does not extend all the way throughout the thickness from facing to facing and at a certain point it has to transfer the load to either the foam or the resin link. This explains the observed occurrence of stress/strain concentrations at the ends of the resin bridges. One question now still remains in this failure mechanism, being “which element fails first?”. From DIC visualisation, cracks in the scrim foam region are observed multiple seconds before final failure, indicating that probably the foam fails first in the scrim region, after which the resin link carries the load until final failure occurs. However, to know for sure which element fails first, we have to be able to have a look inside the specimen, which is not possible with the DIC technique, but might be possible with an acoustic emission technique. Also, FE analysis might be a useful tool to be able to ‘look inside the structure’.

If there would be no resin bridges present in the sandwich structure, fracture would occur in the middle of the sandwich structure loaded in flatwise tension. Hence the 'pillow' fracture surface of the grid-scored structure with and without resin links can be explained, where at the resin bridge locations, fracture occurs at the scrim side, and far away from resin bridges fracture occurs more towards the middle of the sandwich structure. This leads to the 'pillow' shaped fracture surface as previously shown in Figure 5.4.

For the 5mm resin link case, almost all specimens fail in the same manner as the 3mm resin link case, however, some of the specimens show failure through the resin bridges. This might indicate that the resin link has reached or has almost reached a size for which the failure behaviour changes into a failure mode where the resin bridges fail before the resin link fails. However, it might also indicate that for these specimens, the resin has not completely filled up the grid and is thus failing here due to imperfections in the resin grid.
Even though at some locations the 5mm resin link specimens show fracture through resin bridges, the same general fracture surface 'pillow' trend has been observed as in the 3mm resin link specimens. For the 3mm resin link case, no fracture through resin bridges has been observed, from which the expectation can be made that for larger resin link diameters, this type of fracture might be observed more often, and the fracture mechanisms might change when going to these larger resin link sizes.
From DIC imagery, it has been shown that only one of the 5mm resin link specimens resembles exactly the same behaviour of the 3mm resin link case. This is probably due to an imperfection in this specimen. The other 5mm resin link specimens show a more uniform strain distribution through the thickness indicating that the resin link is carrying all of the loading, and the core can simply strain with the resin link, hence the uniform strain distribution in the observed plane. Crack initiation in these specimens has been observed to be occurring in a resin bridge. While this crack initiates, the rest of the investigated strain field keeps showing more or less a uniform strain distribution, indicating that the resin links are still intact and are still carrying all of the loading. This uniform strain distribution carries on until final failure.

Comparing the flatwise tensile strengths and strains of all three tests (benchmark, 3mm and 5mm resin links), showed no identifiable trend. When considering only the resin link 3mm and 5mm specimens, a small trend can be seen, namely; "The more resin is added, thus the larger the resin links are, the more the maximum strain increases, while the maximum stress and stiffness decreases." However, as can be judged from the trend graphs in Figure 5.6, this trend is very small and could very well simply be explained due to statistical scatter.

5.2. THREE POINT BENDING RESULTS

Figures 5.10, 5.11 and 5.12 show 30 specimens in total of which 10 benchmark specimens, 10 3mm resin link specimens and 10 5mm resin link specimens. Each of these sets of 10 have 5 scrim up and 5 scrim down oriented specimens. All of the 30 specimens show similar failure behaviour, namely shear failure. They all have a clearly identifiable 45° shear crack which propagates in 2 directions in a facing-peeling-manner. At the middle support, the shear force goes from maximum negative to maximum positive as can be seen in the shear diagram presented in Figure 5.13. This influences the peeling behaviour into a stop at the middle support of the TPB setup. The propagation lengths at both sides do not show a big difference, indicating that if the resin links have a peel-stopping effect (as would be expected from May-Pat et al.'s paper on Mechanical properties of sandwich panels with perforated foam cores [31]), it is only a small effect.
The position of the shear crack differs. For the benchmark specimens, the scatter of the shear crack position is large. For the 3mm resin link case in scrim up direction shown in Figure 5.11a, all specimens have failed at exactly the same location close to the outer support, however they don't seem to have been influenced by the supports since they haven't failed at exactly the support location. They all show a shear crack through the middle of a resin bridge. The 3mm resin link case in scrim down direction specimens all fail at approximately the same position, in between the middle and outer support. The same goes for the 5mm scrim up and scrim down specimens. None of the failures seem to have been influenced by the supports.

For each test, the Zwick testing machine provides the applied force and displacement throughout the test. A characterisation analysis of the tests will be analysed in the same fashion as they have been analysed in Section 4.3.2. The resulting stress vs strain graphs are shown in Figures 5.14c and 5.14d. It has to be noted that the flexural stresses and flexural strains indicated here are defined with Equations 4.2 and 4.3 as can be

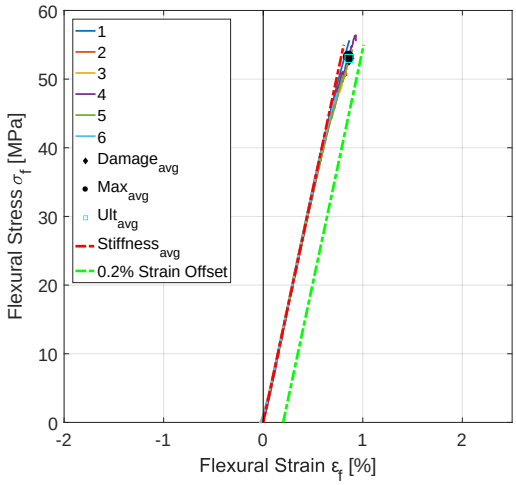

(a) Benchmark TPB Specimens 1-5, SU.

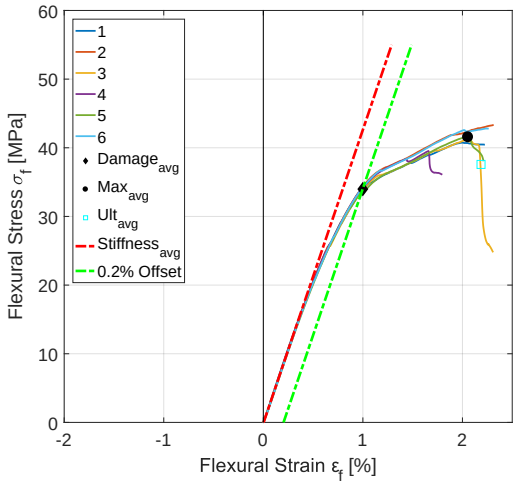

(b) Benchmark TPB Specimens 6-10, SD.

Figure 5.10: Three point bending specimens without resin links with either Scrim Up (SU) or Scrim Down (SD)

(a) 3mm TPB Specimens 1-5, SU.

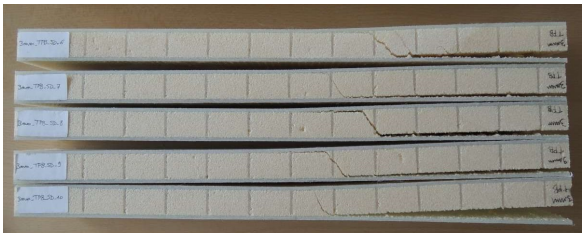

(b) 3mm TPB Specimens 6-10, SD.

Figure 5.11: Three point bending specimens numbers 1-10 with either Scrim Up (SU) or Scrim Down (SD).

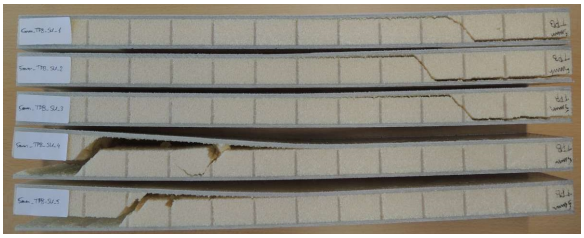

(a) 5mm TPB Specimens 1-5, SU.

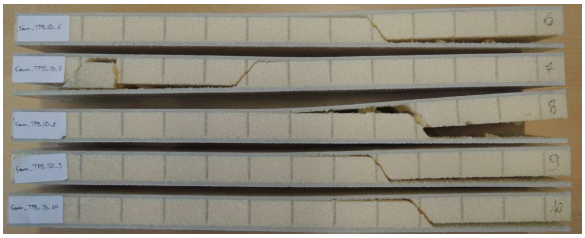

(b) 5mm TPB Specimens 6-10, SD.

Figure 5.12: Three point bending specimens numbers 1-10 with either Scrim Up (SU) or Scrim Down (SD).

found in Section 4.3.2. Also Figure 5.14a shows that the 0.2% strain offset does not make sense to find the damage initiation point and should be lowered to find the damage initiation point. The resulting shear stress vs displacement graphs are shown in Figures 5.15c and 5.15d. The shear stress is the stress acting on the full area of the core and can be computed using Equation 4.1 found in Section 4.3.2. From the figures and from the result summary given in Tables 5.6, 5.7 5.10 and 5.11 it can be seen that the standard deviation and variance for each of the tested specimen sets are small.

For 3mm, 5 scrim up and 5 scrim down specimens are plotted in Figure 5.14c. It can be seen that loading the specimens scrim up or scrim down does not show a difference. This is the same for the 5mm case. For the Benchmark case as shown in Figures 5.14a, 5.14b, 5.15a and 5.15b, loading the specimens in scrim up or scrim down shows a large difference. Hence indicating that the resin links lead to a more consistently performing structure. An increase in performance consistency is valuable to structural engineers who can use this to reduce safety factors needed in design.

While the benchmark scrim down placement shows little to no similarities with other three point bending

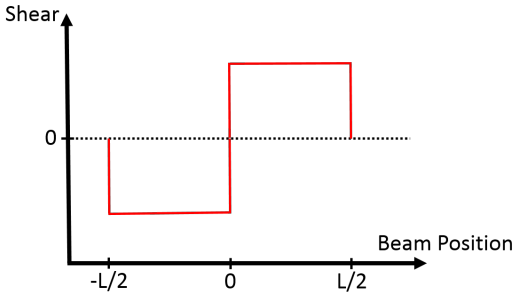

Figure 5.13: Three point bending shear diagram.

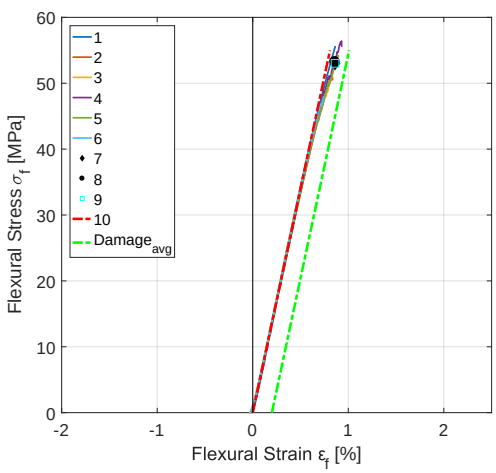

(a) Benchmark TPB Specimens 1-5, SU.

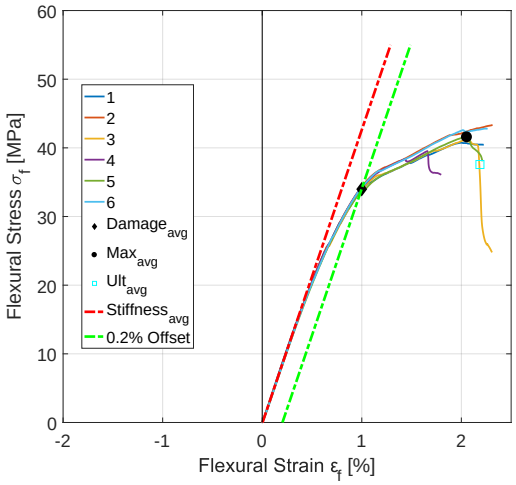

(b) Benchmark TPB Specimens 6-10, SD.

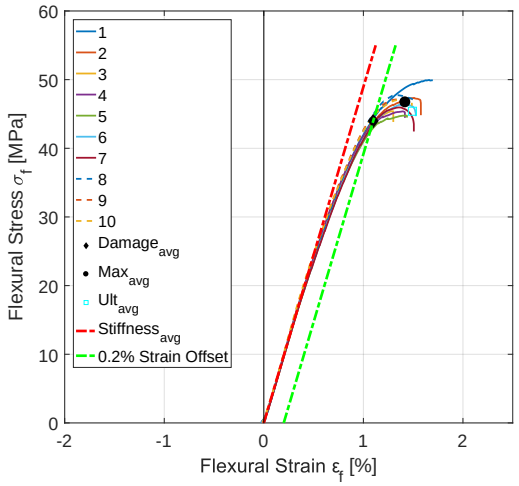

(c) 3mm TPB Specimens 1-10, SU & SD.

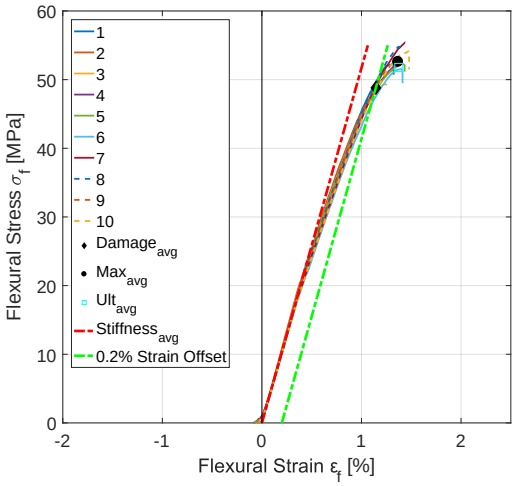

(d) 5mm TPB Specimens 1-10, SU & SD.

Figure 5.14: Stress-strain graphs for three point bending specimens for benchmark and $3mm$ and $5mm$ resin links.

tested specimens, the scrim up placement benchmark does show similarities with the $3mm$ and $5mm$ resin link cases. When comparing benchmark scrim up with resin links in both 3 and 5mm configuration, no identifiable trend can be found, as shown in Figure 5.16. When looking only at the resin link cases 3 and 5mm, it can be seen that the more resin is added, thus the larger the resin links are, the lower the flexural

stress and the higher the strain become. However the difference between the 3 and 5mm case is small.

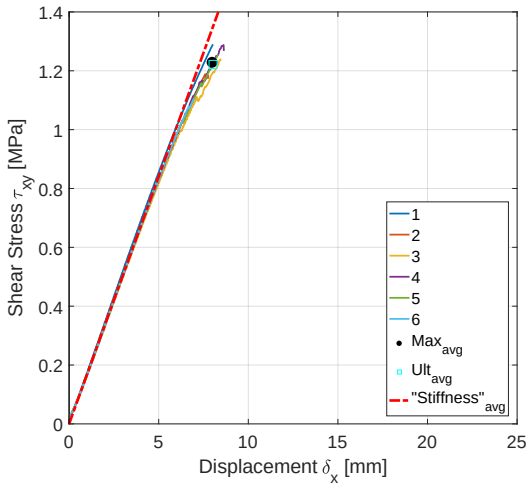

(a) Benchmark TPB Specimens 1-5, SU.

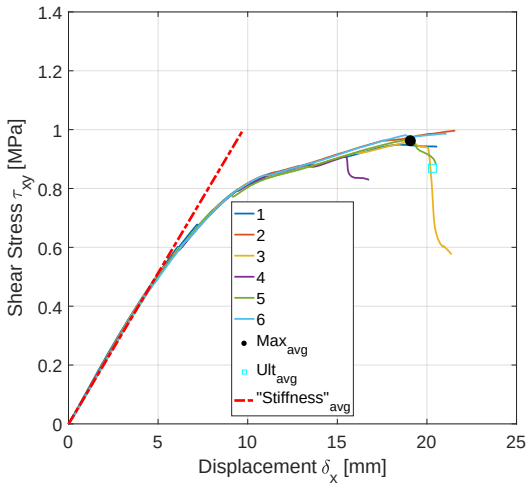

(b) Benchmark TPB Specimens 6-10, SD.

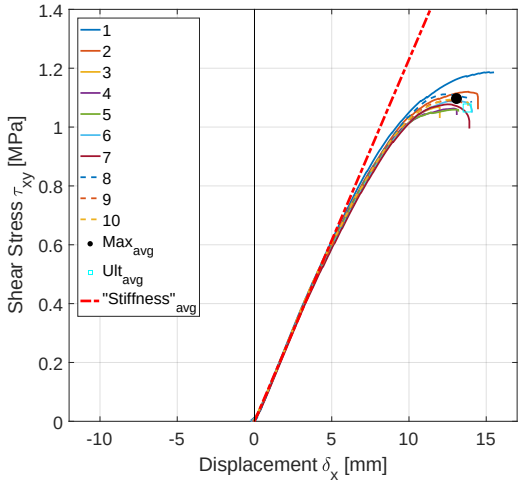

(c) 3mm TPB Specimens 1-10, SU & SD.

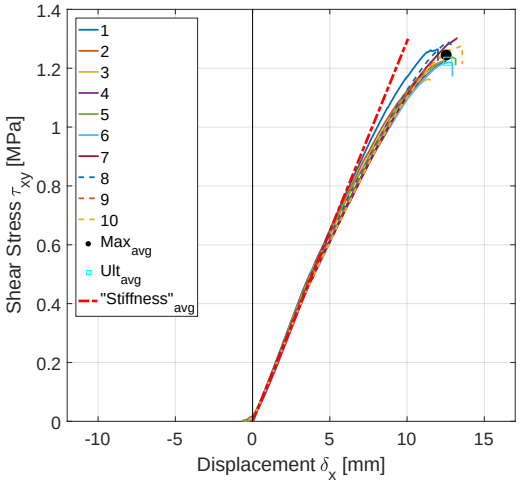

(d) 5mm TPB Specimens 1-10, SU & SD.

Figure 5.15: Shear stress-displacement graphs for three point bending specimens for benchmark and $3mm$ and $5mm$ resin links.

Table 5.5: Averaged data from the benchmark three point bending SU flexural stress-strain graph. Units for stresses and moduli are [MPa] and units for strains are [%].

Sandwich Structure Benchmark SU, n=6	ε_{f_dmg} [%]	σ_{f_dmg} [MPa]	ε_{f_max} [%]	σ_{f_max} [MPa]	ε_{f_ult} [%]	σ_{f_ult} [MPa]	E_f [MPa]
Mean	-	-	8.58E-01	5.33E+01	8.62E-01	5.30E+01	6.80E+03
Standard Deviation	-	-	6.77E-02	3.14E+00	6.66E-02	3.08E+00	9.65E+01
Variance	-	-	4.59E-03	9.88E+00	4.44E-03	9.50E+00	9.31E+03

Throughout the testing of every specimen, stereoscopic images are recorded with a frequency of $2Hz$. These images are analysed using the software package VIC-3D by Correlated Solutions. The three point bending specimens are analysed using the following settings; subset=55 and step=7. The standard subset is 29. A higher subset also induces a longer computation time. For these settings the computational time is about 45 minutes per specimen.

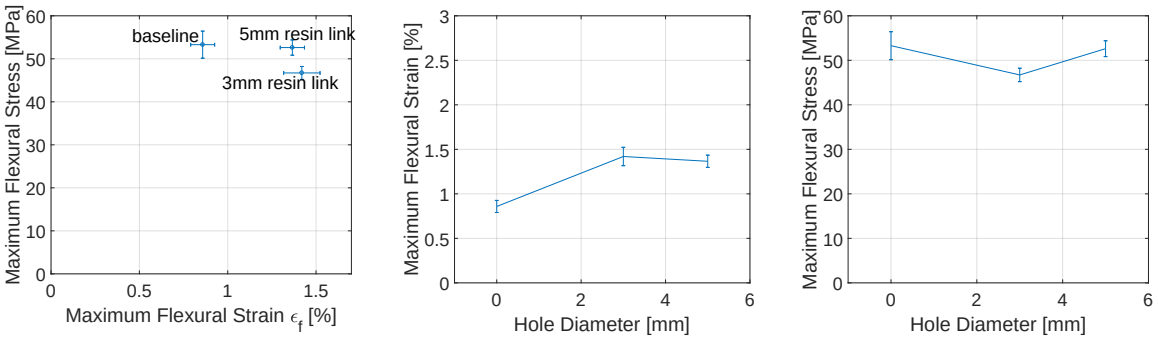

(a) TPB trend in maximum flexural stress/strain.

(b) TPB trend in maximum flexural strain.

(c) TPB trend in maximum flexural stress.

Figure 5.16: TPB trends of benchmark and $3mm$ & $5mm$ resin link cases.

Table 5.6: Averaged flexural stress-strain data from all TPB characterisation tests for resin link 3mm Sandwich Structure. Data for each specific specimen can be found in Table B.3 in Appendix B.3.

Sandwich Structure 3mm resin links, n=10	ε_{f_dmg} [%]	σ_{f_dmg} [MPa]	ε_{f_max} [%]	σ_{f_max} [MPa]	ε_{f_ult} [%]	σ_{f_ult} [MPa]	E_f [MPa]
Mean	1.10E+00	4.40E+01	1.42E+00	4.67E+01	1.49E+00	4.54E+01	4.89E+03
Standard Deviation	1.86E-02	7.86E-01	1.03E-01	1.50E+00	1.04E-01	2.04E+00	9.24E+01
Variance	3.44E-04	6.17E-01	1.06E-02	2.26E+00	1.09E-02	4.18E+00	8.54E+03

Table 5.7: Averaged flexural stress-strain data from all TPB characterisation tests for resin link 5mm Sandwich Structure. Data for each specific specimen can be found in Table B.5 in Appendix B.4.

Sandwich Structure 5mm resin links, n=10	ε_{f_dmg} [%]	σ_{f_dmg} [MPa]	ε_{f_max} [%]	σ_{f_max} [MPa]	ε_{f_ult} [%]	σ_{f_ult} [MPa]	E_f [MPa]
Mean	1.14E+00	4.88E+01	1.37E+00	5.26E+01	1.37E+00	5.18E+01	5.17E+03
Standard Deviation	4.06E-02	1.29E+00	6.85E-02	1.78E+00	6.85E-02	1.94E+00	1.24E+02
Variance	1.65E-03	1.65E+00	4.70E-03	3.17E+00	4.69E-03	3.75E+00	1.53E+04

Table 5.8: Averaged shear stress vs displacement data from all TPB characterisation tests benchmark Sandwich Structure.

Sandwich Structure Benchmark SU, n=6	δ_{dmg} [mm]	τ_{dmg} [MPa]	δ_{max} [mm]	τ_{max} [MPa]	δ_{ult} [mm]	τ_{ult} [MPa]
Mean	-	-	8.00E+00	1.23E+00	8.03E+00	1.22E+00
Standard Deviation	-	-	6.21E-01	7.02E-02	6.09E-01	6.91E-02
Variance	-	-	3.85E-01	4.93E-03	3.71E-01	4.77E-03

Table 5.9: Averaged shear stress vs displacement data from all TPB characterisation tests benchmark SU Sandwich Structure.

Sandwich Structure Benchmark SD, n=6	δ_{dmg} [mm]	τ_{dmg} [MPa]	δ_{max} [mm]	τ_{max} [MPa]	δ_{ult} [mm]	τ_{ult} [MPa]
Mean	5.59E+00	5.52E-01	1.91E+01	9.61E-01	2.03E+01	8.69E-01
Standard Deviation	5.79E-01	4.40E-02	2.13E+00	3.10E-02	1.79E+00	1.57E-01
Variance	3.35E-01	1.94E-03	4.54E+00	9.59E-04	3.20E+00	2.46E-02

Since all three point bending 3mm and 5mm resin link specimens show a very similar pattern during loading, only a few of the obtained DIC images are shown in Figure 5.17. For all other specimens, images and videos showing strain fields during the whole loading cycle can be found in the external Digital Appendix on the enclosed DVD.

Table 5.10: Averaged shear stress vs displacement data from all TPB characterisation tests for resin link 3mm Sandwich Structure. Data for each specific specimen can be found in Table B.4 in Appendix B.3.

Sandwich Structure 3mm resin links, n=10	δ_{dmg} [mm]	τ_{dmg} [MPa]	δ_{max} [mm]	τ_{max} [MPa]	δ_{ult} [mm]	τ_{ult} [MPa]
Mean	-	-	1.31E+01	1.10E+00	1.38E+01	1.06E+00
Standard Deviation	-	-	8.95E-01	3.76E-02	9.24E-01	4.97E-02
Variance	-	-	8.01E-01	1.41E-03	8.53E-01	2.47E-03

Table 5.11: Averaged shear stress vs displacement data from all TPB characterisation tests for resin link 5mm Sandwich Structure. Data for each specific specimen can be found in Table B.6 in Appendix B.4.

Sandwich Structure 5mm resin links, n=10	δ_{dmg} [mm]	τ_{dmg} [MPa]	δ_{max} [mm]	τ_{max} [MPa]	δ_{ult} [mm]	τ_{ult} [MPa]
Mean	-	-	1.26E+01	1.24E+00	1.26E+01	1.22E+00
Standard Deviation	-	-	6.32E-01	4.10E-02	6.30E-01	4.28E-02
Variance	-	-	3.99E-01	1.68E-03	3.97E-01	1.83E-03

From the shear strain fields as shown in Figure 5.17, the position of the resin bridges can be clearly seen. At

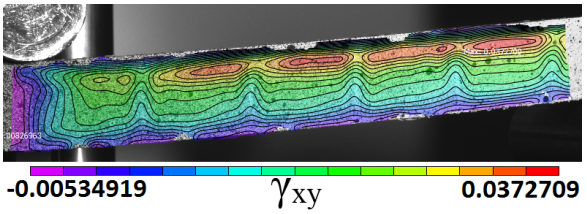

(a) DIC image for specimen $TPB_{3mm}^{SU_4}$ right before failure.

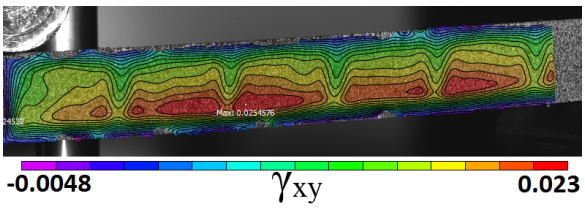

(b) DIC image for specimen $TPB_{3mm}^{SD_6}$ right before failure.

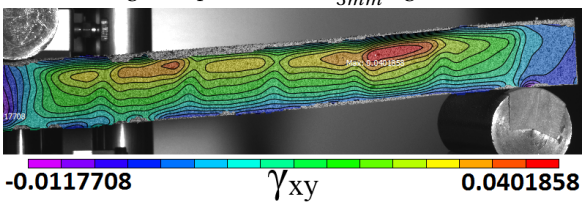

(c) DIC image for specimen $TPB_{5mm}^{SU_4}$ right before failure.

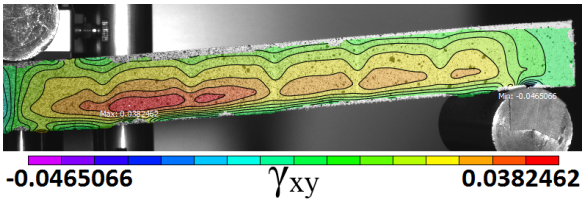

(d) DIC image for specimen $TPB_{5mm}^{SD_7}$ right before failure.

Figure 5.17: DIC Images for the TPB Test of the 3mm and 5mm resin link specimens. All images captured right before failure.

the resin bridges, the shear strain field is smaller than in the foam portions of the beam. The shear strain field reaches maximal shear strain concentrations between the tips of the resin bridges on the scrim side of the sandwich structure. It can be seen that shear strain concentrations are always on the scrim side of the sandwich structure, whether the sandwich is placed scrim up or scrim down in the test setup. The $5mm$ specimens in Figures 5.17c and 5.17d show a more concentrated shear strain than the $3mm$ specimens in Figures 5.17a and 5.17b, however, this is a false conclusion. After judging all $3mm$ and $5mm$ three point bending specimens, it shows that about half of the specimens show more concentrated shear strains, whereas the other half shows a more distributed shear strain over the scrim side. The cause for this might be found in changing the legend of the DIC images, or in the core material that shows imperfections in the specimens with a more concentrated shear strain.

The largest shear strains observed by DIC in the $3mm$ and $5mm$ three point bending specimens right before final failure occurs are given in Table 5.12 below. It can be seen that the scatter for these test results is fairly low, and that the scatter for the $5mm$ case is a bit higher than for the $3mm$ case. The shear stress at break is given by the manufacturer to be 4.0%, and thus the results shown in Table 5.12 are correlating well with the manufacturers data when taking into account 1 standard deviation.

Table 5.12: Table showing maximum strain values right before failure for the three point bending test of $3mm$ and $5mm$ resin link specimens.

Specimen ID	γ_{xy}^{max} [%]	**Specimen ID**	γ_{xy}^{max} [%]
$TPB_{3mm}^{SU\_1}$	5.16	$TPB_{5mm}^{SU\_1}$	2.83
$TPB_{3mm}^{SU\_2}$	4.83	$TPB_{5mm}^{SU\_2}$	3.79
$TPB_{3mm}^{SU\_3}$	3.26	$TPB_{5mm}^{SU\_3}$	2.62
$TPB_{3mm}^{SU\_4}$	3.73	$TPB_{5mm}^{SU\_4}$	4.02
$TPB_{3mm}^{SU\_5}$	5.42	$TPB_{5mm}^{SU\_5}$	5.31
$TPB_{3mm}^{SU\_6}$	4.18	$TPB_{5mm}^{SD\_6}$	3.67
$TPB_{3mm}^{SU\_7}$	3.97	$TPB_{5mm}^{SD\_7}$	3.82
$TPB_{3mm}^{SU\_8}$	4.84	$TPB_{5mm}^{SD\_8}$	3.51
$TPB_{3mm}^{SU\_9}$	5.07	$TPB_{5mm}^{SD\_9}$	3.14
$TPB_{3mm}^{SU\_10}$	4.94	$TPB_{5mm}^{SD\_10}$	4.21
Mean	4.54	Mean	3.69
Standard Deviation	0.71	Standard Deviation	0.76
Variance	0.50	Variance	0.58

DISCUSSION OF RESULTS

The benchmark three point bending case has been previously discussed in Section 4.3.2. Six specimens were tested and showed good correlation and low scatter with respect to eachother. For both the 3mm and 5mm resin link case, all three point bending tests went well without any unexpected failures. All specimens showed a very uniform load-deflection behaviour with respect to each other, and by analysis of the test data, the flexural strength of the sandwich has been determined with a low scatter, indicating that the production of the test specimens, test setup and testing itself has been performed well.
For all of the tests (benchmark + 3mm/5mm resin links), the failure mechanism observed is core shear failure, judging by the 45 degree fracture, which is the expected failure mode for doing the three point bending flexural test. Failure also occurred between the supports for every specimen and is thus deemed acceptable for the test standard. All 3mm and 5mm resin link specimens showed very sudden failure, where no crack initiation could be identified before final failure occured.

The benchmark test showed a very different behaviour for scrim up or down placement, namely for the scrim up it showed a brittle stress-strain curve, where for the scrim down placement the observed behaviour resembles a lot more ductile material. The cause of this is probably that for the scrim down placement, the scrim (foam core) material is loaded in tension and for the scrim up placement it is loaded in compression as is expected in beam bending. As can be found from the core characterisation in Chapter 4 and Appendix A, the foam's compressive strength and maximum strain is a lot higher than the core's tensile strength and maximum strain (respectively $1.8MPa$ and 77% versus $1.55MPa$ max stress and 9.8% max strain). The resin link 3mm and 5mm specimens showed no difference in load response whether they were placed scrim up or scrim down in the test setup. This indicates that the introduction of resin links changes the load path in the sandwich structure under three point bending. This is an important observation since for the resin link cases, the structure is performing very consistent whether loaded in scrim up or scrim down bending, whereas this is not at all the case for the benchmark.

From DIC imagery for both the 3mm and 5mm resin link case, it can be seen that all 3mm and 5mm specimens show very similar behaviour. Under three point bending loading, for both scrim up or down, the foam at the scrim side of the beam shows strain concentrations between the tips of the resin bridges. These strain concentrations are mostly uniform in size along the length of the beam as expected also from the shear diagram of a beam loaded in three point bending. From close inspection of the DIC images, it can be seen that the foam core material reaches a failure shear strain of 4.15% which is very close to the 4% as specified by the manufacturer. Differences can be due to a different batch of foam material tested.

Comparing the flexural strengths and strains of the three tests (benchmark, 3mm and 5mm resin links), showed no identifiable trend. When considering only the resin link 3mm and 5mm specimens, a small trend can be seen, namely; "The more resin is added, thus the larger the resin links are, the more the maximum strain increases, while the maximum stress and stiffness decreases." However, as can be judged from the trend graphs in Figure 5.16, this trend is very small and could very well simply be explained due to statistical scatter.

5.3. FOUR POINT BENDING RESULTS

For the four point bending test, no benchmark results are available. Figures 5.18a and 5.18b show 20 specimens in total of which 10 3mm resin link specimens and 10 5mm resin link specimens. Each of these sets of 10 have 5 scrim up and 5 scrim down oriented specimens. All of the 20 specimens show similar failure behaviour. They all have a clearly identifiable 45° shear crack[2] which propagates in 2 directions in a facing-peeling-manner.
In the center portion of the four point loaded beam, the shear forces are zero as shown in the shear diagram in Figure 5.19a.

The position of the shear crack is very consistent for each set of 5 specimens (3mm SU, 3mm SD, 5mm SU and 5mm SD) as can be seen in Figures 5.18a and 5.18b indicated with the red lines. It can also be seen that the remaining deformation after testing in the four point bending specimens is very small in comparison to the three point bending specimens, making it difficult to spot the cracks in the structure. It seems that there is more energy released during three point bending failure than during four point bending failure. This was also apparent from the louder failure noise that the three point bending specimens made in comparison to the four point bending specimens.

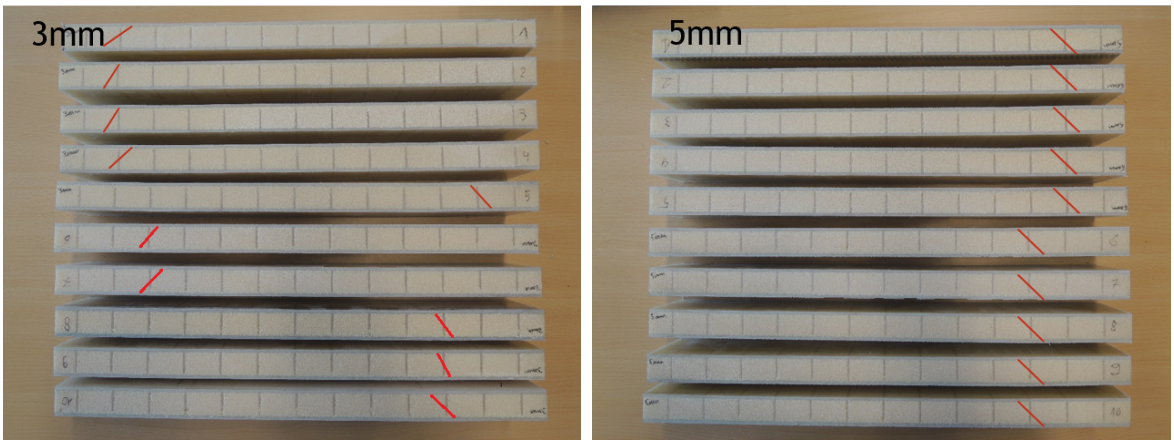

(a) TPB 3mm resin link specimens after failure.

(b) TPB 5mm resin link specimens after failure.

Figure 5.18: 4 Point bending specimens with resin links with either scrim up (SU) or scrim down (SD)

For each test, the Zwick testing machine provides the applied force and displacement throughout the test. Characterisation of the tests will be done using Equations 5.1 and 5.2.

$$\sigma_{flexural} = \frac{3 \cdot F \cdot L}{4 \cdot b \cdot d^2} \tag{5.1}$$

$$\epsilon_{flexural} = \frac{6 \cdot \delta \cdot t}{L^2}. \tag{5.2}$$

The resulting flexural stress-strain graphs are shown in Figures 5.20a and 5.20b. The resulting shear stress vs displacement graphs are shown in Figures 5.20c and 5.20d. From the figures and from the result summary given in Tables 5.13, 5.14, 5.15 and 5.16 it can be seen that the standard deviation and variance for each of the

[2] For the 3mm resin link sandwich structure loaded in four point bending, sometimes this is not a nice 45° angle.

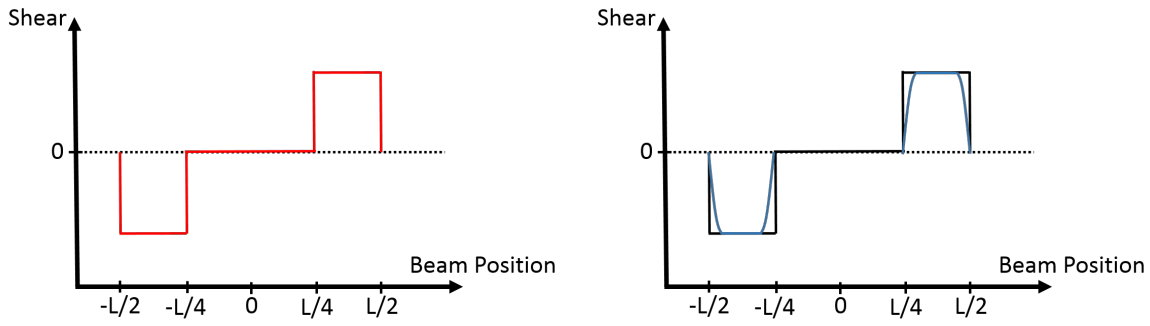

(a) FPB shear diagram.

(b) Observed FPB shear diagram.

Figure 5.19: 4 point bending shear diagrams.

tested specimen sets are small.
For 3mm, 5 scrim up and 5 scrim down specimens are plotted in Figure 5.20a. It can be seen that loading the specimens scrim up or scrim down does not show a difference. This is the same for the 5mm case.
When comparing resin link sandwich structures in 3mm and 5mm configuration to each other, it can be seen that while more resin is added (larger resin links), the maximum achievable stress decreases while the maximum achievable strain increases. This is made visual in Figure 5.21. However the difference between the 3 and 5mm case is small.

Table 5.13: Averaged flexural stress-strain data from all FPB characterisation tests for resin link 3mm Sandwich Structure. Data for each specific specimen can be found in Table B.7 in Appendix B.5.

Sandwich Structure 3mm resin links, n=10	ε_{f_dmg} [%]	σ_{f_dmg} [MPa]	ε_{f_max} [%]	σ_{f_max} [MPa]	ε_{f_ult} [%]	σ_{f_ult} [MPa]	E_f [MPa]
Mean	6.99E-01	2.32E+01	7.10E-01	2.34E+01	7.12E-01	2.33E+01	4.23E+03
Standard Deviation	3.52E-02	1.52E+00	6.55E-02	1.56E+00	6.56E-02	1.53E+00	1.88E+02
Variance	1.24E-03	2.32E+00	4.29E-03	2.43E+00	4.30E-03	2.35E+00	3.53E+04

Table 5.14: Averaged flexural stress-strain data from all FPB characterisation tests for resin link 3mm Sandwich Structure. Data for each specific specimen can be found in Table B.9 in Appendix B.6.

Sandwich Structure 5mm resin links, n=10	ε_{f_dmg} [%]	σ_{f_dmg} [MPa]	ε_{f_max} [%]	σ_{f_max} [MPa]	ε_{f_ult} [%]	σ_{f_ult} [MPa]	E_f [MPa]
Mean	-	-	6.66E-01	2.46E+01	6.69E-01	2.08E+01	4.27E+03
Standard Deviation	-	-	4.40E-02	8.74E-01	4.30E-02	1.87E+00	1.13E+02
Variance	-	-	1.94E-03	7.64E-01	1.85E-03	3.48E+00	1.29E+04

Table 5.15: Averaged shear stress-displacement data from all FPB characterisation tests for resin link 3mm Sandwich Structure. Data for each specific specimen can be found in Table B.8 in Appendix B.5.

Sandwich Structure 3mm resin links, n=10	δ_{dmg} [mm]	τ_{dmg} [MPa]	δ_{max} [mm]	τ_{max} [MPa]	δ_{ult} [mm]	τ_{ult} [MPa]
Mean	-	-	6.48E+00	1.23E+00	6.51E+00	1.03E+00
Standard Deviation	-	-	6.06E-01	7.74E-02	6.10E-01	1.50E-01
Variance	-	-	3.68E-01	6.00E-03	3.72E-01	2.24E-02

Throughout the testing of every specimen, stereoscopic images are recorded with a frequency of $2Hz$. These images are analysed using the software package VIC-3D by Correlated Solutions. The four point bend-

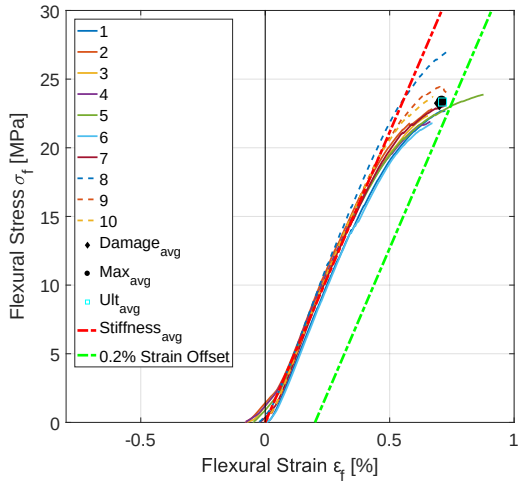

(a) 3mm TPB Specimens 1-10, SU & SD

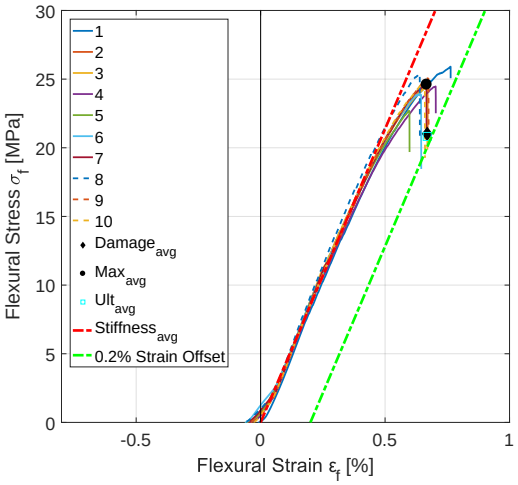

(b) 5mm TPB Specimens 1-10, SU & SD

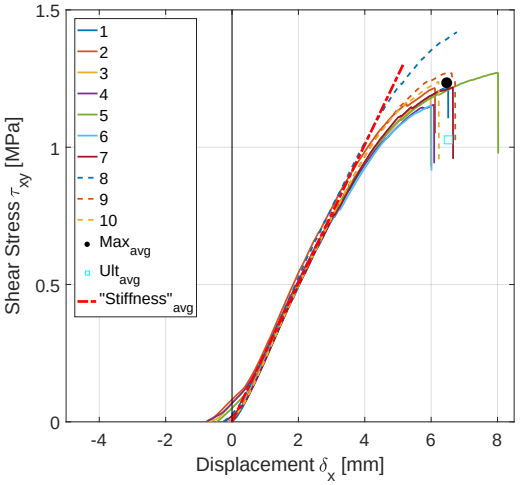

(c) 3mm TPB Specimens 1-10, SU & SD

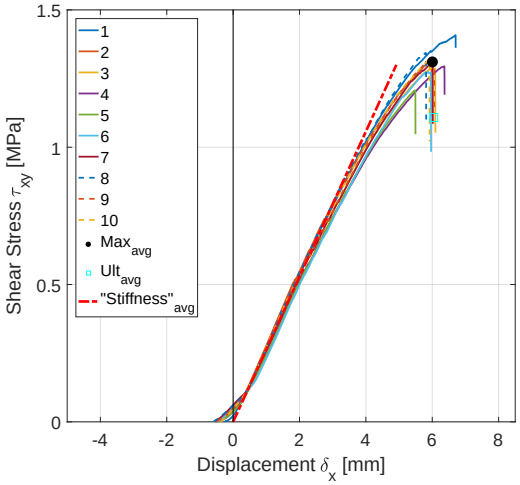

(d) 5mm TPB Specimens 1-10, SU & SD

Figure 5.20: 4 Point bending specimens for 3mm and 5mm resin links. Top 2 graphs show the flexural stress-strain and the bottom 2 graphs show the shear stress-displacement.

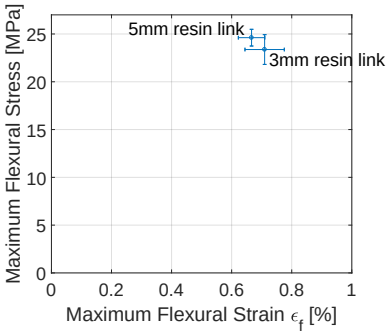

(a) FPB trend in maximum flexural stress/strain.

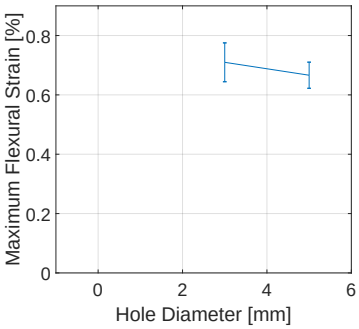

(b) FPB trend in maximum flexural strain.

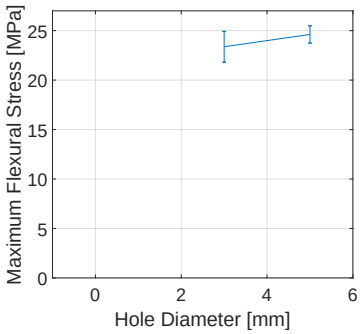

(c) FPB trend in maximum flexural stress.

Figure 5.21: FPB trends of benchmark and $3mm$ & $5mm$ resin link cases.

Table 5.16: Averaged shear stress-displacement data from all FPB characterisation tests for resin link 5mm Sandwich Structure. Data for each specific specimen can be found in Table B.10 in Appendix B.6.

Sandwich Structure 5mm resin links, n=10	δ_{dmg} [mm]	τ_{dmg} [MPa]	δ_{max} [mm]	τ_{max} [MPa]	δ_{ult} [mm]	τ_{ult} [MPa]
Mean	-	-	6.01E+00	1.31E+00	6.04E+00	1.11E+00
Standard Deviation	-	-	3.27E-01	5.14E-02	3.21E-01	1.07E-01
Variance	-	-	1.07E-01	2.64E-03	1.03E-01	1.13E-02

ing specimens are analysed using the following settings; subset=55 and step=7. The standard subset is 29. A higher subset also induces a longer computation time. For these settings the computational time is about 45 minutes per specimen.
Since all four point bending 3mm and 5mm resin link specimens show a very similar pattern during loading, only a few of the obtained DIC images are shown in Figure 5.22. For all other specimens, images and videos showing strain fields during the whole loading cycle can be found in the external Digital Appendix on the enclosed DVD.
From the shear strain fields as shown in Figure 5.17, the position of the resin bridges can be clearly seen. At

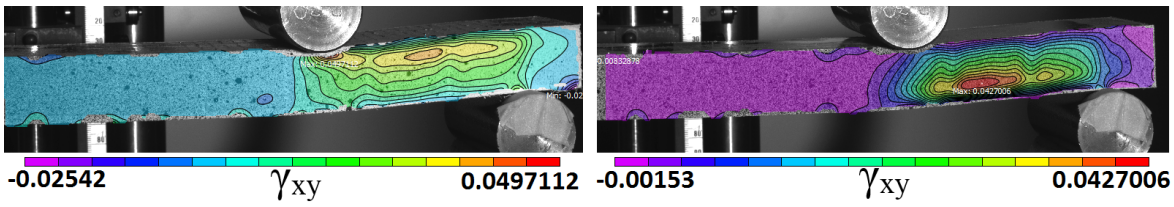

(a) DIC image of specimen $FPB_{3mm}^{SU\_3}$.

(b) DIC image of specimen $FPB_{3mm}^{SD\_6}$.

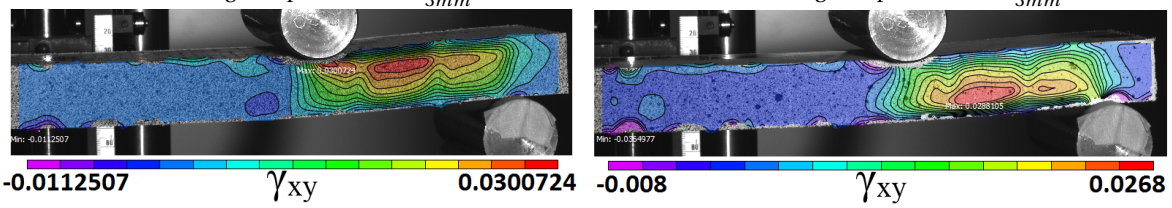

(c) DIC image of specimen $FPB_{5mm}^{SU\_4}$.

(d) DIC image of specimen $FPB_{5mm}^{SD\_8}$.

Figure 5.22: DIC Images for the FPB Test of the 3mm and 5mm resin link specimens. Images taken right before failure.

the resin bridges, the shear strain field reaches maximal shear strain concentrations between the tips of the resin bridges on the scrim side of the sandwich structure. It can be seen that shear strain concentrations are always on the scrim side of the sandwich structure, whether the sandwich is placed scrim up or scrim down in the test setup.
The $3mm$ specimens in Figures 5.22c and 5.22d show a more concentrated shear strain than the $3mm$ specimens in Figures 5.17a and 5.17b, however, this is a false conclusion. After judging all $3mm$ and $5mm$ four point bending specimens, it shows that about half of the specimens show more concentrated shear strains, whereas the other half shows a more distributed shear strain over the scrim side. The cause for this might be found in changing the legend of the DIC images, or in the core material that shows imperfections in the specimens with a more concentrated shear strain.
The largest shear strains observed by DIC in the $3mm$ and $5mm$ four point bending specimens right before final failure occurs are given in Table 5.17 below. It can be seen that the scatter for these test results is fairly low, and that the scatter for the $5mm$ case is a bit higher than for the $3mm$ case. The shear stress at break is given by the manufacturer to be 4.0%, and thus the results shown in Table 5.17 are correlating well with the manufacturers data when taking into account 1 standard deviation.

DISCUSSION OF RESULTS

For the four point bending test, no benchmark tests are available. For both the 3mm and 5mm resin link case, all four point bending tests went well without any unexpected failures. All specimens showed a very uniform

Table 5.17: Table showing maximum strain values right before failure for the four point bending test of $3mm$ and $5mm$ resin link specimens.

Specimen ID	γ_{xy}^{max} [%]	**Specimen ID**	γ_{xy}^{max} [%]
$FPB_{3mm}^{SU\_1}$	4.81	$FPB_{5mm}^{SD\_1}$	4.37
$FPB_{3mm}^{SU\_2}$	4.49	$FPB_{5mm}^{SD\_2}$	3.21
$FPB_{3mm}^{SU\_3}$	4.97	$FPB_{5mm}^{SD\_3}$	4.08
$FPB_{3mm}^{SU\_4}$	6.38	$FPB_{5mm}^{SD\_4}$	3.01
$FPB_{3mm}^{SU\_5}$	7.58	$FPB_{5mm}^{SD\_5}$	3.27
$FPB_{3mm}^{SU\_6}$	4.27	$FPB_{5mm}^{SU\_6}$	3.09
$FPB_{3mm}^{SU\_7}$	5.20	$FPB_{5mm}^{SU\_7}$	5.23
$FPB_{3mm}^{SU\_8}$	4.64	$FPB_{5mm}^{SU\_8}$	2.88
$FPB_{3mm}^{SU\_9}$	4.88	$FPB_{5mm}^{SU\_9}$	3.65
$FPB_{3mm}^{SU\_10}$	3.89	$FPB_{5mm}^{SU\_10}$	2.46
Mean	5.11	Mean	3.53
Standard Deviation	1.09	Standard Deviation	0.82
Variance	1.18	Variance	0.68

load-deflection behaviour with respect to each other, and by analysis of the test data, the flexural strength of the sandwich has been determined with a low scatter, indicating that the production of the test specimens, test setup and testing itself has been performed well.
For all of the tests (3mm/5mm resin links), the failure mechanism observed is core shear failure, judging by the 45 degree fracture, which is the expected failure mode for doing the four point bending flexural test. Failure also occurred between the supports for every specimen and is thus deemed acceptable for the test standard. All 3mm and 5mm resin link specimens showed very sudden failure, where no crack initiation could be identified before final failure occurred.

Although there is no benchmark test available for the four point bending, it is expected that in analogy with the three point bending loading, the benchmark test would have produced very different results whether loaded in scrim up or scrim down placement. This because the loading and the failure mode observed for the four point bending case is similar to the three point bending case.

From DIC imagery for both the 3mm and 5mm resin link case, it can be seen that all 3mm and 5mm specimens show very similar behaviour. Under four point bending loading, for both scrim up or down, the foam at the scrim side of the beam shows strain concentrations between the tips of the resin bridges. These strain concentrations are mostly uniform in size along the length of the part of the beam loaded in shear as expected from the shear diagram of a beam loaded in four point bending. From close inspection of the DIC images, it can be seen that the foam core material reaches a failure shear strain of 4.32% which is very close to the 4% as specified by the manufacturer. Differences can be due to a different batch of foam material tested.

Comparing the flexural strengths and strains of the two resin link cases (3mm and 5mm), a small trend can be seen, namely; "The more resin is added, thus the larger the resin links are, the more the maximum strain increases, while the maximum stress and stiffness decreases." This is the same conclusion as can be drawn from the three point bending test. However, as can be judged from the trend graphs in Figure 5.21, this trend is very small and could very well simply be explained due to statistical scatter.

From the above discussion, it can be seen that the three and four point bending results are very similar except for the value of the flexural strength and strain, which makes sense since these are dependent on the length of the beam between the supports. The DIC imagery shows very similar results and also very similar shear strains at failure close to those predicted by the manufacturer.

6

CONCLUSIONS & RECOMMENDATIONS

6.1. CONCLUSIONS

Research has been conducted into the effect of resin links on the critical loading capabilities of grid-scored sandwich structures applied in wind turbine blades. "Resin links" is a concept proposed by Suzlon Blade Technology, which is described as a perforation through the core material of a sandwich composite, whereby the two facings are linked together by resin. It has been hypothesized that resin links will increase the flexural modulus, shear modulus, and the failure strength of the sandwich structure while descreasing its maximum (shear) strain. The critical loading for sandwich structures in wind turbine applications is a shear and a bending loading. To test the hypothesis, several experiments have been conducted, namely flatwise tensile, three point bending and four point bending tests. All coupon testing went well and in general all of the results show little scatter. No results had to be disregarded in computations or comparisons. The same can be said for all of the DIC image capturing.

From the **flatwise tensile** tests it can be concluded that there is no trend visible for varying resin link diameters for the maximal tensile strength and strain. When considering only the $3mm$ and $5mm$ cases, it can be stated that; *"The more resin is added, thus the larger the resin links are, the more the maximum strain increases, while the maximum stress and stiffness decreases."*. This observation is in direct contradiction with the posed hypothesis. However the trend is small and when taking into account the standard deviation it could be argued that there is no trend to be found at all.
All $3mm$ and $5mm$ specimens failed through the resin links. However, the failure mechanism in the $5mm$ resin link case changed more towards resin bridge failure while for the $3mm$ case all failure went through the foam at the scrim part of the sandwich structure. The benchmark case showed exactly the same failure behaviour as the $3mm$ resin link case.
All obtained DIC results for the $3mm$ resin link case showed similar behaviour in contrast to the $5mm$ resin link case. The $5mm$ resin link case had a larger effect on the load path redistribution and take up more of the load than the $3mm$ resin links.

All of the **three point bending specimens** (benchmark, $3mm$ and $5mm$ resin links) showed shear failure. Mostly, this failure propagated through a resin bridge, and the resin links showed no noticeable effect of some sort of peel stopper mechanism. Shear strain concentrations in the foam were always found on the scrim side of the sandwich structure.
When comparing resin link cases $3mm$ and $5mm$, it can be seen that; *"The more resin is added, thus the larger the resin links are, the lower the flexural stress and stiffness, and the higher the flexural strain becomes"*. This observation is in direct contradiction with the posed hypothesis. However the difference between the 3 and 5mm case is small.
For the three point bending resin link cases,no difference in failure was observed whether the specimens are mounted in the test setup with scrim up or down. This is contrasting with the benchmark data where there is a large difference in behaviour between scrim up or down placement. *Hence indicating that the resin links lead to a more consistently performing structure.* An increase in performance consistency is valuable to structural engineers who can use this to reduce safety factors needed in design.

For the three point bending tests, the shear strain found by DIC correlates well with the shear strain given by the manufacturer when taking into account at maximum 1 standard deviation. However when comparing $3mm$ to $5mm$ resin link cases, it can be seen that all $3mm$ cases have a higher mean shear failure stress than the $5mm$ case.

Overall, the conclusions for the **four point bending** tests are the same as for the three point bending tests. No benchmark tests were available for the four poing bending case. All of the four point bending test specimens showed shear failure in one of the 2 outer regions of the test. Mostly, this failure propagated through a resin bridge, and the resin links showed no noticeable effect of some sort of peel stopper mechanism. Shear strain concentrations in the foam were always found on the scrim side of the sandwich structure.
Similar to the three point bending tests, it can be concluded when comparing resin link cases $3mm$ and $5mm$, that; *The more resin is added, thus the larger the resin links are, the lower the flexural stress and stiffness, and the higher the flexural strain becomes.* This observation is in direct contradiction with the posed hypothesis. However the difference between the $3mm$ and $5mm$ case is again small.
For the four point bending tests, no benchmark test results are available, so no comparison can be made. However, a similar behaviour is expected since the resin link four point bending specimens also failed in a shear regime.
For the four point bending tests, the shear strain found by DIC correlates well with the shear strain given by the manufacturer when taking into account at maximum 1 standard deviation. However, when comparing $3mm$ to $5mm$ resin link cases, it can be seen that all $3mm$ cases have a higher mean shear failure stress than the $5mm$ case.

6.2. RECOMMENDATIONS

Recommendations for further research or repeated research on the topic of resin links for grid-scored sandwich structures can be divided into four main categories shown in the summation below;

1. A Finite Element (FE) analysis should be made and compared to the results in this thesis.
    - From DIC imaging in this thesis, it is shown for which values of stress and strain failure occurs. If this can be correctly predicted by use of FE software, then FE modeling can be used to further investigate the effect of different types and parameters of resin links.
2. In order to investigate further what the effects are of implementing resin links to a sandwich structure, more tests should be performed.
    - The trends observed now consist of only 3 data points (benchmark, $3mm$, $5mm$). Hence more different resin link sizes should to be tested in order to obtain a trendline from more data points. For flatwise tensile; does the observed trend continue? For three and four point bending; do more resin link sizes indicate a trend? Does the trendline have a linear or an exponential tendency?
    - Comparing DIC results for flatwise tension load cases of $3mm$ and $5mm$ resin links showed that the DIC strain field behaviour was on the verge of changing in the $5mm$ resin link case. Testing a larger ($6mm$ or preferably $7mm$) resin link might show a full transition to a different more uniform strain field.
    - The three point bending tests for the benchmark structure without resin links should be redone. These show a large difference between scrim placement up and down. There is a small chance that this might be due to manufacturing differences. Also a four point benchmark test should be performed in scrim up and down placement to see if the same difference in scrim up and down placement can be observed here.
    - The "straight hole" resin links do not seem to have an effect on the shear properties of the structure, however other resin link types might have an effect. It is recommended to investigate other resin link concepts by either coupon testing or FE modeling (or a combination of both).
    - The statistical significance can be improved by performing more tests on the already tested $3mm$ and $5mm$ resin link cases. However, the scatter at this point is fairly low and more testing does not seem necessary.

- Other test types such as edgewise tension and compression should be performed to check the sandwich structure's performance to these tests.

3. While a small section of a sandwich panel in a large wind turbine blade can be considered flat/straight, it is probably wise to also perform testing on single or even double curved sandwich panels to find out what the effects of resin links are.

4. Laustsen at al. proposed a failure criterion for (normal) grid-scored sandwich structures. It can be recommended to see how appropriate it is to implement this criterion for the failure of grid-scored sandwich structures incorporating resin links.

BIBLIOGRAPHY

[1] Gurit, *Wind Energy: Market Information*, Tech. Rep. (Gurit, 2009).

[2] P. Joosse, *TUDelft*, Tech. Rep. March (TUDelft, Delft, 2013).

[3] B. B. Mary Harris,Sandy Van Natta,Marie Sherman, *41516 Anisotropy and fiber composites,* DTU Lecture Course 41516 , 6 (2011).

[4] I. M. Daniel and E. E. Gdoutos, *Failure Modes of Composite Sandwich Beams,* Major Accomplishments in Composite Materials and Sandwich Structures **11**, 197 (2010).

[5] A. C. Manalo, T. Aravinthan, W. Karunasena, and M. M. Islam, *Flexural behaviour of structural fibre composite sandwich beams in flatwise and edgewise positions,* Composite Structures **92**, 984 (2010).

[6] F. Aymerich, *Composite materials for wind turbine blades : issues and challenges*, Tech. Rep. July (University of Patras, 2012).

[7] C. Kassapoglou, *Thomas Telford, Polymers and Polymer Composites in . . .* (John Wiley & Sons, Ltd, 2010) p. 300.

[8] J.-M. Berthelot, *Non-linear Behaviour of Foam Cores and Sandwich Materials, Part 1: Materials and Modelling,* Journal of Sandwich Structures and Materials **4**, 219 (2002).

[9] 3A Composites, *Airex ® C70 Data Sheet,* Material Technical Data Sheet **1**, 1 (2011).

[10] O. T. Thomsen, *Sandwich Materials for Wind Turbine Blades - Present and Future,* Journal of Sandwich Structures and Materials **11**, 7 (2009).

[11] S. Trofka, *Effects of Contour Cuts on Shear Properties of Ductile Foam Cores,* Composites & Polycon 2007, American Composites Manufacturers Association, October 17-19, 2007, Tampla, FL USA **2**, 1 (2007).

[12] S. Laustsen, E. Lund, O. T. Thomsen, S. B. T. B. V, and H. Campus, *Experimental Characterisation of the Progresive Failure of Grid-Scored Sandwich Structures in Wind Turbine Blades,* in *Proceedings of the 19th international conference on composite materials (ICCM-19)* (2013) pp. 3344–3349.

[13] S. Laustsen, O. T. Thomsen, and E. Lund, *Analysis of Grid-Scored Sandwich Structures of Different Curvatures and Grid Sizes for Wind Turbine,* in *ECCM15 - 15TH EUROPEAN CONFERENCE ON COMPOSITE MATERIALS*, June (2012) pp. 24–28.

[14] S. Laustsen, E. Lund, L. Kuhlmeier, and O. Thomsen, *Failure behaviour of grid-scored foam cored composite sandwich panels for wind turbine blades subjected to realistic multiaxial loading conditions,* Journal of Sandwich Structures and Materials **16**, 481 (2014).

[15] a. Fathi, F. Wolff-Fabris, V. Altstadt, and R. Gatzi, *An investigation on the flexural properties of balsa and polymer foam core sandwich structures: Influence of core type and contour finishing options,* Journal of Sandwich Structures and Materials **15**, 487 (2013).

[16] A. Fathi, J.-H. Keller, and V. Altstaedt, *Full-field shear analyses of sandwich core materials using Digital Image Correlation (DIC),* Composites Part B: Engineering **70**, 156 (2015).

[17] O. T. Thomsen and J. Larsen, *Simplified Rule of Mixtures Approach for the Accurate Estimation of the Elastic Properties of Grid-Scored Polymer Foam Core Sandwich Plates,* 8th International Conference on Sandwich Structures , 261 (2008).

[18] J. Jakobsen, J. H. Andreasen, and O. T. Thomsen, *Crack deflection by core junctions in sandwich structures,* Engineering Fracture Mechanics **76**, 2135 (2009).

[19] D. T. Griffith, *An update on the Sandia 100-meter Blade Project,* (2014).

[20] J. Zhao, P. Chen, and H. Gregersen, *Stress-strain analysis of contractility in the ileum in response to flow and ramp distension in streptozotocin-induced diabetic rats-Association with advanced glycation end product formation,* Journal of Biomechanics **48**, 1075 (2015).

[21] Correlated Solutions, *Correlatedsolutions.com - Calibration,* (2017).

[22] WyomingTestFixtures, *SANDWICH PANEL FLATWISE TENSILE TEST,* (2017).

[23] J. F. Manwell, J. G. McGowan, and A. L. Rogers, *Wind Energy Explained* (Wiley, 2002) pp. vii, 577 p., arXiv:arXiv:1011.1669v3 .

[24] H. P. Konka, M. A. Wahab, and K. Lian, *On Mechanical Properties of Composite Sandwich Structures With Embedded Piezoelectric Fiber Composite Sensors,* Journal of Engineering Materials and Technology **134**, 011010 (2012).

[25] J. Doe, *Materials Eng Cam - Young's Modulus - Density,* (2001).

[26] J. Doe, *PVC sheets for composite structures,* (2017).

[27] A. B. Morgan and E. Toubia, *Cone calorimeter and room corner fire testing of balsa wood core/phenolic composite skin sandwich panels,* Journal of Fire Sciences **32**, 328 (2014).

[28] Easycomposites, *easycomposites.co.uk,* (2015).

[29] A. Kennedy, *Porous Metals and Metal Foams Made from Powders,* in *Powder Metallurgy* (InTech, 2012).

[30] L. Massüger and R. Gätzi, *Effects of groove configurations on fatigue resistance of infused sandwich panels,* The 10th International Conference on Flow Processes in Composite Materials , 1 (2010).

[31] A. May-Pat, F. Aviles, and J. Aguilar, *Mechanical properties of sandwich panels with perforated foam cores,* Journal of Sandwich Structures and Materials **13**, 427 (2011).

[32] D. Zenkert, *An Introduction To Sandwich Construction* (Engineering Materials Advisory Services, 1995) p. 277.

[33] S. Laustsen, E. Lund, L. Kühlmeier, and O. T. Thomsen, *Development of a high-fidelity experimental substructure test rig for grid-scored sandwich panels in wind turbine blades,* Strain **50**, 111 (2014).

[34] H. Mathieson, A. Fam, and M. Asce, *In-Plane Bending and Failure Mechanism of Sandwich Beams with GFRP Skins and Soft Polyurethane Foam Core,* Journal of Composites for Construction **20**, 1 (2016).

[35] M. Johannes, J. Dulieu-Barton, E. Bozhevolnaya, and O. Thomsen, *Characterization of local effects at core junctions in sandwich structures using thermoelastic stress anaylsis,* The Journal of Strain Analysis for Engineering Design **43**, 469 (2008).

[36] M. Johannes, J. Jakobsen, O. T. Thomsen, and E. Bozhevolnaya, *Examination of the failure of sandwich beams with core junctions subjected to in-plane tensile loading,* Special Issue on the 12th European Conference on Composite Materials, ECCM 2006 **69**, 1447 (2008).

[37] P. Camanho, *Failure criteria for fibre-reinforced polymer composites,* Demegi, Feup , 1 (2002).

[38] S. W. Tsai and E. M. Wu, *A General Theory of Strength for Anisotropic Materials,* Journal of Composite Materials **5**, 58 (1971).

[39] L. J. Hart-Smith, *Predictions of the original and truncated maximum-strain failure models for certain fibrous composite laminates,* Failure Criteria in Fibre-Reinforced-Polymer Composites **58**, 179 (2004).

[40] J. Doe, *Failure Index vs Strength Ratio in Quadratic Failure Criterion (Composite Materials),* (2015).

[41] P. Camanho, S. Bowron, and F. Matthews, *Failure Mechanism Bolted CFRP,* Journal of Reinforced Plastics and Composites **17**, 205 (1998).

[42] H. Mahfuz, *Response of sandwich composites with nanophased cores under flexural loading,* Composites Part B: Engineering **35**, 543 (2004).

[43] E. E. Gdoutos and I. M. Daniel, *Failure mechanisms of composite sandwich structures,* Journal of Thermoplastic Composite Materials **16**, 345 (2004).

[44] E. Gdoutos, I. Daniel, and K.-a. Wang, *Compression facing wrinkling of composite sandwich structures,* Mechanics of Materials **35**, 511 (2003).

[45] J. L. Abot, I. M. Daniel, and E. E. Gdoutos, *Contact Law for Composite Sandwich Beams,* Journal of Sandwich Structures and Materials **4**, 157 (2002).

[46] I. M. Daniel, J. L. Abot, P. M. Schubel, and J.-J. Luo, *Response and Damage Tolerance of Composite Sandwich Structures under Low Velocity Impact,* Experimental Mechanics **52**, 37 (2012), arXiv:arXiv:1011.1669v3 .

[47] A. Russo and B. Zuccarello, *Experimental and numerical evaluation of the mechanical behaviour of GFRP sandwich panels,* Composite Structures **81**, 575 (2007).

[48] H. Mahfuz, S. Islam, M. Saha, L. Carlsson, and S. Jeelani, *Buckling of sandwich composites; Effects of core-skin debonding and core density,* Applied Composite Materials **12**, 73 (2005).

[49] T. C. Triantafillou and L. J. Gibson, *Debonding in foam-core sandwich panels,* Materials and Structures **22**, 64 (1989).

[50] D. Zenkert, *Strength of sandwich beams with interface debondings,* Composite Structures **17**, 331 (1991).

[51] Z. Suo and J. W. Hutchinson, *Interface Crack Between Two Elastic Layers,* International Journal of Fracture **43**, 1 (1990).

[52] U. Hansen, *002199839803200402.pdf,* J. Comp. Mat. **32**, 335 (1998).

[53] J. L. Avery and B. V. Sankar, *Compressive Failure of Sandwich Beams with Debonded Face-Sheets,* Journal of Composite Materials **34**, 1176 (2000).

[54] A. Truxel and J. Grenestedt, *Influence of Face/Core Interface on Debond Toughness of Foam and Balsa Cored Sandwich,* Journal of Sandwich Structures and Materials **8**, 237 (2006).

[55] G. A. Kardomateas, *The Initial Post-buckling and Growth Behavior of Internal Delaminations in Composite Plates,* Journal of Applied Mechanics **60**, 903 (1993).

[56] E. E. GDOUTOS, I. M. DANIEL, and K.-A. WANG, *Multiaxial Characterization and Modeling of a PVC Cellular Foam,* (2001).

[57] E. E. Gdoutos, I. M. Daniel, and K. A. Wang, *Failure of cellular foams under multiaxial loading,* Composites - Part A: Applied Science and Manufacturing **33**, 163 (2002).

[58] M. Johannes and O. T. Thomsen, *Localised effects in sandwich structures with internal core junctions: Modelling and experimental characterisation of load response, failure and fatigue,* in *Major Accomplishments in Composite Materials and Sandwich Structures: An Anthology of ONR Sponsored Research* (Springer, 2009) pp. 229–277.

[59] J. P. Dear, A. Puri, A. D. Fergusson, A. Morris, I. D. Dear, K. Branner, and F. M. Jensen, *Digital image correlation based failure examination of sandwich structures for wind turbine blades,* 8th International Conference on Sandwich Structures , 212 (2008).

[60] A. C. Manalo, *Behaviour of fibre composite sandwich structures under short and asymmetrical beam shear tests,* Composite Structures **99**, 339 (2013).

[61] Y. Frostig, *Buckling of sandwich panels with a flexible core—high-order theory,* International Journal of Solids and Structures **35**, 183 (1998).

[62] E. E. Gdoutos, I. M. Daniel, K.-A. Wang, and J. L. Abot, *Nonlinear behavior of composite sandwich beams in three-point bending,* Experimental Mechanics **41**, 182 (2001).

[63] P. U. Haselbach, R. D. Bitsche, and K. Branner, *The effect of delaminations on local buckling in wind turbine blades,* Renewable Energy **85**, 295 (2016).

[64] N. J. Hoff and S. Mautner, *The Buckling of Sandwich-Type Panels,* Journal of the Aeronautical Sciences **12**, 285 (1945).

[65] A. Dobyns, *Correlation of Sandwich Facesheet Wrinkling Test Results with Several Analysis Methods,* 51st American Helicopter Society (AHS) Forum , 9 (1995).

[66] L. Kuhlmeier, O. Thomsen, and E. Lund, *Large Scale Buckling Experiment and Validation of Predictive Capabilities,* in *Proceedings (CD-rom) of the 15th International Conference on Composite Materials (ICCM-15)* (2005).

[67] L. Kuhlmeier, *Buckling of Wind Turbine Rotor Blades: Analysis, Design and Experimental Validation*, Ph.D. thesis, Aalborg Universitet (2007).

[68] L. C. T. Overgaard, E. Lund, and O. T. Thomsen, *Structural collapse of a wind turbine blade. Part A: Static test and equivalent single layered models,* Composites Part A: Applied Science and Manufacturing **41**, 257 (2010).

[69] L. C. T. Overgaard and E. Lund, *Structural collapse of a wind turbine blade. Part B: Progressive interlaminar failure models,* Composites Part A: Applied Science and Manufacturing **41**, 271 (2010).

[70] F. Stoll and D. Griffin, *Blade Design with Engineered Cores Materials Sandwich Construction in Large Blades*, Tech. Rep. (Webcore Fiber Reinforced Composite Foam Cores, 2008).

[71] F. Stoll, D. Ph, and S. D. Engineer, *Recent Core Material Developments / Applications for Blades at Milliken Sandwich Core in Large Blades*, Tech. Rep. (Milliken, 2012).

[72] A. I. Marasco, D. D. R. Cartié, I. K. Partridge, and A. Rezai, *Mechanical properties balance in novel Z-pinned sandwich panels: Out-of-plane properties,* Composites Part A: Applied Science and Manufacturing **37**, 295 (2006).

[73] N. Mitra, *A methodology for improving shear performance of marine grade sandwich composites: Sandwich composite panel with shear key,* Composite Structures **92**, 1065 (2010).

[74] ASTM Standard, *ASTM C273-00 Standard Test Method for Shear Properties of Sandwich Core Materials,* ASTM International , 1 (2000).

[75] A. standard, *C297/C297M Standard Test Method for Flatwise Tensile Strength of Sandwich Constructions,* ASTM International **04**, 1 (2013).

[76] ASTM Standard, *ASTM C393-06 Standard Test Method for Core Shear Properties of Sandwich Constructions by Beam Flexure,* ASTM International **i**, 1 (2010).

[77] *Stress-Strain Diagrams and Material Properties,* (2017).

[78] ASTM Standard, *ASTM C365-08 Standard Test Method for Flatwise Compressive Properties of Sandwich Cores,* ASTM International , 32 (2010).

[79] V. A. Company, *Divinycell - Technical Manual,* Material Technical Data Sheet , 1 (1985).

[80] V. S. Deshpande and N. A. Fleck, *Multi-axial yield behaviour of polymer foams,* Acta Materialia **49**, 1859 (2001).

[81] G. M. Viana and L. A. Carlsson, *Mechanical Properties and Fracture Characterization of Cross-Linked PVC Foams,* Journal of Sandwich Structures and Materials **4**, 99 (2002).

[82] S. Taher, O. Thomsen, and J. Dulieu-Barton, *Mechanical characterization of PVC foam using digital image correlation and nonlinear FE,* Proceedings of the 18th International Conference on Composite Materials (ICCM-18), Jeju Island, Republic of Korea , 1 (2011).

[83] ASTM Standard, *ASTM C364-08 Standard Test Method for Edgewise Compressive Strength of Sandwich Constructions,* ASTM International , 24 (2010).

A

CHARACTERISATION APPENDIX

A.1. FACINGS CHARACTERISATION

The facing material that is used in the aforementioned (sandwich) material tests are weaves built up of OC Advantex SE1500 fibres. Two types of weaves are used depending on the test type, namely a biax(±45) or a triax(0 ± 45) weave. The biax and triax weaves have areal weights of 833 and 1185 $g/m2$ respectively. Raw test data for these (infused) weaves are available from Suzlon Blades Technology for edgewise tension/compression and flatwise compression. This test data will be used in the following subsections to characterise the facing's load response.

A.1.1. EDGEWISE TENSILE (ET) CHARACTERISATION

The test standard used for this test is ISO 14129. The lay-up used for both biax and triax tests is 2 layers of weave in a 0 degree orientation. Four Kyowa KFG-5-120-C1-11, 5mm strain gauges are used per test specimen, of which 2 per facing in a 0/90° manner. This test type yields a tensile stress-strain response, but also a shear stress-strain response. There were 9 specimens tested for both weave types, and their averaged sizes are shown in Table A.1. These averages have been made using measurements along 3 positions of the specimens. The test bench yields force and displacement data, and the strain gauges yield strain data. From the force F and cross-sectional area of the specimens, the stress can be computed using Equation A.1.

$$\sigma = \frac{F}{w \cdot t} \tag{A.1}$$

For the 0° oriented strain gauges, test results are plotted versus the stress for all 9 specimens in Figure A.1a for

Table A.1: Specimen sizes for the SBT edgewise tensile test coupons.

	Biax	Triax
Width w [mm]	24.98	24.97
Thickness t [mm]	3.22	2.31
Gauge Length l_g [mm]	149.7	149.8
Total Length l_t [mm]	250	250

the front side measurements and Figure A.1b for the back side measurements. In the front side strain gauge measurements, starting at a strain value of approximately 6.2%, specimen 9 shows a deviating behaviour non-conform the rest of the specimens. Similarly, specimen 1 exhibits this same behaviour for the back side measurements. Their corresponding opposite side measurements however do not show this unstable behaviour and hence the behaviour is probably caused by a debonded or partially debonded strain gauge. Also specimen 2 seems to fail prematurely at a strain of 7.21%. The test results of coupons 1, 2 and 9 will be disregarded in further analysis. All other specimens show very similar trends, which are to be expected trends for this type of specimens.

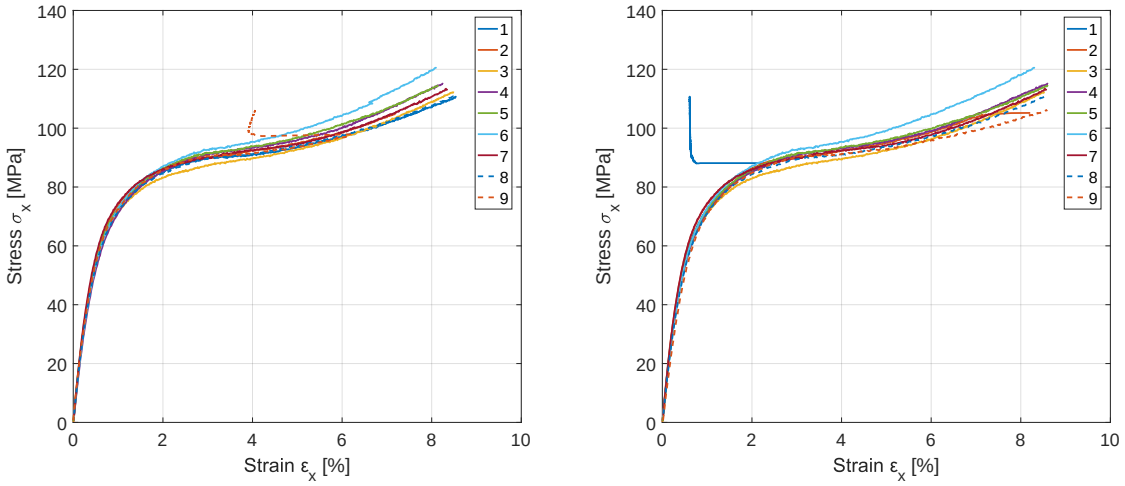

(a) Front side 0° oriented strain gauge measurements.

(b) Back side 0° oriented strain gauge measurements.

Figure A.1: 0° oriented strain gauge measurements for the edgewise tensile test of the biax coupons.

The tensile Young's modulus of these specimens is calculated by taking the slope of the graph between 0.05 and 0.30% strain. This range of values is chosen because it shows very uniform behaviour for all test specimens. At close to 0 and from 0.4[%] strains, the behaviour is less uniform. This stiffness is then computed as a slope for each specimen and averaged over all valid tests. This average stiffness (Young's Modulus E) is highlighted in Figure A.2a. The strain at which damage initiates is defined by the 0.2% offset method for each specimen. Basically this offsets the elastic modulus line by 0.2% strain and where this line crosses the stress-strain curve, the damage initiation point is located. This is shown schematically in Figure A.2b, where σ_Y signifies the stress at damage initiation, and σ_{PL} signifies the stress at the start of plastic deformation. A summary of the averaged results of the 6 qualifying test specimens is given in Table A.2.

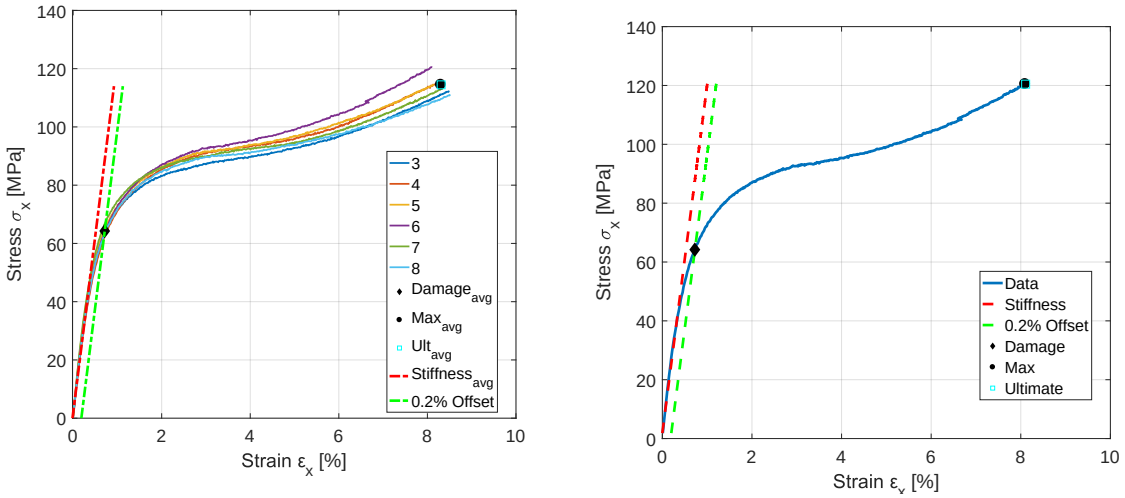

(a) ET test front side 0° oriented strain gauge measurements.

(b) Schematic representation of the 0.2% strain offset [77].

Figure A.2: Front side measurements and computed important parameters.

In this test method, also 90° orientated strain gauges are used, from which together with the 0° orientated strain gauges, the shear strain can be computed using Equation A.2, and the shear stress by Equation A.3. Doing this for all 9 test specimens, the specimens' shear stress - shear strain response can be plotted as seen in Figures A.3a and A.3b. From these results, specimens 1, 2 and 9 are further omitted because of non-uniform

behaviour. Per specimen, the stiffness, strain at damage initiation, maximum strain and ultimate strain together with stresses are calculated. These results are averaged for all 6 qualifying test specimens, leading to the facings' average structural properties as summarised in Table A.2. These averages are shown together with the specimens' stress-strain graphs in Figures A.4a and A.4b.

$$\gamma_{xy} = \varepsilon_0 - \varepsilon_{90} \tag{A.2}$$

$$\tau_{xy} = \frac{F}{2 \cdot w \cdot t} \tag{A.3}$$

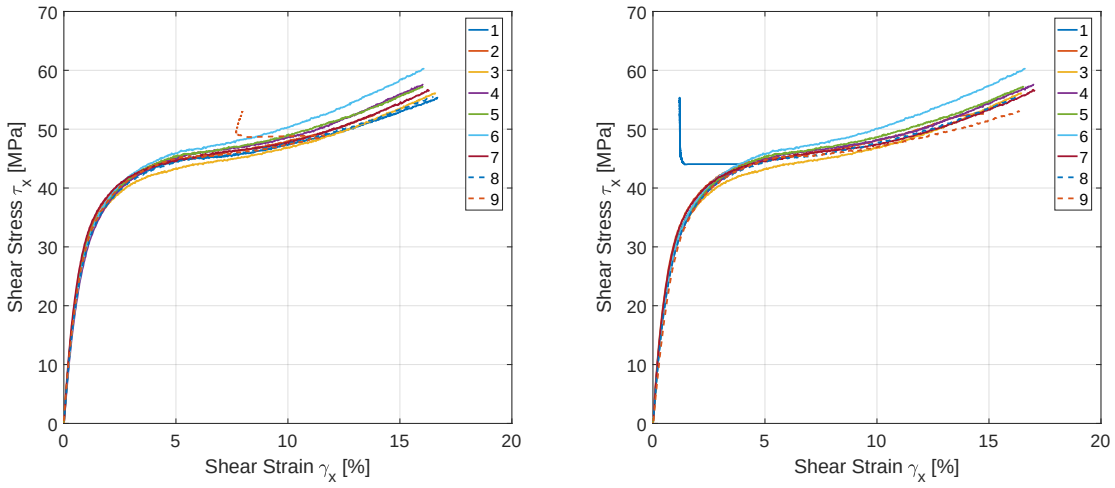

(a) ET test shear stress vs shear strain - front facing.

(b) ET test shear stress vs shear strain - back facing.

Figure A.3: Edgewise tensile test shear stress vs shear strain curves - front and back facing.

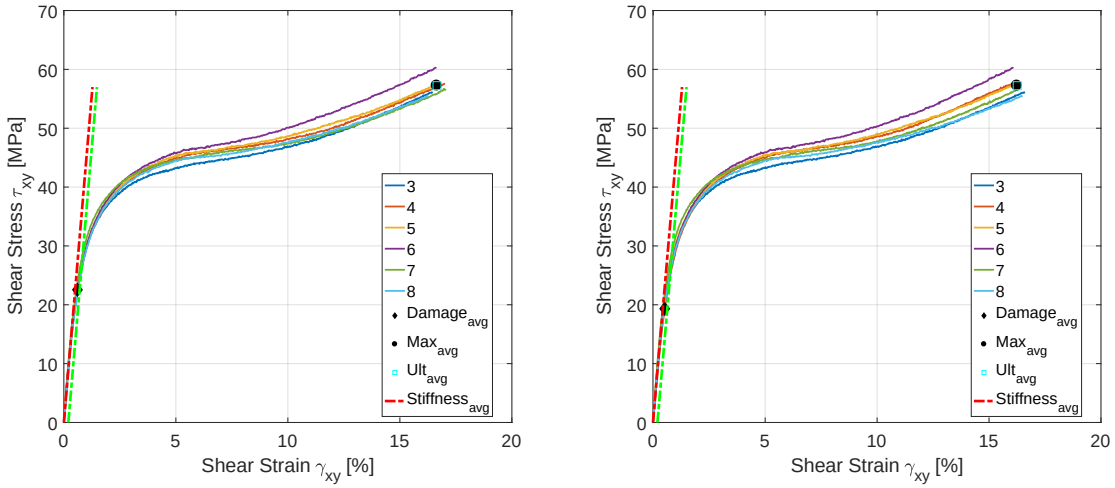

(a) ET test shear stress vs shear strain - front facing.

(b) ET test shear stress vs shear strain - back facing.

Figure A.4: Edgewise tensile test shear stress vs shear strain curves - front and back facing - including average values.

For the triax facing material, tests are performed in the similar manner, and data is also processed in the same manner. Coupon dimensions for the triax tests are shown in Table A.1. For these tests, also 9 specimens are tested, of which all 9 results are usable without any deviating results as can be seen in Figures A.5a-A.5d. The results show that the triax material exhibits an almost completely linear deformation and a brittle failure mode. This in contrast with the biax material because of the difference in weave (±45 for the biax and 0±45

Table A.2: Averaged data from all edgewise tensile characterisation tests for both biax and triax materials. Units for stresses and moduli are [MPa] and units for strains are [%].

BIAX, n=6		ε_{dmg} [%]	σ_{dmg} [MPa]	ε_{max} [%]	σ_{max} [MPa]	ε_{ult} [%]	σ_{ult} [MPa]	E [MPa]
Front	Mean	7.14E-01	6.43E+01	8.30E+00	1.15E+02	8.31E+00	1.14E+02	1.22E+04
	St. Dev.	1.27E-02	1.21E+00	1.76E-01	3.27E+00	1.73E-01	3.26E+00	4.91E+02
	Variance	1.60E-04	1.46E+00	3.09E-02	1.07E+01	2.98E-02	1.06E+01	2.41E+05
Back	Mean	7.11E-01	6.37E+01	8.52E+00	1.15E+02	8.53E+00	1.14E+02	1.23E+04
	St. Dev.	1.00E-02	1.13E+00	1.14E-01	3.27E+00	1.11E-01	3.26E+00	4.02E+02
	Variance	1.00E-04	1.28E+00	1.29E-02	1.07E+01	1.23E-02	1.06E+01	1.62E+05
		γ_{dmg} [%]	τ_{dmg} [MPa]	γ_{max} [%]	τ_{max} [MPa]	γ_{ult} [%]	τ_{ult} [MPa]	G [MPa]
Front Shear	Mean	7.89E-01	2.65E+01	1.66E+01	5.73E+01	1.67E+01	5.72E+01	4.47E+03
	St. Dev.	1.10E-02	6.26E-01	2.88E-01	1.64E+00	3.15E-01	1.63E+00	1.95E+02
	Variance	1.20E-04	3.91E-01	8.29E-02	2.68E+00	9.93E-02	2.66E+00	3.80E+04
Back Shear	Mean	8.01E-01	2.69E+01	1.62E+01	5.73E+01	1.63E+01	5.72E+01	4.39E+03
	St. Dev.	1.84E-02	5.88E-01	2.50E-01	1.64E+00	2.42E-01	1.63E+00	1.95E+02
	Variance	3.38E-04	3.45E-01	6.26E-02	2.68E+00	5.88E-02	2.66E+00	3.80E+04
TRIAX, n=9		ε_{dmg} [%]	σ_{dmg} [MPa]	ε_{max} [%]	σ_{max} [MPa]	ε_{ult} [%]	σ_{ult} [MPa]	E [MPa]
Front	Mean	1.58E+00	4.00E+02	2.30E+00	5.56E+02	2.30E+00	5.56E+02	2.89E+04
	St. Dev.	1.17E-01	3.73E+01	6.59E-02	2.14E+01	6.51E-02	2.15E+01	9.37E+02
	Variance	1.37E-02	1.39E+03	4.34E-03	4.59E+02	4.23E-03	4.62E+02	8.78E+05
Back	Mean	1.68E+00	4.22E+02	2.29E+00	5.56E+02	2.29E+00	5.56E+02	2.85E+04
	St. Dev.	9.84E-02	2.88E+01	8.86E-02	2.14E+01	8.80E-02	2.16E+01	1.14E+03
	Variance	9.69E-03	8.30E+02	7.85E-03	4.59E+02	7.74E-03	4.66E+02	1.29E+06
		γ_{dmg} [%]	τ_{dmg} [MPa]	γ_{max} [%]	τ_{max} [MPa]	γ_{ult} [%]	τ_{ult} [MPa]	G [MPa]
Front Shear	Mean	1.40E+00	1.21E+02	3.72E+00	2.78E+02	3.73E+00	2.78E+02	1.01E+04
	St. Dev.	6.59E-02	8.01E+00	8.74E-02	1.07E+01	8.53E-02	1.05E+01	3.27E+02
	Variance	4.35E-03	6.41E+01	7.65E-03	1.15E+02	7.28E-03	1.10E+02	1.07E+05
Back Shear	Mean	1.49E+00	1.26E+02	3.76E+00	2.78E+02	3.76E+00	2.78E+02	9.76E+03
	St. Dev.	8.51E-02	1.02E+01	1.44E-01	1.07E+01	1.43E-01	1.07E+01	3.48E+02
	Variance	7.24E-03	1.04E+02	2.07E-02	1.15E+02	2.03E-02	1.16E+02	1.21E+05

for the triax material). This behaviour is as expected. The structural properties resulting from these tests are computed in the same manner as for the biax case and the results are summarised in Table A.2.

A.1.2. EDGEWISE COMPRESSION (EC) CHARACTERISATION

Analysis on these specimens is done in exactly the same manner as for the edgewise tensile specimens. Resulting graphs are shown in Figures A.6-A.7 and the resulting data is given in Table A.4.

The test standard used for this test is ISO 14126; "Determination of compressive properties in the in-plane direction". The lay-up used for both biax and triax tests is 2 layers of weave in a 0° orientation. Two 2mm cross strain gauges are used per test specimen, of which 1 per facing in a 0° manner. This test type yields a compressive stress-strain response, but also a compressive shear stress-strain response. There were 9 specimens tested for both weave types, and their averaged sizes are shown in Table A.3. These averages have been made using measurements along 3 positions of the specimens. The test bench yields force and displacement data, and the strain gauges yield strain data. From the force F and cross-sectional area of the specimens, the stress can be computed using Equation A.1.

Figures A.6a and A.6b show the stress strain data for all 9 specimens. Specimen 4,5,7 and 8 fail prematurely due to debonding of the strain gauge. They will further be excluded from analysis.

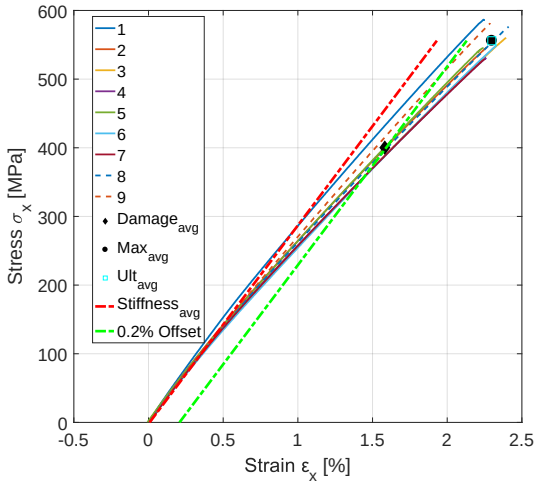

(a) ET test stress vs strain - triax front facing.

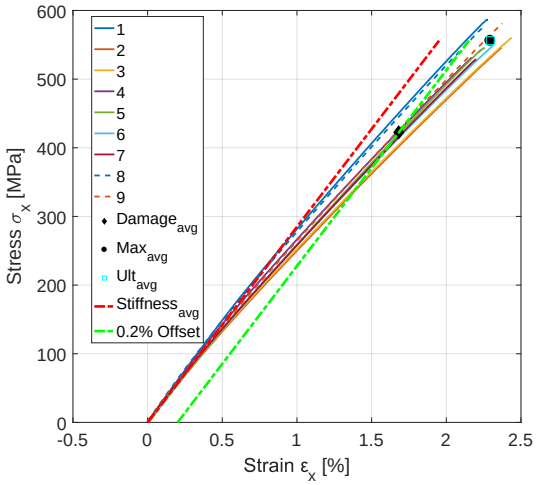

(b) ET test stress vs strain - triax back facing.

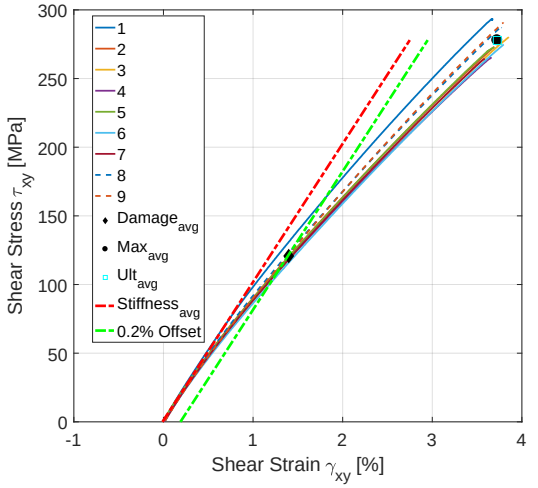

(c) ET test shear stress vs shear strain - triax front facing.

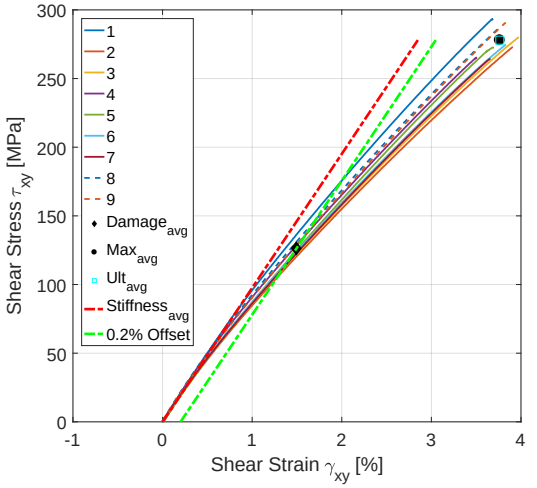

(d) ET test shear stress vs shear strain - triax back facing.

Figure A.5: Triax lay-up normal stress-strain and shear stress-strain curves indicating average values for damage, maximum and ultimate stresses and strains.

Table A.3: Specimen sizes for the SBT edgewise compression test coupons.

	Biax	Triax
Width w	10.08	25.01
Thickness t	3.35	3.24
Gauge Length l_g	10.1	24.9
Total Length l_t	136.9	150.0

The results of the triax specimens are shown in Figures A.7a and A.7b. It can be seen that nearing the end of the analysis, the specimen starts to grow towards high positive or negative strains. While this happens, its counterpart (front or back) moves the opposite way. Hence can be concluded that the specimen fails right before showing buckling behaviour. For buckling behaviour to occur, the strain measurements on one of both sides should be positive.

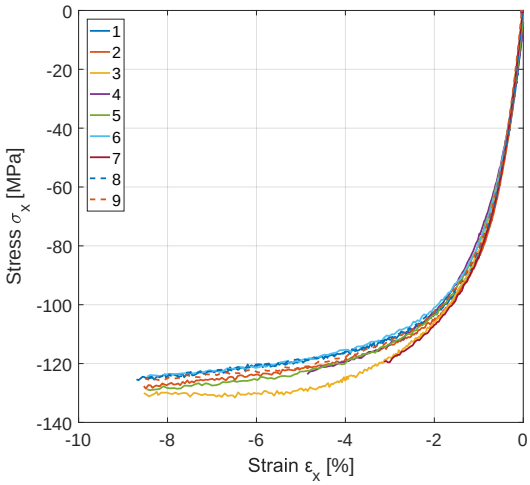

(a) Biax EC test front side 0° oriented strain gauge measurements.

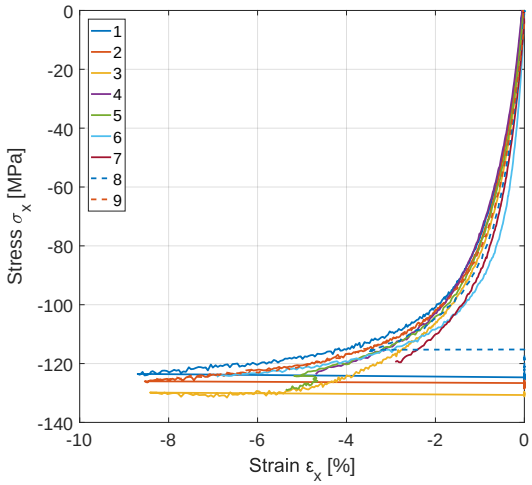

(b) Biax EC test back side 0° oriented strain gauge measurements.

Figure A.6: 0° oriented strain gauge measurements for the edgewise tensile test of the biax coupons.

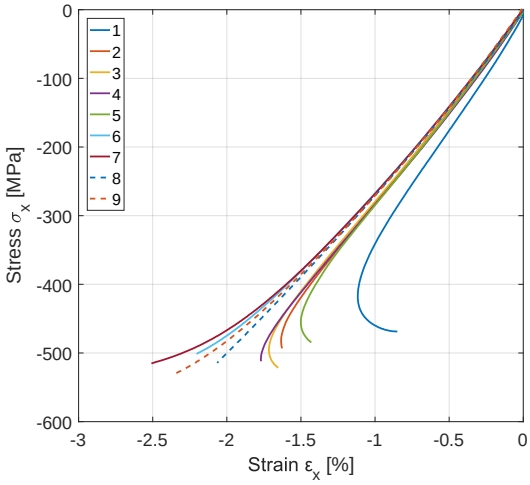

(a) Triax EC test front side 0° oriented strain gauge measurements.

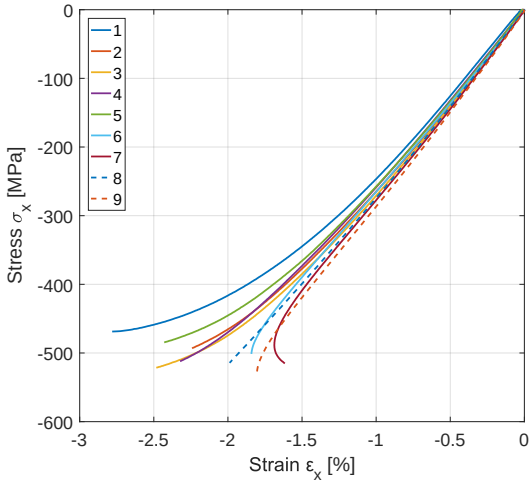

(b) Triax EC test back side 0° oriented strain gauge measurements.

Figure A.7: 0° oriented strain gauge measurements for the edgewise tensile test of the biax and triax coupons.

A.1.3. FLATWISE COMPRESSION CHARACTERISATION

Analysis on these specimens is done in exactly the same manner as for the edgewise tensile and compressive specimens. Resulting graphs are shown in Figures A.8a-A.9b and the resulting data is given in Table A.6.

The test standard used for this test is ASTM C365; "Flatwise Compressive Properties of Sandwich Cores". The lay-up used for both biax and triax tests is 2 layers of weave in a 0 degree orientation. This test type yields a compressive stress-strain response. There were 6 specimens tested for both weave types, and their averaged sizes are shown in Table A.5. These averages have been made using measurements along 3 positions of the specimens. The test bench yields force and displacement data, and the strain gauges yield strain data. From the force F and cross-sectional area of the specimens, the stress can be computed using Equation A.1.

As can be seen in Figures A.8a, A.9a and A.9b, at low strains the stress-strain curve is almost horizontal. This region is called a toe region as also discussed in the paper on the test standard [78] (Figure A.8b, where it

Table A.4: Averaged data from all edgewise compression characterisation tests for both biax and triax materials. Units for stresses and moduli are [MPa] and units for strains are [%].

BIAX, n=5		ε_{dmg} [%]	σ_{dmg} [MPa]	ε_{max} [%]	σ_{max} [MPa]	ε_{ult} [%]	σ_{ult} [MPa]	E [MPa]
Front	Mean	-7.85E-01	-7.22E+01	-8.06E+00	-1.27E+02	-8.55E+00	-1.27E+02	1.23E+04
	St. Dev.	1.81E-02	1.28E+00	8.97E-01	2.86E+00	8.97E-02	2.28E+00	7.37E+02
	Variance	3.28E-04	1.64E+00	8.04E-01	8.20E+00	8.05E-03	5.21E+00	5.43E+05
Back	Mean	-7.59E-01	-7.30E+01	-7.73E+00	-1.26E+02	-8.17E+00	-1.26E+02	1.29E+04
	St. Dev.	6.29E-02	6.70E+00	8.76E-01	3.02E+00	7.18E-01	2.44E+00	2.04E+03
	Variance	3.96E-03	4.48E+01	7.67E-01	9.10E+00	5.16E-01	5.95E+00	4.15E+06
TRIAX, n=9		ε_{dmg} [%]	σ_{dmg} [MPa]	ε_{max} [%]	σ_{max} [MPa]	ε_{ult} [%]	σ_{ult} [MPa]	E [MPa]
Front	Mean	-1.49E+00	-4.03E+02	-1.87E+00	-4.92E+02	-1.87E+00	-4.92E+02	3.00E+04
	St. Dev.	2.19E-01	3.83E+01	4.46E-01	3.45E+01	4.46E-01	3.45E+01	1.65E+03
	Variance	4.81E-02	1.47E+03	1.99E-01	1.19E+03	1.99E-01	1.19E+03	2.73E+06
Back	Mean	-1.68E+00	-4.26E+02	-2.18E+00	-5.02E+02	-2.18E+00	-5.02E+02	2.82E+04
	St. Dev.	1.48E-01	4.85E+01	3.67E-01	1.94E+01	3.67E-01	1.94E+01	1.09E+03
	Variance	2.19E-02	2.35E+03	1.34E-01	3.78E+02	1.34E-01	3.78E+02	1.20E+06

is stated that this region is "an artifact caused by a take-up of slack and alignment or seating of the specimen". It is further discussed that this artifact should be corrected for by finding the stiffness on the linear portion of the stress-strain graph and finding it's intersection with the strain axis. This intersection will then be the new strain 0-point.

Table A.5: Specimen sizes for the SBT flatwise compression test coupons.

	Biax	Triax
Width w [mm]	19.33	19.35
Thickness t [mm]	2.78	3.56
Total Length l_t [mm]	19.8	19.4

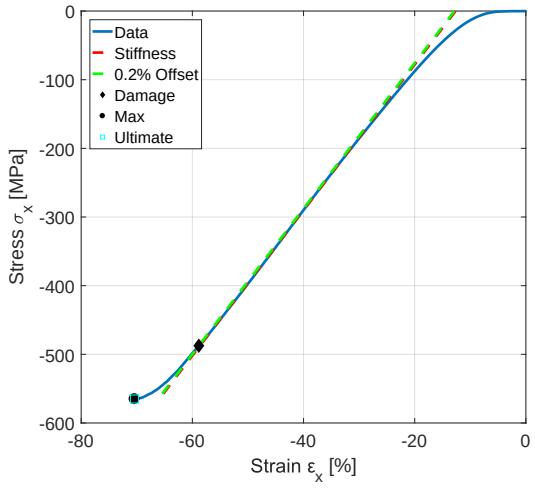

(a) FC test Biax833 specimen 2.

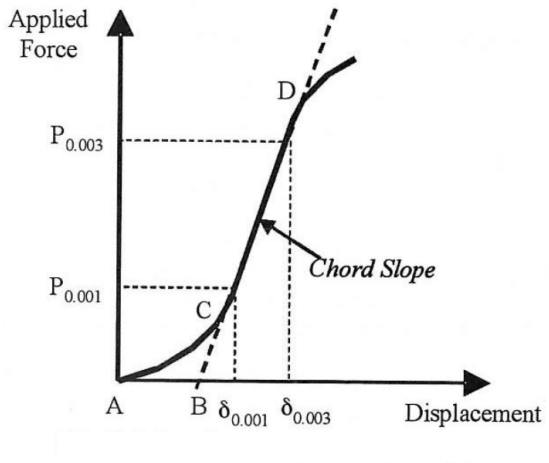

(b) Toe region [78].

Figure A.8: Stress-strain curves for biax and triax specimens loaded in flatwise compression.

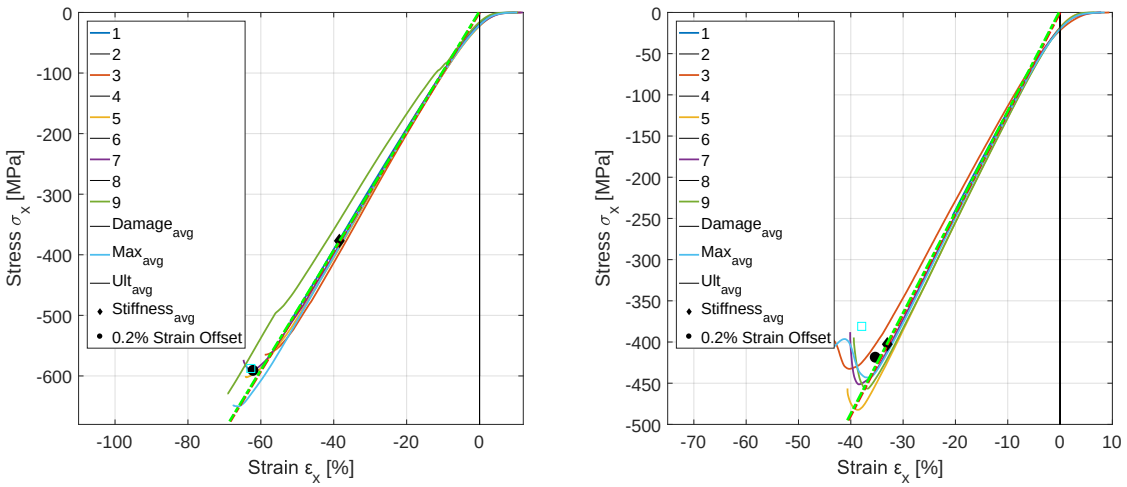

(a) FC Biax833 in flatwise compression.

(b) FC Triax1185 in flatwise compression.

Figure A.9: Stress-strain curves for biax and triax specimens loaded in flatwise compression.

Table A.6: Averaged data from all flatwise compression characterisation tests for both biax and triax materials. Units for stresses and moduli are [MPa] and units for strains are [%].

BIAX, n=6	ε_{dmg} [%]	σ_{dmg} [MPa]	ε_{max} [%]	σ_{max} [MPa]	ε_{ult} [%]	σ_{ult} [MPa]	E [MPa]
Mean	-3.85E+01	-3.77E+02	-6.21E+01	-5.91E+02	-6.28E+01	-5.88E+02	9.87E+02
Standard Deviation	1.76E+01	1.78E+02	5.97E+00	4.93E+01	6.29E+00	4.90E+01	4.83E+01
Variance	3.08E+02	3.18E+04	3.56E+01	2.43E+03	3.96E+01	2.41E+03	2.33E+03
TRIAX, n=6	ε_{dmg} [%]	σ_{dmg} [MPa]	ε_{max} [%]	σ_{max} [MPa]	ε_{ult} [%]	σ_{ult} [MPa]	E [MPa]
Mean	-3.30E+01	-4.03E+02	-3.53E+01	-4.19E+02	-3.79E+01	-3.81E+02	1.22E+03
Std. Dev.	8.24E+00	1.04E+02	7.31E+00	8.58E+01	8.65E+00	7.02E+01	5.18E+01
Variance	6.78E+01	1.07E+04	5.35E+01	7.36E+03	7.49E+01	4.92E+03	2.68E+03

A.2. AIREX C70.55 PVC CORE CHARACTERISATION

The used core material is the Airex® C70.55 foam produced by 3A Composites, which is a closed cell, cross-linked polymer foam (PVC). The number "55" indicates its density which according to the manufacturers lies in the typical range of $54-69 kg/m^3$. The rest of the material's properties as specified by the manufacturer are shown in Table 4.1. From the manufacturer's data it is important to note that with a varying density, also the structural properties of the foam core material are varying. Minimum values are supplied by the manufacturer, making fail safe design easier. However it has to be kept in mind that this varying range of properties can be a cause of deviating test results.

Although these properties can be used to give a good indication of the material behaviour under different load cases, they do not include any non-linear material behaviour. A study performed by Berthelot et al. [8] aims to evaluate the non-linear behaviour of foam sandwich materials in FE analyses. In the study, the same C70.55 core material as discussed above is used. Since the linear behaviour of this foam type is only limited to a few percent of strain, it is important to characterise its non-linear stress-strain response to make accurate predictions for the rest of the strain range.

The characterisation data as given by Berthelot et al. [8] can be used for this research, keeping in mind that the properties of the foam can vary depending on the production batch, as also indicated by the manufacturer. In the following subsections, the derivation of the non-linear behaviour properties of the C70.55 core material as studied by Berthelot et al. will be discussed.

A.2.1. COMPRESSIVE CHARACTERISATION

In the study performed by Berthelot et al., ten C70.55 PVC foam specimens are tested in flatwise (also known as out-of plane or transverse) compression as shown in Figure A.10a. Their dimensions are $50mm$ x $50mm$ with a thickness of $15mm$. It has to be noted that Berthelot et al. have not specified a used test standard, nor have they specified any further information on the statistical significance of the results. However the specimen sizes are compliant to the ASTM C365 test standard for flatwise compressive properties of a core material. Figure A.10b shows the test setup used, where it can be seen that a displacement transducer is fixed to the upper support to measure the displacement of the supports and thus specimens.

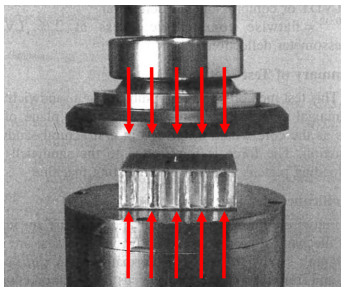

(a) ASTM C365: flatwise compression load [78]

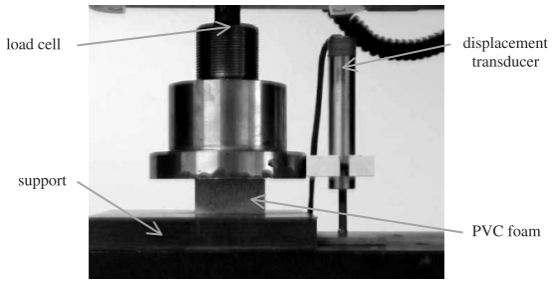

(b) Flatwise compression test setup [8]

Figure A.10: Flatwise compression test type schematic and test setup picture

From the flatwise compression tests, Berthelot et al. concluded that all specimens showed similar results and a good homogeneity of the foam fabrication. Figure A.11a shows obtained stress-strain curves for one of the tests. The behaviour observed is typical for closed-cell foam cores [8], where first a linear-elastic deformation behaviour is observed up to a strain of approximately 4%, followed by an extensive stress plateau indicating plastic deformation, and lastly foam densification which causes a steeply increasing stress for strains higher than 60%. The graph also indicates that a higher density core material (C70.75; $80kg/m^3$ nominal density), exhibits a higher plateau stress with similar strain values at beginning and end of the plateau as for the lower density core (C70.55). Berthelot et al. add that for the plateau, the volume of the foam changes, leading to a effective Poisson's ratio of zero in this case.

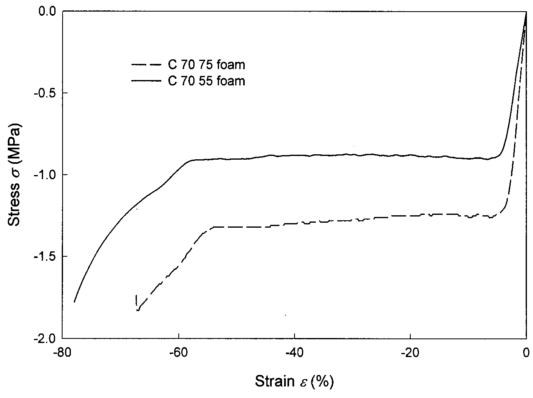

(a) Flatwise compression results [8].

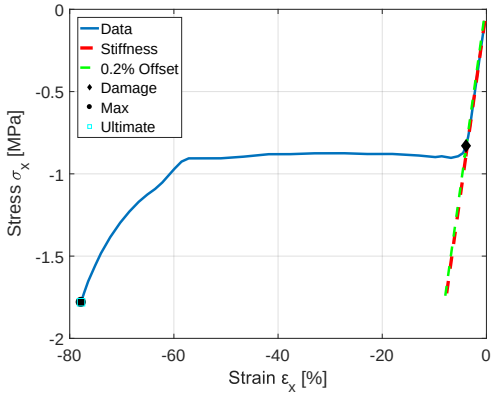

(b) Analysis of flatwise compression data from figure A.11a.

Figure A.11: Flatwise compression stress-strain curves from research by Berthelot et al. [8].

Figure A.11b is an approximation to Figure A.11a by picking and interpolating data points. The Young's modulus of the foam material in this compression test is shown as the red striped line in the graph and is approximately $22.5MPa$, where Berthelot et al. have derived a Young's modulus of $27MPa$ from their tests. Reasons for this can be either that the used interpolation points as shown in Figure A.11b are not accurate enough, or that the value given by Berthelot et al. is an averaged value over all 10 test specimens. In any case,

the values as reported by Berthelot et al. are probably more accurate since they possess more data.

Apart from the fact that a test standard has not been named and no statistical data is available (other than the fact that the test was conducted on 10 specimens), the research as performed by Berthelot et al. seems well structured and therefore his test result data on the compressive properties of this core type will be considered correctly characterised data. Their test results are summarised in Table A.7.

Table A.7: Mechanical characteristics of the C70.55 foam subjected to transverse (through-thickness) and in-plane compression.

Properties	Transverse Compression	In-plane Compression
Young's Modulus E [MPa]	27	20
Poisson's Ratio[1] [-]	0.42	0.42
σ_{Damage} [MPa]	0.85	0.60
ϵ_{Damage} [%]	4	3
$\sigma_{PlateauStart}$ [MPa]	0.87	0.68
$\epsilon_{PlateauStart}$ [%]	5	4
$\sigma_{PlateauEnd}$ [MPa]	0.92	0.70
$\epsilon_{PlateauEnd}$ [%]	58	40
σ_{Ult} [MPa]	1.8	1.6
ϵ_{Ult} [%]	77	77

Because of the roll-forming production process of this foam type, cells are elongated in the forming plane, and hence the foam's properties are expected to be different in through-thickness and in-plane directions. In Berthelot et al.'s study, the foam was also tested in in-plane compression. Used test specimens were $120mm$x$15mm$ with a thickness of $15mm$. No information on the accuracy or the statistical significance of results, amount of test specimens used, or test standard used is available.
Figure A.12a shows obtained stress-strain curves for one of the tests. A very similar behaviour is observed as in the transverse compressive test. The results of this test are summarised in Table A.7. A significant difference can be seen when comparing transverse and in-plane compression responses as shown in Figure A.12b. The stiffness and stress values are higher for the transverse compression case. This difference can be attributed to the earlier mentioned roll-forming production process as also discussed by Berthelot et al. [8].

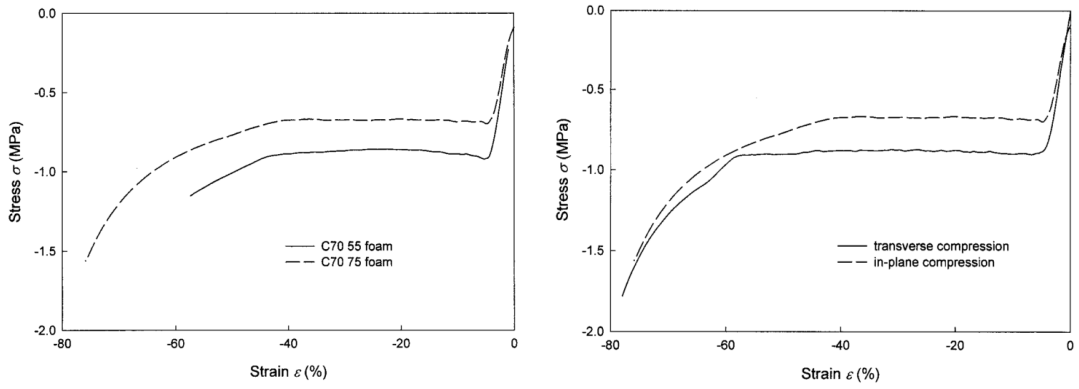

(a) In-plane compression results [8]. (b) Comparison Transverse & In-plane Compression [8]

Figure A.12: In-plane compression stress-strain curves from research by Berthelot et al. [8].

[1] For Linear-Elastic part of deformation

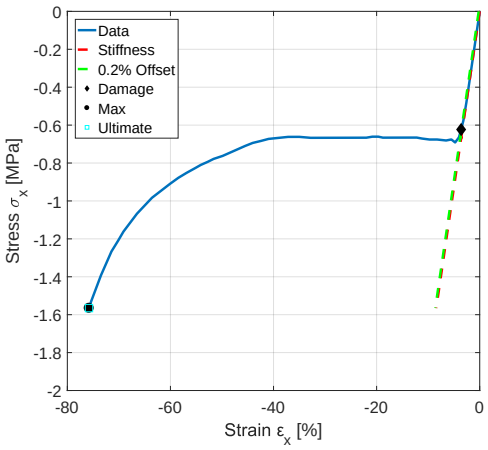

Figure A.13: Analysed data from data in Figure A.12a.

A.2.2. TENSILE CHARACTERISATION

For the edgewise tensile characterisation, Berthelot et al. [8] have tested foam specimens with constant cross-sectional areas. For this test, tabs were bonded to the edges of the specimens leading to gauge dimensions of $180mm$ x $25mm$ with a thickness of $15mm$. Again extensometers are used, but this time in longitudinal and transverse directions. The test standard used, and the number of specimens tested was not specified by Berthelot et al., neither was any information on the accuracy or the statistical significance of the results.

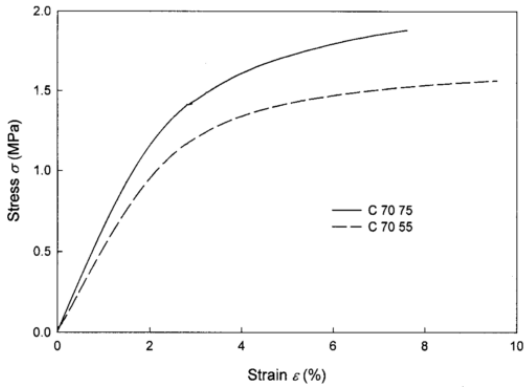

(a) Edgewise tensile results [8].

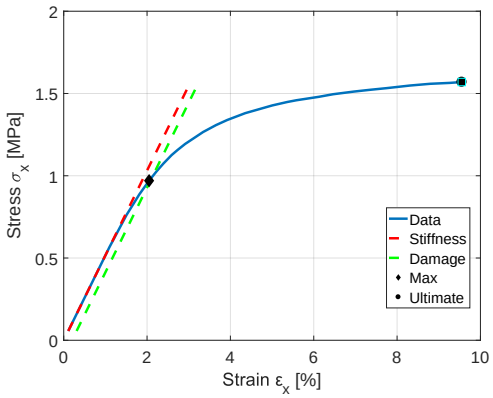

(b) Approximation to C70.55 data set in Figure A.14a

Figure A.14: Edgewise tension stress-strain curves from research by Berthelot et al. [8].

Figure A.14a shows obtained stress-strain curves for one of the tests. The behaviour observed is typical for closed-cell foam cores [8], where in the first portion of the graph up to a strain of approximately 2%, the foam material behaves linearly elastic as expected, and then transitions into non-linear behaviour with progressively decreasing stress-strain slope until failure at 9.55% strain. For the higher density foam also plotted in Figure A.14a, the Young's modulus and fracture stress are about 20% higher, at a lower ultimate failure strain of approximately 7.5%.

Apart from the fact that a test standard has not been named and no statistical data is available, the research as performed by Berthelot et al. seems well structured and therefore their test result data on the tensile properties of this core type will be considered correctly characterised data. Their test results are summarised in Table A.8.

[2] For Linear-Elastic part of deformation

Table A.8: Mechanical characteristics of the C70.55 foam subjected to transverse (through-thickness) and in-plane tension.

Properties	In-plane Tension
Young's Modulus E [MPa]	45
Poisson's Ratio[2] [-]	0.42
σ_{Damage} [MPa]	0.8
ϵ_{Damage} [%]	1.6
σ_{Ult} [MPa]	1.55
ϵ_{Ult} [%]	9.8

No flatwise tensile characterisation data of this type of foam core is available. For the Divinycell H100 foam, such data is however available from multiple sources such as [9, 79–82], and more. From these sources it can be concluded that the material characterisation data is very dependent on the batch of material used and tested. Strangely the ratios between in-plane and out-of-plane stiffnesses also deviate between 1 and 2.2, which is quite a big difference.
The Airex C70.55 PVC core material used in this research is also a PVC foam. Assuming that the production process and material are very similar, it can be concluded that without characterising the material ourselves, the properties used in FE analysis might be deviating quite a lot with respect to the actually used batch of material. For simplicity the most conservative path will be taken and it will be assumed that the flatwise tensile properties are equal to the edgewise tensile properties between which the ratio is thus 1.

A.3. SANDWICH CHARACTERISATION

In this section, the benchmark grid-scored sandwich structure is characterised in the following loading types; edgewise compression, edgewise tension, and flatwise compression.

A.3.1. EDGEWISE COMPRESSION

The used test method is "ASTM C 364/C 364M - 07" or "Standard Test Method for Edgewise Compressive Strength of Sandwich Constructions" [83]. Acceptable and unacceptable failure modes for this standard are shown in Figure A.15. Failure modes are only acceptable if they occur away from the supported ends. Assuming thin facings, the failure mode is usually face sheet wrinkling in which the core deforms due to the wavy shape of the facings leading to bending of the sandwich and resulting in crimping near the ends as a result of shear failure of the core. Other accepted failure modes are facesheet compression failure. At least 5 specimens should be tested per test condition to obtain statistically significant data. By applying this test method to coupon testing, its edgewise compressive strength is obtained.

The constituents used in the sandwich coupons are Advantex SE1500 tri-axial glass fibre mats, Airex C70.55CK PVC foam core and resin system Y (cannot be specified due to confidentiality). These materials are compliant for use with this test standard, and the design parameters for the test coupons satisfy the requirements as shown in Figure A.16. The design and actual (measured) coupon dimensions are given in Table A.9.

Table A.9: EC: Design and actual coupon dimensions. Average values based on 6 test coupons.

Dimension	Design Value	Measured Value
Width b [mm]	60	59.41
Total Length L_{tot} [mm]	270	269.5
Gauge Length L_{gauge} [mm]	150	148.4
Sandwich thickness t_s [mm]	22	22.25
Core Thickness t_c [mm]	20	20.02

For this test, six test specimens were tested. Test specimen dimensions are $60mm$ x $270mm$ with a total thickness of $22.25mm$ on average. During production of the test specimens, monolithic glass fibre tabs (blue-greenish colour) of 60 x 60mm are laminated within the structure as visible in Figures A.17a-A.19b to prevent

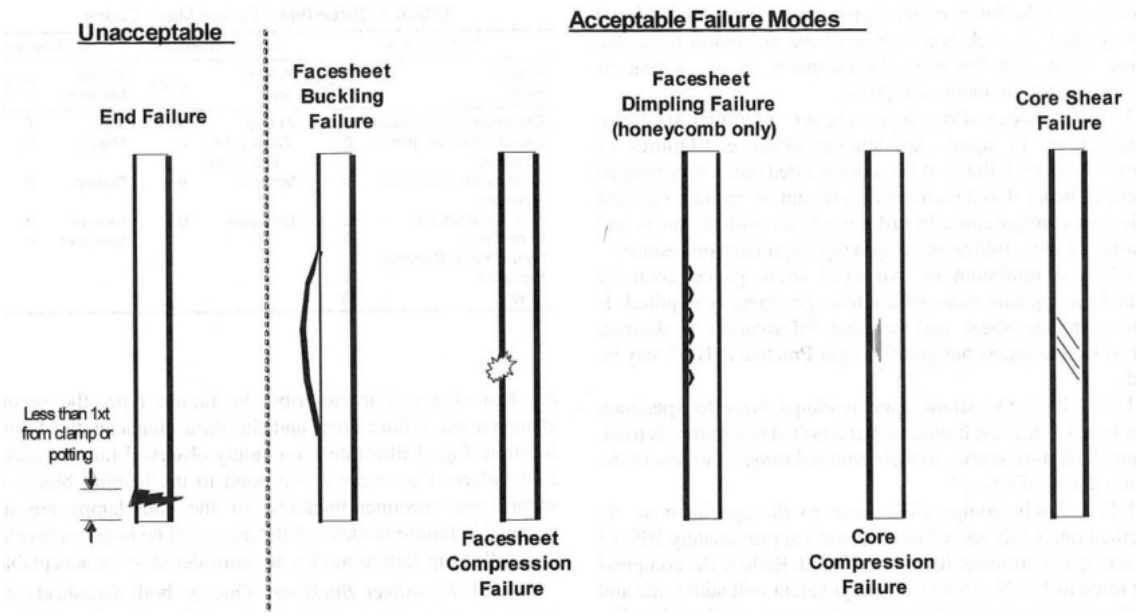

Figure A.15: Acceptable and unacceptable failure modes for ASTM C364.

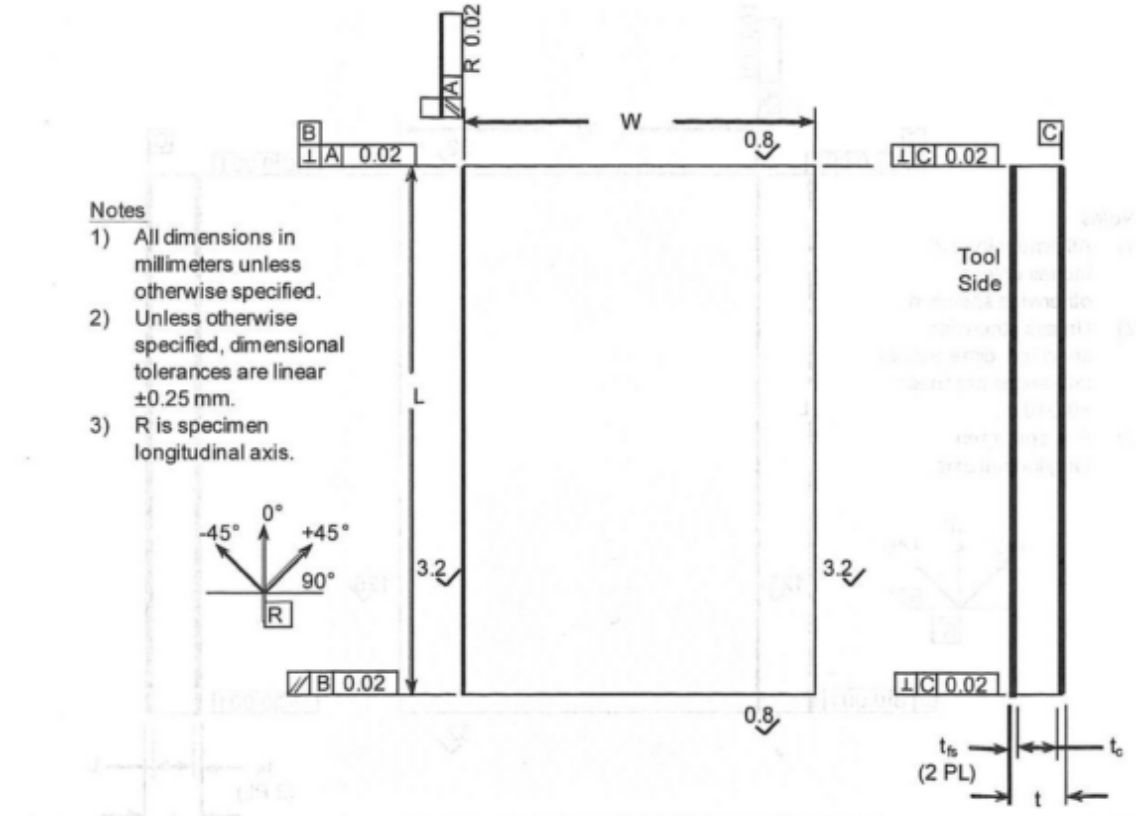

Dimension	Recommended Range
Length, L (mm)	$L \leq 8 \times t$
Width, W (mm)	$50 \leq W \leq L$; $W \geq 2 \times t$; $W \geq 4 \times$ cell widths (honeycomb only)
t, total panel thickness (mm)	As required, in order to be representative of intended use
Facesheet thickness, t_{fs}(mm)	As required, in order to be representative of intended use
Core thickness, t_c(mm)	As required, in order to be representative of intended use

Figure A.16: ASTM C364 coupon dimensions.

the clamps from damaging the specimen during testing, and to prevent damage to occur in the edge regions of the specimens. Each facing of the specimen is fitted with a lengthwise (0°) oriented strain gauge as can be seen in Figures A.17a and A.17b. Figure A.18a shows a specimen during loading and Figures A.18b, A.19a and

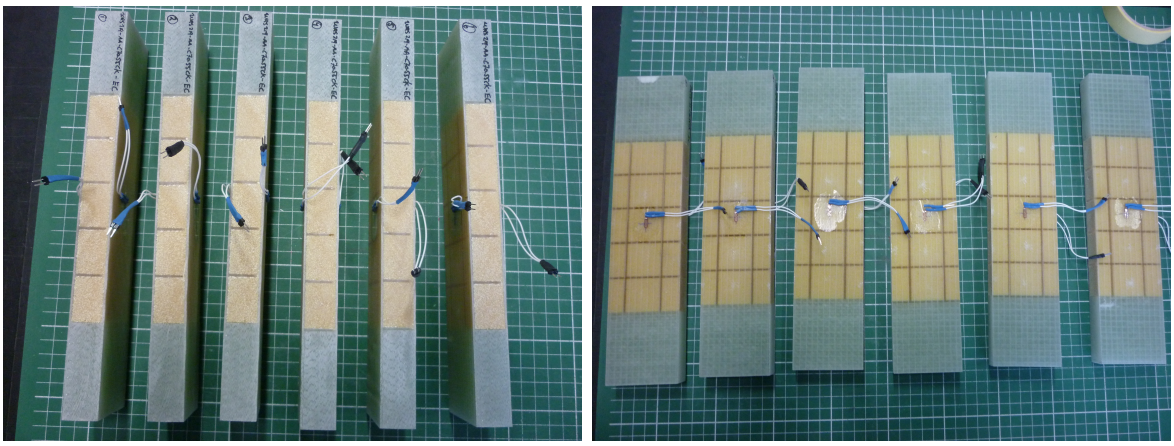

(a) Side view of EC test specimens.

(b) Front view of EC test specimens.

Figure A.17: Edgewise compression specimens showing tabs at each end and 1 strain gauge per side.

A.19b show respectively the side, front and back view of the specimens after testing. All failure mechanisms observed are acceptable for the ASTM C364 test standard. From the side view in Figure A.18bit can be seen that facings have failed in a wrinkling manner of which 4 outward and 2 inward with respect to the core. This resulted in debonding for all 4 outward wrinkling specimens and in one of these propagated further into core failure. In the 2 inward wrinkling cases it is seen that the core has taken plastic indentation damage from the inward moving facings. When looking at the front view, multiple circular white spots can be seen in approximately the middle of the square foam blocks. These spots were already visible before testing and might indicate small dry spots as a production defect. In both figures for front and back view (Figures A.19a and A.19b) it can be seen from the ±45° oriented white lines that damage has occurred in the biaxial plies under compression. These might have caused a local decrease in stiffness and lead to the wrinkling/debonding type failure as discussed above.

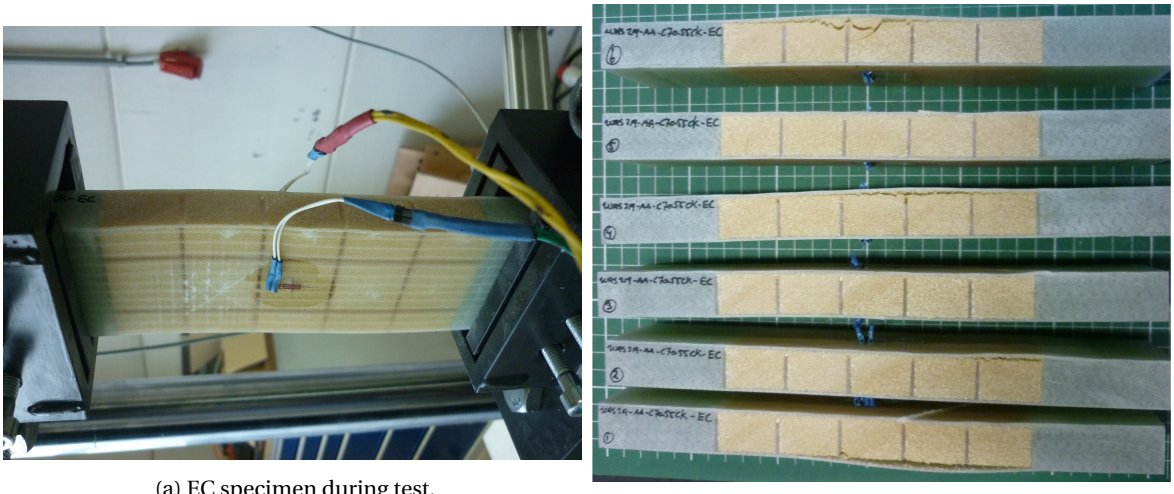

(a) EC specimen during test.

(b) EC specimens after test.

Figure A.18: Edgewise compression specimens during and after loading.

Further analysis on these sandwich specimens will be done in a similar manner as for the facing edgewise compression characterisation as discussed in Section A.1.2. The compressive stress is assumed to be carried fully by the facings, while the core material only serves a stabilising purpose. Hence for the computation of

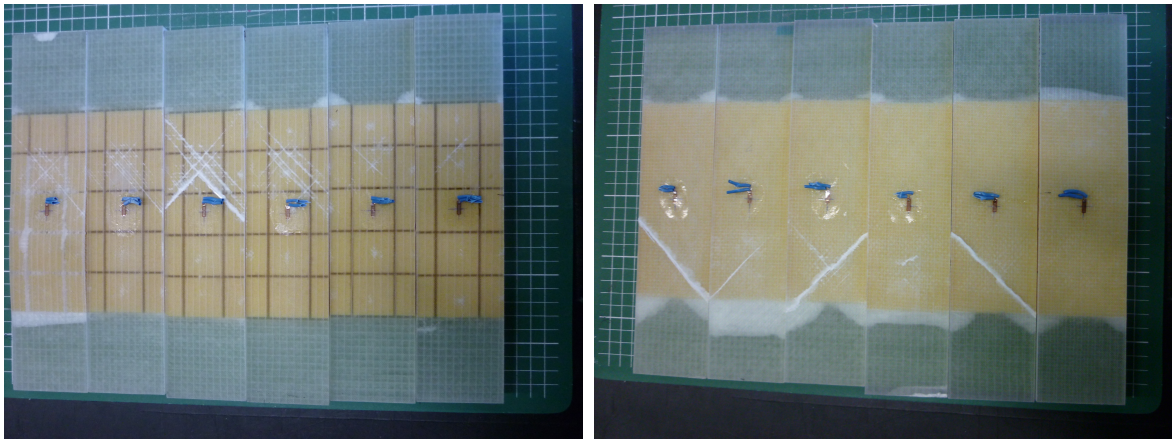

(a) EC specimens front view after test.

(b) EC specimens back view after test.

Figure A.19: Edgewise compression specimens after loading showing facing damage.

the stress, Equation A.1 can be used where the area is only that of the cross-section of the facings and not of the core. The stress-strain curves obtained for front and back side measurements are shown in Figures A.20a and A.20b. Result analysis of these data sets in terms of Young's moduli and damage/max/ult stress/strain are summarised in Table A.10.

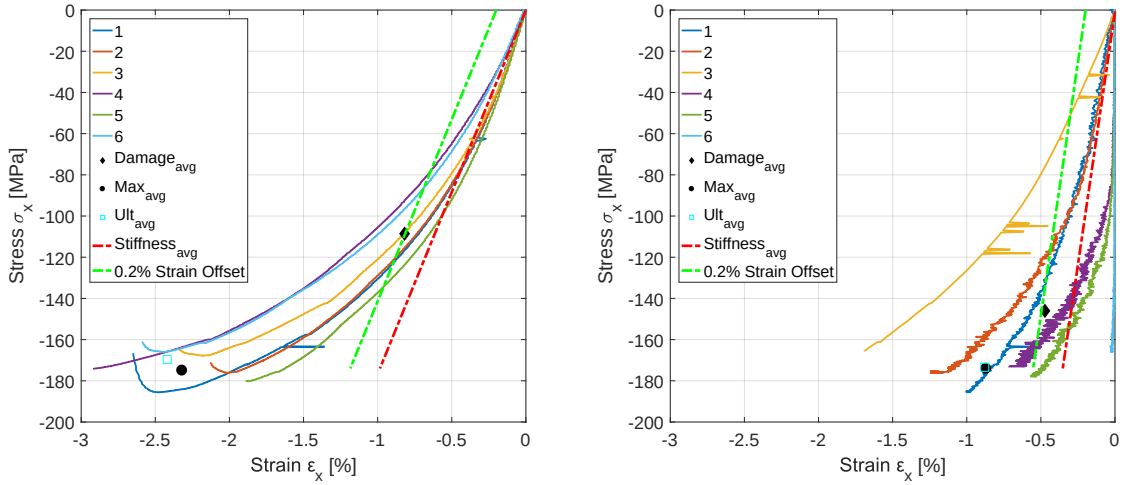

(a) EC stress-strain curves front.

(b) EC stress-strain curves back.

Figure A.20: Stress-strain curves for the EC test specimens for both front and back side strain gauges.

Table A.10: Resulting averaged data for EC tests for both front and back strain gauges. Units for stresses and moduli are [MPa] and units for strains are [%].

Sandwich, n=6		ε_{dmg}	σ_{dmg}	ε_{max}	σ_{max}	ε_{ult}	σ_{ult}	E
Mean	-8.18E-01	-1.09E+02	-2.32E+00	-1.75E+02	-2.42E+00	-1.70E+02	1.77E+04	
Standard Deviation	5.19E-02	8.69E+00	3.75E-01	7.42E+00	3.75E-01	6.89E+00	2.52E+03	
Variance	2.70E-03	7.55E+01	1.41E-01	5.51E+01	1.41E-01	4.74E+01	6.35E+06	
Mean	-4.73E-01	-1.46E+02	-8.70E-01	-1.74E+02	-8.79E-01	-1.73E+02	4.91E+04	
Standard Deviation	2.65E-01	2.21E+01	5.73E-01	7.63E+00	5.74E-01	8.24E+00	2.94E+04	
Variance	7.01E-02	4.90E+02	3.28E-01	5.83E+01	3.30E-01	6.79E+01	8.63E+08	

From comparison of the front and back side measurements using Figures A.20a and A.20b and Table A.10, it can be seen that the back side measurements are not as fluent as the front side measurements. The exact cause of this measurement 'noise' is unknown but since the wavy effect is noticeable only noticeable on all 6 back sides of the specimens it probably has to do with the interface between back strain gauge and the data logging device. The average stiffness of the back facings is a factor 2.8 higher than that of the front facings.

When comparing the sandwich's stress-strain curve with that of a purely monolithic triax laminate (Figure A.7a in Section A.1.2), it can be seen that the average ultimate strains are about equal, whereas the ultimate stress and stiffness of the monolithic triax laminate are about 2.8 times higher than for the front facing of the sandwich structure (factor 8 wrt back facing of the sandwich structure). This is counter-intuitive since the expectation would be that in the sandwich structure the core would stabilise the facings and hence make it possible to reach a higher stiffness and strength before collapse. The only explanation available for this unexpected result is that the gauge length for the facings only tests is short enough to stabilise the specimen even more than the core material can. No gauge length was reported for the facing only EC test, total length was 150mm.

A.3.2. EDGEWISE TENSILE

No test standard is available for this type of test, however it is basically the edgewise compression test with a reversed direction of loading. Hence the same test coupons will be used as discussed in Section A.3.1. The following requirements and constraints posed on the test specimens are assumptions in order to obtain a reliable test method. For stress and strain calculations, not the complete sandwich cross sectional area should be used, but rather the cross sectional area of the two facings. In this case acceptable failure modes are all modes that occur away from the supporting clamps, so preferably in the middle section of the coupons. Acceptable failure modes are core tensile fracture and facing tensile failure. It is assumed that at least 5 specimens should be tested per test condition to obtain statistically significant data. By performing this test on a coupon, its edgewise tensile strength is obtained.

The sandwich coupons used for this test are exactly the same as used for the edgewise compression test discussed in Section A.3.1, thus also including the monolithic glass fibre tabs to prevent clamping damage. The only difference is that for this test, every coupon is fitted with a lengthwise and width-wise (0/90°) oriented strain gauge on only 1 side of the sandwich as shown in Figures A.21a and A.21b. The design and actual (measured) coupon dimensions are given in Table A.11. For this test, six test specimens were tested.

Table A.11: ET: Design and actual coupon dimensions. Average values based on 6 test coupons.

Dimension	Design Value	Measured Value
Width b [mm]	60	59.68
Total Length L_{tot} [mm]	270	268.1
Gauge Length L_{gauge} [mm]	150	148.7
Sandwich thickness t_s [mm]	22	22.37
Core Thickness t_c [mm]	20	20.02

Figure A.22a shows a specimen during loading and Figures A.22b, A.22c and A.22d show respectively the side, front and back view of the specimens after testing. All failure mechanisms observed are deemed acceptable. In both figures for front and back view (Figures A.22c and A.22d) it can be seen that on almost all coupons, white ±45° oriented lines are visible indicating failure of the ±45° glass fibre plies. From the side view it can be observed that all six coupons show core tensile failure.

Further analysis on these sandwich specimens will be done in a similar manner as for the sandwich edgewise compression characterisation as discussed in Section A.3.1. The tensile stress is assumed to be carried fully by the facings, while the core material only serves a stabilising purpose. Hence for the computation of the stress, Equation A.1 can be used where the area is only that of the facings and not of the core. The stress-strain curves obtained are shown in Figures A.23a and A.23b using respectively the strain gauge in loading direction (0°) and perpendicular to the loading direction (90°). Analysis of these data sets in terms of Young's moduli and damage/max/ult stress/strain are summarised in Table A.12. Using the 0.2% offset rule as seen in Figure A.23a, damage occurs at an average tensile stress of 85.16$[MPa]$ with corresponding strain of 0.72%.

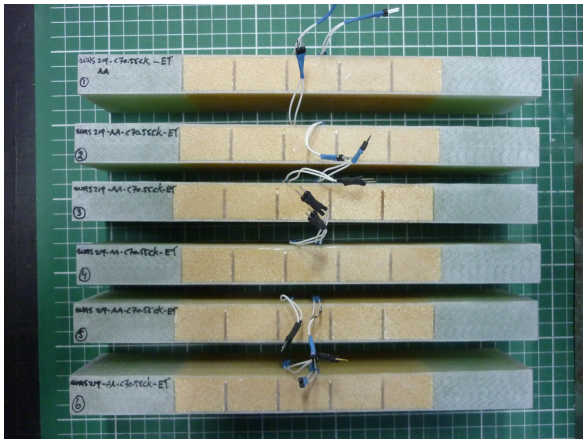

(a) Side view of ET test specimens.

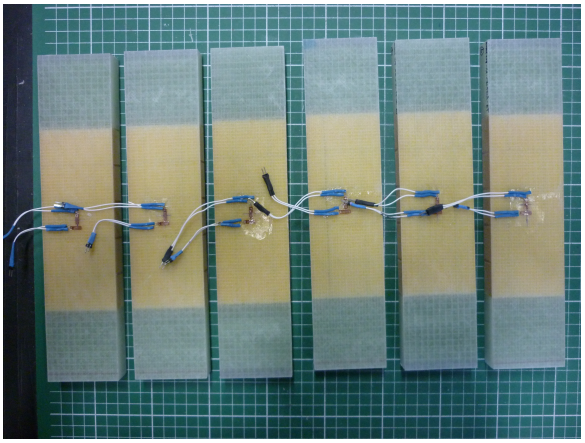

(b) Front view of ET test specimens.

Figure A.21: Edgewise tensile (ET) specimens showing tabs at each end and 2 strain gauges in perpendicular position on 1 facing.

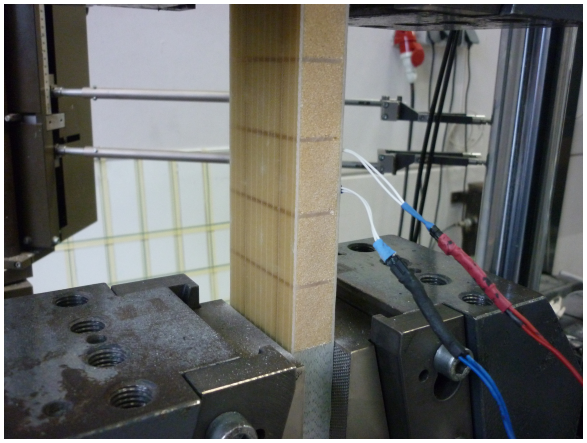

(a) ET specimen during test.

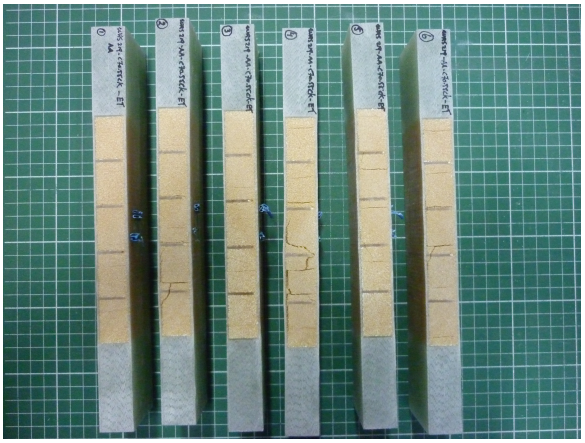

(b) ET specimens side view after test.

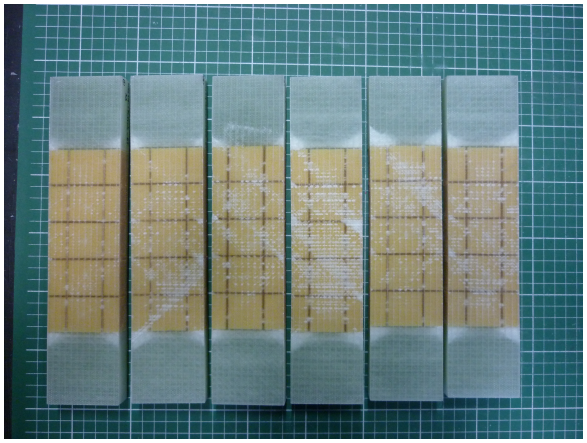

(c) ET specimens front view after test.

(d) ET specimens back view after test.

Figure A.22: Edgewise tensile specimens during and after testing - multiple views.

Figure A.23b shows the stress-strain graph using 90° strain gauge measurements, from which it is clear that failure in the ±45° plies occurs at an average transverse stress of 80.25$[MPa]$ with corresponding strain of 0.35%, which relates to the tensile damage initiation point at 85.16$[MPa]$ as discussed before. Because of the small strains in the 90° strain orientation, the 0.2% offset method does not have an intersection with the stress-strain curves and hence does not provide a damage initiation stress or strain. By lowering the 0.2%

offset, a damage initiation point can be defined, however for the ET test the 0° oriented strains are of much higher importance.

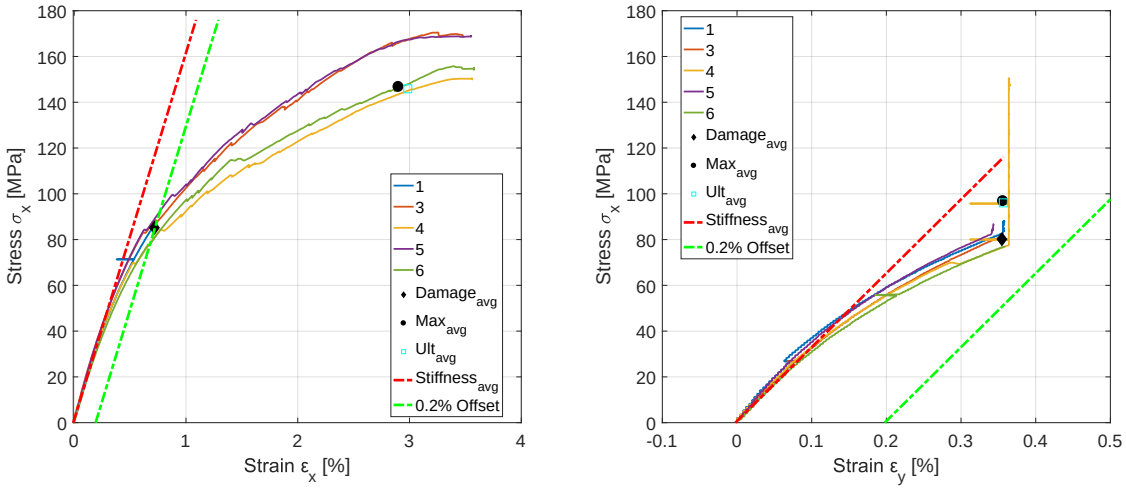

(a) Stress-strain curves using 0° oriented strain gauges. (b) Stress-strain curves using 90° oriented strain gauges.

Figure A.23: Stress-strain curves for ET tests for both 0° and 90° oriented strain gauges.

Table A.12: Resulting averaged data for ET tests for both 0° and 90° oriented strain gauges. Units for stresses and moduli are [MPa] and units for strains are [%].

Sandwich, n=5		ε_{dmg}	σ_{dmg}	ε_{max}	σ_{max}	ε_{ult}	σ_{ult}	E
0 deg	Mean	7.18E-01	8.52E+01	2.90E+00	1.47E+02	2.98E+00	1.46E+02	1.60E+04
	Standard Deviation	1.60E-02	4.42E+00	1.21E+00	3.39E+01	1.25E+00	3.33E+01	7.04E+02
	Variance	2.56E-04	1.95E+01	1.47E+00	1.15E+03	1.57E+00	1.11E+03	4.95E+05
90 deg[3]	Mean	3.54E-01	8.01E+01	3.54E-01	8.03E+01	3.54E-01	8.03E+01	3.23E+04
	Standard Deviation	9.04E-03	2.64E+00	8.78E-03	2.55E+00	8.78E-03	2.55E+00	2.39E+03
	Variance	8.17E-05	6.99E+00	7.71E-05	6.52E+00	7.71E-05	6.52E+00	5.70E+06

A.3.3. FLATWISE COMPRESSION

The used test method is "ASTM C 365/C 365M - 05" or "Standard Test Method for Flatwise Compressive Properties of Sandwich Cores"[78]. The test setup is similar to the one shown in Figure A.10. In this test method, the compressive load is applied uni-axially in the direction normal to the plane of facings of the sandwich coupon. The force is transmitted to the sandwich structure using loading platens attached to the testing machine. By applying this test method to coupon testing, its flatwise compressive strength and modulus can be obtained. For this test standard, the test coupons have to be of square or circular cross-section with a minimum and maximum facing area of respectively 625$[mm^2]$ and 10,000$[mm^2]$[78] for the used PVC foam core. The constituents used in the sandwich coupons are Advantex SE1500 bi-axial glass fibre mats, Airex C70.55CK PVC foam core and resin system Y. These materials are compliant for use with this test standard. For this test, eight test specimens were tested. Test specimen dimensions are 100mm x 100mm with a total thickness of 22.21mm on average. The design and actual (measured) coupon dimensions are given in Table A.14, which are also compliant for the test standard.

Figures A.24a and A.24b show the coupons from 2 different views. Figures A.25a shows a specimen in the test setup, and A.25b shows a specimen during loading. Figures A.26(a)-(f) show the sandwich coupons after

[3]No damage stresses and strains are defined because of shortcomings of the 0.2% offset method. However the 90° damage point is of much lower importance for the ET test than the 90° damage point.

Table A.13: Flatwise compression (FC) specimens before testing.

Dimension	Design Value	Measured Value
Width1 b_1 [mm]	100	99.78
Width2 b_2 [mm]	100	99.60
Sandwich thickness t_s [mm]	22	22.21
Core Thickness t_c [mm]	20	20.02

Table A.14: FC: Design and actual coupon dimensions. Average values based on 8 test coupons.

(a) Front view of FC test specimens.

(b) Side view of FC test specimens.

testing. From the figures it can be seen that all the specimens failed in some kind of a core failure as expected. The loading type can be seen as the resin grid being pushed into the scrim core material. So puncture of this scrim foam material by the resin grid can be expected. However this type of failure occurred only once in the test specimens as can be seen in Figure A.26e at the bottom of the 3rd resin bridge from the left. The most often observed failure behaviour is a buckling behaviour of the resin bridges. This buckling behaviour remains visible after unloading of the specimens indicating plastic deformation of the resin bridges. As can be seen in the zoomed figures, this behaviour can occur with all bridges buckling in the same direction, or in mixed directions. The PVC foam at the edges of the specimens are therefore buckling in or out depending on the behaviour of the nearest resin bridge buckling. It can be seen that this buckling behaviour often leads to failure of the PVC core at the hollow side of the resin bridge.

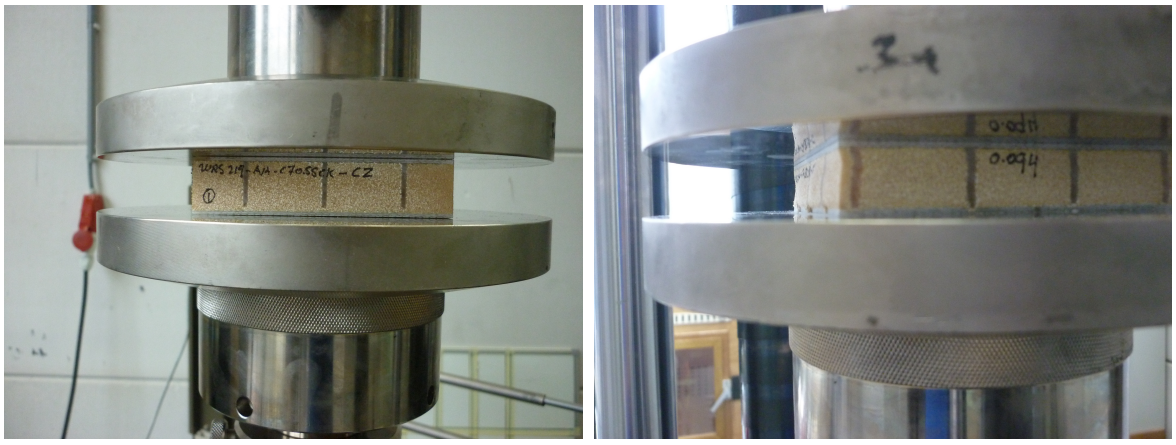

(a) FC specimen during test.

(b) FC specimen side view after test.

Figure A.25: Flatwise compression specimens during loading.

Numerical analysis on these test specimens will be done in a similar manner as before. The compressive stress is acting on the full area of the facing and hence is simply equal to $\sigma_{compressive} = Force_{applied}/Area_{facing}$. The stress-strain curves obtained in this manner are shown in Figure A.27a and the analysis of these results

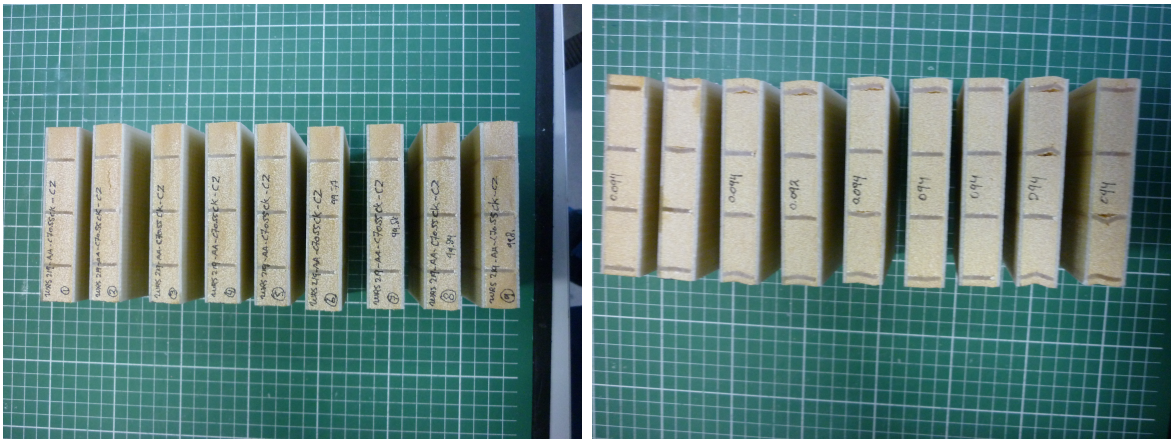

(a) FC specimens front view after test.

(b) FC specimens back view after test.

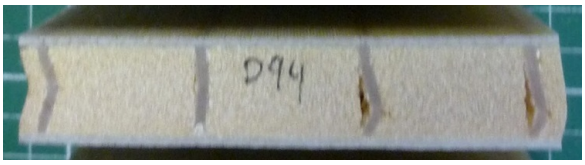

(c) FC Zoom1.

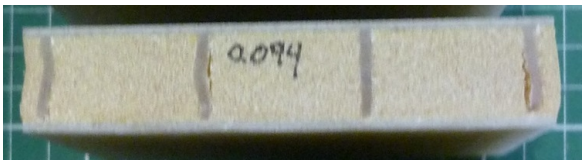

(d) FC Zoom2.

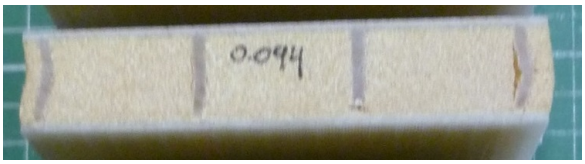

(e) FC Zoom3.

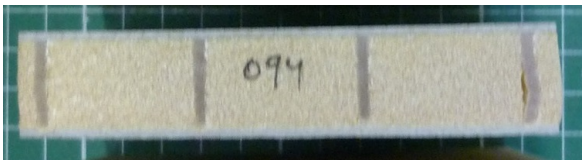

(f) FC Zoom4.

Figure A.26: FC specimens after testing showing different damage modes.

in terms of Young's moduli and damage/max/ult stress/strain are summarised in Table A.15. An important note to be made is the visible toe region for which a correction is necessary as also discussed before in Section A.1.3 with help of Figure A.8b.
When comparing the stress-strain results of this sandwich specimen to the stress-strain results for the PVC core material (comparing Figures A.27a and A.27b), it can be seen that for the core that contains resin bridges, the stiffness is approximately a factor 5 higher than for plain PVC foam material, while the ultimate strain is a factor 4 smaller, and the maximum stress is a factor 6.5 higher.

Table A.15: Resulting averaged data for FC tests. Units for stresses and moduli are [MPa] and units for strains are [%].

Sandwich, n=9	ε_{dmg}	σ_{dmg}	ε_{max}	σ_{max}	ε_{ult}	σ_{ult}	E
Mean	-7.69E+00	-7.54E+00	-1.60E+01	-1.15E+01	-1.97E+01	-9.70E+00	1.01E+02
Standard Deviation	5.97E-01	1.11E+00	1.61E+00	4.33E-01	2.09E+00	1.27E+00	1.08E+01
Variance	3.57E-01	1.23E+00	2.60E+00	1.87E-01	4.38E+00	1.61E+00	1.16E+02

A.3.4. RAIL SHEAR

The used test method is "ASTM C 273 - 00" or "Standard Test Method for Shear Properties of Sandwich Core Materials"[74]. The test setup is similar to the one shown in Figures 4.1a and 4.1b, using an extensiometer to measure the displacement between the two facings. In this test method, the shear load is applied parallel to the plane of the facings. The two facings are bonded to the loading plates which transfers the shear force from the test machine to the test coupons. By applying this test method to coupon testing, the core shear strength and modulus can be obtained. The constituents used in the sandwich coupons are Advantex SE1500 bi-axial glass fibre mats, Airex C70.55CK PVC foam core and resin system Y. These materials are compliant for

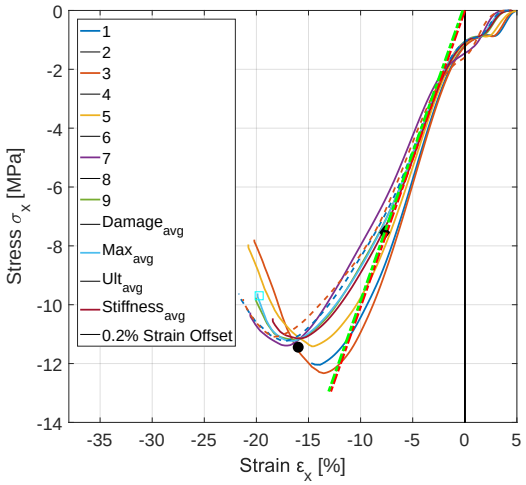

(a) FC sandwich specimen during test.

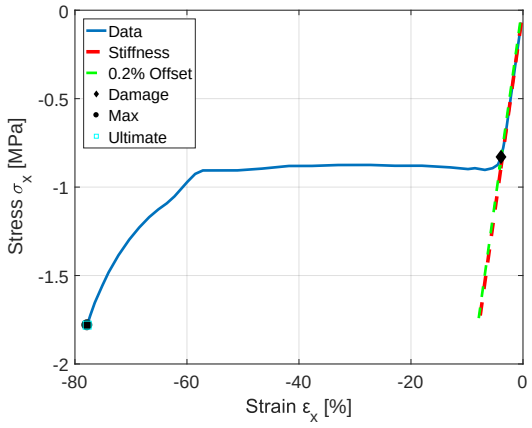

(b) Analysis of FC data for PVC core material.

Figure A.27: Analysis of sandwich and PVC core FC tests.

use with this test standard. For this test, nine test specimens were tested. The design and actual (measured) coupon dimensions are given in Table A.16, which are compliant for the test standard. According to SBT, all specimens have failed in core shear failure.

Table A.16: Sxz: Design and actual coupon dimensions. Average values based on 9 test coupons.

Dimension	Design Value	Measured Value
Width b [mm]	60	59.93
Length L [mm]	270	269.4
Sandwich thickness t_s [mm]	22	22.05
Core Thickness t_c [mm]	20	20.00

Numerical analysis on these test specimens will be done in a similar manner as before. The shear stress is acting on the full area of the facing and can hence be computed using Equation A.4. The stress-strain curves obtained in this manner are shown in Figure A.28 and the analysis of these results in terms of Young's moduli and damage/max/ult stress/strain are summarised in Table A.17.

$$\tau = \frac{P}{L \cdot b} \tag{A.4}$$

Table A.17: Averaged data from all rail shear characterisation tests. Units for stresses and moduli are [MPa] and units for strains are [%].

Sandwich, n=9	ε_{dmg}	σ_{dmg}	ε_{max}	σ_{max}	ε_{ult}	σ_{ult}	E
Mean	1.15E+00	5.82E-01	4.53E+00	9.42E-01	3.15E+01	4.48E-02	6.08E+01
Standard Deviation	6.44E-02	2.10E-02	9.40E-01	2.69E-02	5.26E+00	2.31E-02	2.40E+00
Variance	4.15E-03	4.41E-04	8.83E-01	7.24E-04	2.76E+01	5.33E-04	5.78E+00

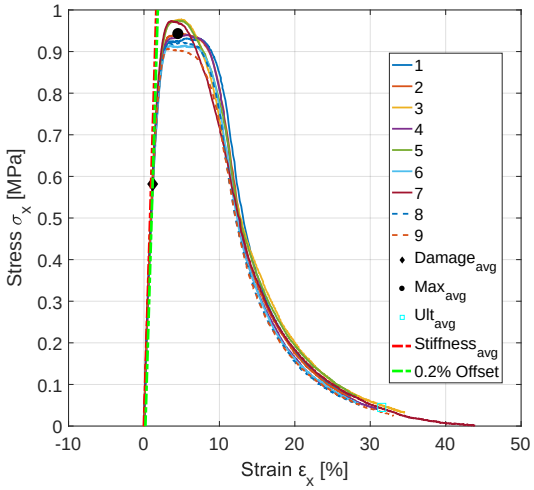

Figure A.28: Sxz sandwich shear stress-shear strain curve.

B

Resin Link Results

B.1. Flatwise Tension 3mm Resin Link Results

Table B.1: Data for all flatwise tensile characterisation tests for resin link 3mm sandwich structure. Units for stresses and moduli are [MPa] and units for strains are [%].

Sandwich Structure 3mm resin links, n=10	ε_{dmg} [%]	σ_{dmg} [MPa]	ε_{max} [%]	σ_{max} [MPa]	ε_{ult} [%]	σ_{ult} [MPa]	E [MPa]
ID#1	3.398312	1.477778	3.850286	1.587262	3.953979	1.5422	46.22057
ID#2	3.888171	1.604698	4.086255	1.633883	4.257947	1.582379	43.50934
ID#3	3.805831	1.636169	3.84367	1.638513	3.982888	1.531351	45.37485
ID#4	2.956943	1.332503	3.599564	1.530918	3.718319	1.481453	48.32728
ID#5	4.067794	1.558914	4.188367	1.571477	4.254003	1.413174	40.30745
ID#6	4.067594	1.664715	4.033097	1.666916	4.125053	1.556892	43.04577
ID#7	3.148042	1.487659	3.145769	1.562600	3.481058	1.307415	50.29311
ID#8	3.445361	1.422797	4.039991	1.595412	4.193425	1.490292	43.84317
ID#9	3.451072	1.399457	4.104007	1.550416	4.187358	1.486815	42.97864
ID#10	3.701959	1.560102	3.902558	1.593183	3.938457	1.540031	44.54509
Mean	3.593108	1.514479	3.879356	1.593058	4.009249	1.493200	44.84452
Standard Deviation	0.376735	0.108726	0.308634	0.042557	0.252366	0.081081	2.870706
Variance	0.141929	0.011821	0.095255	0.001811	0.063688	0.006574	8.240951

B.2. Flatwise Tension 5mm resin link Results

Table B.2: Data for all flatwise tensile characterisation tests for resin link 5mm sandwich structure. Units for stresses and moduli are [MPa] and units for strains are [%].

Sandwich Structure 5mm resin links, n=10	ε_{dmg} [%]	σ_{dmg} [MPa]	ε_{max} [%]	σ_{max} [MPa]	ε_{ult} [%]	σ_{ult} [MPa]	E [MPa]
ID#1	5.48343	1.344648	5.415738	1.471255	5.48343	1.344648	24.26465
ID#2	4.260488	1.356022	5.061914	1.559946	5.074756	1.538661	33.39456
ID#3	5.321252	1.376305	5.299628	1.484429	5.999186	1.42654	26.87538
ID#4	3.947718	1.257875	4.92454	1.594047	4.925968	1.582381	32.17467
ID#5	1.723689	0.376503	5.848728	1.509233	6.151153	1.452471	22.7134
ID#6	3.903505	1.384978	3.89607	1.468084	4.445815	1.399072	37.43955
ID#7	4.536008	1.361761	5.145716	1.539138	5.14641	1.519754	31.40604
ID#8	5.603555	1.637828	5.680481	1.643861	5.737804	1.567942	30.30326
ID#9	5.186406	1.49926	5.168914	1.614123	5.383414	1.478849	30.05987
ID#10	2.742419	0.006509	8.917404	1.546018	8.918479	1.491483	0.255211
Mean	4.270847	1.160169	5.535913	1.543013	5.726642	1.48018	26.88866
Standard Deviation	1.261478	0.527893	1.299487	0.060991	1.232099	0.075906	10.31381
Variance	1.591327	0.278671	1.688666	0.00372	1.518069	0.005762	106.3746

B.3. THREE POINT BENDING 3MM RESIN LINK RESULTS

Table B.3: Flexural stress-strain data for all TPB characterisation tests for resin link 3mm sandwich structure. Units for stresses and moduli are [MPa] and units for strains are [%].

Sandwich Structure 3mm resin links, n=10	ε_{dmg} [%]	σ_{dmg} [MPa]	ε_{max} [%]	σ_{max} [MPa]	ε_{ult} [%]	σ_{ult} [MPa]	E [MPa]
ID#1	5.48343	1.344648	5.415738	1.471255	5.48343	1.344648	24.26465
ID#2	4.260488	1.356022	5.061914	1.559946	5.074756	1.538661	33.39456
ID#3	5.321252	1.376305	5.299628	1.484429	5.999186	1.42654	26.87538
ID#4	3.947718	1.257875	4.92454	1.594047	4.925968	1.582381	32.17467
ID#5	1.723689	0.376503	5.848728	1.509233	6.151153	1.452471	22.7134
ID#6	3.903505	1.384978	3.89607	1.468084	4.445815	1.399072	37.43955
ID#7	4.536008	1.361761	5.145716	1.539138	5.14641	1.519754	31.40604
ID#8	5.603555	1.637828	5.680481	1.643861	5.737804	1.567942	30.30326
ID#9	5.186406	1.49926	5.168914	1.614123	5.383414	1.478849	30.05987
ID#10	2.742419	0.006509	8.917404	1.546018	8.918479	1.491483	0.255211
Mean	4.270847	1.160169	5.535913	1.543013	5.726642	1.48018	26.88866
Standard Deviation	1.261478	0.527893	1.299487	0.060991	1.232099	0.075906	10.31381
Variance	1.591327	0.278671	1.688666	0.00372	1.518069	0.005762	106.3746

Table B.4: Shear stress-displacement data for all TPB characterisation tests for resin link 3mm sandwich structure. Units for stresses and moduli are [MPa] and units for strains are [%].

Sandwich Structure 3mm resin links, n=10	δ_{dmg} [mm]	τ_{dmg} [MPa]	δ_{max} [mm]	τ_{max} [MPa]	δ_{ult} [mm]	τ_{ult} [MPa]
ID#1	5.72556	0.69280	15.15749	1.18662	15.50552	1.18588
ID#2	5.66484	0.67358	13.84871	1.12018	14.46568	1.06056
ID#3	5.81390	0.69187	11.82882	1.06753	11.99273	1.03074
ID#4	5.64820	0.67241	12.89740	1.06297	13.09505	1.04104
ID#5	5.72400	0.67571	12.99384	1.05930	13.19392	1.05250
ID#6	5.61666	0.65656	13.25149	1.08815	14.07843	1.04914
ID#7	5.66127	0.65595	12.50833	1.07723	13.90916	0.99507
ID#8	5.16621	0.61440	12.51631	1.11139	14.04707	1.08345
ID#9	5.54726	0.65440	13.01723	1.09047	13.56706	1.07768
ID#10	5.28901	0.63485	12.93995	1.09425	13.82302	1.07261
Mean	5.58569	0.66225	13.09596	1.09581	13.76776	1.06487
Standard Deviation	0.20360	0.02449	0.89493	0.03761	0.92360	0.04971
Variance	0.04145	0.00060	0.80089	0.00141	0.85304	0.00247

B.4. THREE POINT BENDING 5MM RESIN LINK RESULTS

Table B.5: Flexural stress-strain data for all TPB characterisation tests for resin link 5mm sandwich structure. Units for stresses and moduli are [MPa] and units for strains are [%].

Sandwich Structure 5mm resin links, n=10	ε_{dmg} [%]	σ_{dmg} [MPa]	ε_{max} [%]	σ_{max} [MPa]	ε_{ult} [%]	σ_{ult} [MPa]	E [MPa]
ID#1	5.48343	1.344648	5.415738	1.471255	5.48343	1.344648	24.26465
ID#2	4.260488	1.356022	5.061914	1.559946	5.074756	1.538661	33.39456
ID#3	5.321252	1.376305	5.299628	1.484429	5.999186	1.42654	26.87538
ID#4	3.947718	1.257875	4.92454	1.594047	4.925968	1.582381	32.17467
ID#5	1.723689	0.376503	5.848728	1.509233	6.151153	1.452471	22.7134
ID#6	3.903505	1.384978	3.89607	1.468084	4.445815	1.399072	37.43955
ID#7	4.536008	1.361761	5.145716	1.539138	5.14641	1.519754	31.40604
ID#8	5.603555	1.637828	5.680481	1.643861	5.737804	1.567942	30.30326
ID#9	5.186406	1.49926	5.168914	1.614123	5.383414	1.478849	30.05987
ID#10	2.742419	0.006509	8.917404	1.546018	8.918479	1.491483	0.255211
Mean	4.270847	1.160169	5.535913	1.543013	5.726642	1.48018	26.88866
Standard Deviation	1.261478	0.527893	1.299487	0.060991	1.232099	0.075906	10.31381
Variance	1.591327	0.278671	1.688666	0.00372	1.518069	0.005762	106.3746

Table B.6: Shear stress-displacement data for all TPB characterisation tests for resin link 5mm sandwich structure. Units for stresses and moduli are [MPa] and units for strains are [%].

Sandwich Structure 5mm resin links, n=10	δ_{dmg} [mm]	τ_{dmg} [MPa]	δ_{max} [mm]	τ_{max} [MPa]	δ_{ult} [mm]	τ_{ult} [MPa]
ID#1	5.63317	0.72719	11.98521	1.26449	11.99627	1.22489
ID#2	5.91038	0.74845	12.20566	1.22084	12.20566	1.22084
ID#3	4.98916	0.63390	11.39991	1.16308	11.54797	1.15942
ID#4	8.26305	0.95441	12.46427	1.22240	12.48802	1.22033
ID#5	5.17437	0.65670	12.95363	1.23718	13.14358	1.20966
ID#6	4.47144	0.54853	12.79570	1.21987	12.93655	1.17155
ID#7	4.89970	0.59944	13.24089	1.30221	13.26075	1.30176
ID#8	4.88278	0.62055	12.62288	1.28946	12.85774	1.27872
ID#9	4.97736	0.61600	12.29125	1.24157	12.31241	1.23738
ID#10	4.97619	0.60739	13.57503	1.27620	13.57602	1.21375
Mean	5.41776	0.67126	12.55344	1.24373	12.63250	1.22383
Standard Deviation	1.07841	0.11585	0.63167	0.04096	0.63033	0.04279
Variance	1.16297	0.01342	0.39900	0.00168	0.39731	0.00183

B.5. FOUR POINT BENDING 3MM RESIN LINK RESULTS

Table B.7: Flexural stress-strain data for all TPB characterisation tests for resin link 5mm sandwich structure. Units for stresses and moduli are [MPa] and units for strains are [%].

Sandwich Structure 3mm resin links, n=10	ε_{dmg} [%]	σ_{dmg} [MPa]	ε_{max} [%]	σ_{max} [MPa]	ε_{ult} [%]	σ_{ult} [MPa]	E [MPa]
ID#1	5.48343	1.344648	5.415738	1.471255	5.48343	1.344648	24.26465
ID#2	4.260488	1.356022	5.061914	1.559946	5.074756	1.538661	33.39456
ID#3	5.321252	1.376305	5.299628	1.484429	5.999186	1.42654	26.87538
ID#4	3.947718	1.257875	4.92454	1.594047	4.925968	1.582381	32.17467
ID#5	1.723689	0.376503	5.848728	1.509233	6.151153	1.452471	22.7134
ID#6	3.903505	1.384978	3.89607	1.468084	4.445815	1.399072	37.43955
ID#7	4.536008	1.361761	5.145716	1.539138	5.14641	1.519754	31.40604
ID#8	5.603555	1.637828	5.680481	1.643861	5.737804	1.567942	30.30326
ID#9	5.186406	1.49926	5.168914	1.614123	5.383414	1.478849	30.05987
ID#10	2.742419	0.006509	8.917404	1.546018	8.918479	1.491483	0.255211
Mean	4.270847	1.160169	5.535913	1.543013	5.726642	1.48018	26.88866
Standard Deviation	1.261478	0.527893	1.299487	0.060991	1.232099	0.075906	10.31381
Variance	1.591327	0.278671	1.688666	0.00372	1.518069	0.005762	106.3746

Table B.8: Shear stress vs displacement data for all TPB characterisation tests for resin link 3mm sandwich structure. Units for shear stresses are [MPa] and units for displacements are [mm].

Sandwich Structure 3mm resin links, n=10	δ_{dmg} [mm]	τ_{dmg} [MPa]	δ_{max} [mm]	τ_{max} [MPa]	δ_{ult} [mm]	τ_{ult} [MPa]
ID#1	3.398	0.844	6.367	1.213	6.376	1.105
ID#2	5.351	1.142	6.354	1.215	6.376	1.051
ID#3	4.880	1.054	6.144	1.181	6.154	0.930
ID#4	4.936	1.042	6.286	1.155	6.296	0.942
ID#5	3.587	0.877	7.956	1.271	7.970	0.977
ID#6	3.160	0.774	5.887	1.151	5.903	0.915
ID#7	3.068	0.782	6.480	1.218	6.487	0.958
ID#8	3.944	1.020	6.706	1.419	6.706	1.419
ID#9	3.618	0.914	6.333	1.271	6.593	1.016
ID#10	3.543	0.900	6.063	1.238	6.081	0.956
Mean	3.949	0.935	6.458	1.233	6.494	1.027
Standard Deviation	0.811	0.124	0.573	0.077	0.571	0.150
Variance	0.657	0.015	0.328	0.006	0.326	0.022

B.6. FOUR POINT BENDING 5MM RESIN LINK RESULTS

Table B.9: Flexural stress-strain data for all TPB characterisation tests for resin link 5mm sandwich structure. Units for stresses and moduli are [MPa] and units for strains are [%].

Sandwich Structure 5mm resin links, n=10	ε_{dmg} [%]	σ_{dmg} [MPa]	ε_{max} [%]	σ_{max} [MPa]	ε_{ult} [%]	σ_{ult} [MPa]	E [MPa]
ID#1	5.48343	1.344648	5.415738	1.471255	5.48343	1.344648	24.26465
ID#2	4.260488	1.356022	5.061914	1.559946	5.074756	1.538661	33.39456
ID#3	5.321252	1.376305	5.299628	1.484429	5.999186	1.42654	26.87538
ID#4	3.947718	1.257875	4.92454	1.594047	4.925968	1.582381	32.17467
ID#5	1.723689	0.376503	5.848728	1.509233	6.151153	1.452471	22.7134
ID#6	3.903505	1.384978	3.89607	1.468084	4.445815	1.399072	37.43955
ID#7	4.536008	1.361761	5.145716	1.539138	5.14641	1.519754	31.40604
ID#8	5.603555	1.637828	5.680481	1.643861	5.737804	1.567942	30.30326
ID#9	5.186406	1.49926	5.168914	1.614123	5.383414	1.478849	30.05987
ID#10	2.742419	0.006509	8.917404	1.546018	8.918479	1.491483	0.255211
Mean	4.270847	1.160169	5.535913	1.543013	5.726642	1.48018	26.88866
Standard Deviation	1.261478	0.527893	1.299487	0.060991	1.232099	0.075906	10.31381
Variance	1.591327	0.278671	1.688666	0.00372	1.518069	0.005762	106.3746

Table B.10: Shear stress vs displacement data for all TPB characterisation tests for resin link 5mm sandwich structure. Units for shear stresses are [MPa] and units for displacements are [mm].

Sandwich Structure 5mm resin links, n=10	δ_{dmg} [mm]	τ_{dmg} [MPa]	δ_{max} [mm]	τ_{max} [MPa]	δ_{ult} [mm]	τ_{ult} [MPa]
ID#1	3.793	0.974	6.699	1.408	6.705	1.362
ID#2	3.217	0.843	5.974	1.317	5.982	1.112
ID#3	3.941	0.980	6.005	1.288	6.095	1.053
ID#4	3.601	0.873	6.365	1.295	6.370	1.191
ID#5	4.361	1.036	5.480	1.207	5.494	1.047
ID#6	4.960	1.160	5.877	1.274	5.965	0.983
ID#7	3.514	0.880	6.009	1.313	6.018	1.086
ID#8	3.695	0.959	5.799	1.344	5.818	1.101
ID#9	3.408	0.862	6.047	1.330	6.058	1.125
ID#10	3.462	0.891	5.890	1.317	5.921	1.021
Mean	3.795	0.946	6.015	1.309	6.043	1.108
Standard Deviation	0.519	0.098	0.327	0.051	0.321	0.107
Variance	0.269	0.010	0.107	0.003	0.103	0.011

C

DIGITAL APPENDIX

The digital appendix attached to this thesis is fairly large due to the amount of videos and data added. Therefore the appendix is enclosed on an external hard drive. An overview of the contents of this external hard drive is given in Table C.1 below.

Table C.1: Overview of the contents of the digital appendix.

Flatwise tension tests	3mm	10 videos with fixed legend scale
		10 videos with adapting legend scale
	5mm	10 videos with fixed legend scale
		10 videos with adapting legend scale
Three point bending tests	3mm	10 videos with fixed legend scale
		10 videos with adapting legend scale
	5mm	10 videos with fixed legend scale
		10 videos with adapting legend scale
Four point bending tests	3mm	10 videos with fixed legend scale
		10 videos with adapting legend scale
	5mm	10 videos with fixed legend scale
		10 videos with adapting legend scale